T.R.
BOLU ABANT İZZET BAYSAL UNIVERSITY
INSTITUTE OF GRADUATE STUDIES
Department of Physics

STRUCTURAL AND MAGNETO-ELECTRICAL CHARACTERIZATION OF CATHODES BASED ON RARE-EARTH MANGANITES FOR SOLID OXIDE FUEL CELL

DOCTOR OF PHILOSOPHY

SEVGİ KARADAVUT

ACADEMIC SUPERVISOR
Assoc. Prof. Dr. Sevgi POLAT ALTINTAŞ

BOLU, ŞUBAT - 2022

APPROVAL OF THE THESIS

Structural and Magneto-Electrical Characterization of Cathodes Based on Rare-Earth Manganites For Solid Oxide Fuel Cells submitted by **Sevgi Karadavut** and defended before the Examining Committee Members listed below in partial fulfillment of the requirements for the degree of **Doctor of Philosophy** in **Department of Physics, Institute of Graduate Studies of Bolu Abant Izzet Baysal University in 3.02.2022** by

Examining Committee Members	**Signature**
Supervisor Assoc. Prof. Dr. Sevgi POLAT ALTINTAŞ Bolu Abant İzzet Baysal University	.....
Member Prof. Dr. Cabir TERZİOĞLU Bolu Abant İzzet Baysal University	.....
Member Prof. Dr. Muharrem GÖKÇEN Düzce University	.....
Member Assoc. Prof. Dr. Erhan BUDAK Bolu Abant İzzet Baysal University	.....
Member Assoc. Prof. Dr. Elif AŞIKUZUN Kastamonu University	.....

Prof. Dr. İbrahim KÜRTÜL

Director of Instıtute of Graduate Studies

ETHICAL DECLARATION

In this thesis dissertation that was properly prepared according to the Thesis Writing Rules of Bolu Abant İzzet Baysal University of the Institute of Graduates Studies, I hereby declare that;

- All data, information, and documents presented in the thesis were obtained in accordance with the academic and ethical rules,
- All data, documents, assessments, and results were presented in accordance with the scientific ethical, and moral rules,
- All works that were benefitted in the thesis were appropriately cited,
- No alteration was made in the data used,
- Study presented in this thesis is original,

Otherwise, I declare that I accept the loss of all my rights in case any contradiction that may arise against me.

Based on the plagiarism report that was generated on the date of 08/02/2022 by using predetermined filtrations set by Directorate of Institute of Graduate Studies of the Turnitin programme, a plagiarism detection sofware, the similarity index detected was 26 %.

_____

Sevgi KARADAVUT

ABSTRACT

STRUCTURAL AND MAGNETO-ELECTRICAL CHARACTERIZATION OF CATHODES BASED ON RARE-EARTH MANGANITES FOR SOLID OXIDE FUEL CELLS
PHD THESIS
SEVGİ KARADAVUT
BOLU ABANT IZZET BAYSAL UNIVERSITY
INSTITUTE OF GRADUATE STUDIES
DEPARTMENT OF PHYSICS
(SUPERVISOR: ASSOC. PROF. DR. SEVGİ POLAT ALTINTAŞ)

BOLU, FEBRUARY 2022

The subject of the thesis is highly spin-polarized rare earth element-based manganese perovskite structures. Lanthanum-strontium-manganese-oxide (LSMO) ceramics possess unique magnetic and electrical properties which have received lots of attention from researchers and producers of new materials. In addition to the effects of colossal magnetoresistance, magnetic refrigeration, magnetic memory, and magnetic hyperthermia applied in various fields of modern technology, they also possess parameters that make it possible to consider them as frequently used cathode materials for solid oxide fuel cells. In this dissertation, two series of manganite ceramics both produced by *B*-site substitution are explored. In the first series, *10 %* of *Mn* ions are replaced with various transition metals as *Cu, Co, Fe,* and *Ti* in the $La_{0.8}Sr_{0.2}MnO_3$ system and examined the structural, magnetic, and electrical-transport features. In the second series, the influence of iron content on the structural, microstructural, magnetic, and electrical-transport features of the ceramic perovskite manganites of the $La_{0.8}Sr_{0.2}Mn_{1-x}Fe_xO_3$ *(x=0.0, 0.05, 0.1, and 0.2)* system was investigated. A detailed analysis of the conduction mechanism behind the metal-insulator transition is also discussed. Analyzing structural and magneto-electrical features in these systems and obtaining enhancing physical properties bu B-site substitution offers a possibility to use them in technology.

KEYWORDS: Solid oxide fuel cell, manganites, magnetization, perovskite structure, temperature coefficient of resistance.

ÖZET

KATI OKSİT YAKIT PİLLERİ İÇİN NADİR TOPRAK ELEMENTİ BAZLI KATOTLARIN YAPISAL VE MANYETO-ELEKTRİKSEL KARAKTERİZASYONU
DOKTORA TEZİ
SEVGİ KARADAVUT
BOLU ABANT İZZET BAYSAL ÜNİVERSİTESİ
LİSANSÜSTÜ EĞİTİM ENSTİTÜSÜ
FİZİK ANABİLİM DALI
KATIHAL FİZİĞİ BİLİM DALI
(TEZ DANIŞMANI: DOÇ. DR. SEVGİ POLAT ALTINTAŞ)

BOLU, ŞUBAT - 2022

Tezin konusu oldukça spin polarize nadir toprak elementi bazlı manganez perovskit yapılardır. Lantanyum-stronsiyum-manganez-oksit (LSMO) seramikleri, yeni malzeme araştırmacıları ve üreticilerinden büyük ilgi gören benzersiz manyetik ve elektriksel özelliklere sahiptir. Modern teknolojinin çeşitli alanlarında uygulanan devasa manyeto direnç, manyetik soğutma, manyetik bellek ve manyetik hiperterminin etkilerine ek olarak, katı oksit yakıt hücreleri için sıklıkla kullanılan katot malzemeleri olarak değerlendirilmelerini mümkün kılan parametrelere de sahiptirler. Bu tezde, her ikisi de *B* bölgesi yer değiştirmesi ile üretilen iki seri manganit seramiği araştırıldı. İlk seride, $La_{0.8}Sr_{0.2}MnO_3$ sisteminde *Mn* iyonlarının *%10*'u *Cu, Co, Fe* ve *Ti* gibi çeşitli geçiş metalleri ile değiştirildi ve yapısal, manyetik ve elektriksel taşınım özellikleri incelendi. İkinci seride, $La_{0.8}Sr_{0.2}Mn_{1-x}Fe_xO_3$ *(x=0.0, 0.05, 0.1 ve 0.2)* seramik perovskit manganit sisteminde demir içeriğinin yapısal, mikroyapısal, manyetik ve elektriksel taşınım özellikleri üzerindeki etkisi araştırıldı. Ayrıca metal-yalıtkan geçişinin arkasındaki iletim mekanizmasının ayrıntılı bir analizi tartışıldı. Yapısal ve manyeto-elektriksel özelliklerin araştırılması ve B-bölgesi yer değiştirilmesiyle iyileştirilen fiziksel özelliklerin bulunması bu malzemelerin teknolojide kullanılmasına olanak sağlamaktadır.

ANAHTAR KELİMELER: Katı oksit yakıt pili, manganitler, manyetizasyon, perovskit yapı, direnç sıcaklık katsayısı

TABLE OF CONTENTS

LIST OF FIGURES

Page

LIST OF TABLES

Page

LIST OF PICTURES

Page

LIST OF ABBREVIATIONS AND SYMBOLS

AFI **:** Antiferromagnetic insulators

AFM **:** Antiferromagnetic

AMR **:** Anisotropic magnetoresistance

au **:** Arbitrary unit

CMR **:** Colossal magnetoresistance

CO **:** Charge ordering

e-e : Electron-electron

e-p : Electron-phonon

FC **:** Field-cooled

FM **:** Ferromagnetism

GMR **:** Giant magnetoresistance

H_C **:** Critical magnetic field

HS **:** High Spin

K **:** Kelvin

LSMO **:** $La_{1-x}Sr_xMnO_3$

MR : Magnetoresistance

Oe : Oersted

OO : Orbital ordering

PM : Paramagnetic

T_C **:** Curie temperature

TCR : Temperature coefficient resistance

T_{MI} **:** Metal-insulator temperature

TM **:** Transition metal

TMR **:** Tunneling magnetoresistance

T_N **:** Néel temperature

SEM **:** Scanning electron microscope

XRD **:** X-ray diffraction

ZFC **:** Zero Field Cooled

This dissertation is devoted to only my daughter; Zimra...

ACKNOWLEDGEMENTS

Firstly, I want to explain my deepest thankfulness to my advisor Dr. Sevgi POLAT ALTINTAŞ for her guidance, advice, and criticism during all investigations. She always encouraged me and shared her constructive remarks on the thesis. In particular, I would like to thank for her friendly help when needed, for her patient throughout this work.

I also explain my sincere appreciation to Dr. Cabir TERZİOĞLU to provide the instruments needed to work in the laboratory. Also, I would like to thank Dr. Nevin SOYLU for measurements in the laboratory and also teaching me how to use the instruments. I also want to express my gratitude her for the time and energy she reserved to me. Special thanks go to Dr. Fatih DENBRİ for helping me with Jana refinement, grain size analysis from SEM photos, and conduction mechanism analysis.

I would like to thank my thesis committee members for their guidance and assistance through this process. Of course, their discussion, comments, ideas, and especially feedback have certainly been invaluable to interpret and improve the results obtained.

I am also very grateful to Eren GÜNKAYA, Erpiliç Advertising Manager for several figures design.

I would like to thank my best friends being especially Büşra GÜNKAYA, Hacer COŞKUNYÜREK, Merve MAN KARAYAKA, and Sinem YILDIZ for their moral support, nice conversation, constant encouragement, and prayers throughout this process.

I express sincere appreciation to my parents, Sevim BAL and Bünyamin BAL. Especially, I would like to thank my father countless times for his encouragement to finish my Ph.D. Without his sacrifice and love, I would not be where I am today. I am also very grateful to my sisters, Sibel BAL and Sümeyye BAL. They supported me in all aspects of my life with love. Special thanks go to my husband Dr. Yüksel KARADAVUT for being here for me with his love,

continued support, and prayers. Finally, I would like to thank my daughter, Zimra KARADAVUT for shining in her eyes…

This study was supported by the Bolu Abant Izzet Baysal University Foundation through the project 2021.03.02.1485.

1. INTRODUCTION

Ceramic manganites possess unique magnetic and electrical properties which have received lots of attention from the researchers and developers of new materials, recently (1) (2) (3) (4) (5). In addition to the effects of colossal magnetoresistance, magnetic refrigeration, magnetic memory and magnetic hyperthermia (6) (7) (8) (9) applied in various fields of modern technology, they also possess parameters that make it possible to consider them as promising cathode materials for solid oxide fuel cells (10) (11).

$La_{1-x}Sr_xMnO_3$ *(LSMO)* is a kind of perovskites having an ABO_3 crystal structure which is derived from the combination of $LaMnO_3$ and $SrMnO_3$ *(i.e. A: La and Sr, B: Mn).* In such a combination, the La^{3+} ion can be replaced by Sr^{2+}. The replacement may give rise to the formation of electron acceptors and the valence of the manganese ions to change from $3+$ to $4+$ (12) (13) (14). Due to such doping effects, the manganites show phase transitions with respect to the temperature. One of them is the magnetic phase transition from ferromagnetic to paramagnetic phase at the Curie temperature T_C, while the other is the metal-insulator phase transition occurs generally at temperatures close to T_C (12) (13) (14). The physical features exhibited by *CMR* manganites are mainly originated from chemical substitution. It is found that the orderings of the cation and dopants have decisive effects of such properties (15) (16) (17) (18) (19). The chemical substitution, having random spatial locations, leads to the manganite system to generate certain disorders. In *LSMO* system, a number of studies have revealed the effect of the substitution particularly in the range $x=0.1–0.3$ due to having important applications in solid oxide fuel cells (10) (11). A particular interest requires to be devoted to the samples with $x=0.2$ due to the existence of having ferromagnetic to paramagnetic phase transition close to room temperature $(T_c \sim 325\ K)$ (20) (21).

CMR in manganites is mainly originated from the Jahn-Teller type distortions and *DE* interaction between Mn^{3+} and Mn^{4+}. So, investigating the effect of manganese-site substitution is very curicial to understand the origin interactions. For this purpose, many studies have studied the substitution of *B*-site by transition metals as ***Cu*** (22) (23) (24) (25) (26) (27) (28) (29) (30), ***Co*** (31)

(32) (33) (34) (35) (36), ***Fe*** (37) (38) (39) (40) (41) (42) (43) (44) (45) (46), ***Ti*** (47) (48) (49) (47) (50) (51) (52) (53) (54) (55) (56) (57), etc. The common findings in these studies are the substitution of manganese with transition metals in the lanthanum-based manganites systems results a lowering in Curie temperature, T_C, an increment in the resistance, and for higher doping regimes, getting insulating phase and/or cluster-glass-like state *(~T<50 K).* As per the best of our knowledge, there is no detailed study that reports the optimum amount of transition metal substitution on the *B*-site that enhances magnetoresistivity properties of the $La_{0.8}Sr_{0.2}MnO_3$ ceramic system.

The dissertatition consists of five main chapters. The first chapter is introduction of the thesis which gives the general information of the solid oxide fuel cell *(SOFC)* and includes the overwiev. Also, each chapter is briefly summarized. The second chapter is theoretical part which involves history and the basic theoretical background of perovskite manganites as the detailed presentation of the chemical, electronic, structural, and magnetic composition. The various magnetic couplings, exchange interactions and properties as well as main models (metal-insulator transition, magnetoresistance, etc.) is explained in detail. The third chapter which is materials and methods, is described experimental set up, preparation of the samples and all measurements techniques. The fourth chapter named result and discussion, divided into two groups due to having two series of samples. The structural, electrical, and magnetic transport properties and conduction mechanism of the two series of samples are analyzed one by one in this part. Finally, the highlights of main results and suggestions of the thesis are given in the last chapter.

1.1 Solid Oxide Fuel Cells *(SOFC)*

Solid oxide fuel cell *(SOFC)* technology has a wide range of power generation execution areas (58). The importance of *SOFC* arises from its high yield and clean production of electricity from a diversity of fuels. It has developed as an energy conversion device to obtain a high yield of over *70%* with remodeling (59). This technology has been extensively studied because it has so low emissions to the atmosphere and fuel flexibility like hydrogen, natural and coal gas, etc. (60). At present, the attractiveness of *SOFC* is getting rise up due to a broad discussion

about increasing climate change day by day and the end of the energy resources (61). *SOFC* ensures a lot of benefits over traditional energy conversion systems containing high efficiency, modularity, reliability, fuel adaptability, and very low levels of SO_x and NO_x emissions (62) (63).

SOFCs are electrochemical equipment that fabricates electricity by converting from the chemical energy of a fuel to oxidant into electrical energy directly (64). *SOFCs* are much more yield and environmentally harmless than conventional electric power generation operations because they fabricate electricity through an electrochemical reaction and not through a combustion operation.

Every *SOFC* has two electrodes that one is positive and the other one is negative, called as anode and cathode respectively (65). The main structure of a *SOFC* includes a solid electrolyte (usually a ceramic) that is located between anode and cathode (66). As for how it works, fuel is sent to the anode, and oxidant, typically air, is given to the cathode (67). These reactions that produce electricity occur at the electrodes. The electrodes have solid porous structures (68). So, it allows the fuel and air to diffuse to the electrolyte and the outputs of the electrochemical reaction on the anode part to diffuse away from the electrolyte. The electrolyte transmits the oxygen ions occurred by the electrochemical reduction of molecular oxygen from the cathode part to the anode part of the *SOFC.* Fuel penetrates through the anode to the anode/electrolyte interface. The oxygen ions are reacted by the fuel catalytically. Each cell is connected in electrical series to increase power and voltage. They can be stacked to obtain an optimal stack magnitude. A series of stacks can be ordered within an enclosure to compose a *SOFC* module. Single or multiple modules may be banded together and integrated with subsystems to send out air and fuel, to recycle heat, and to convert the fabricated electricity from direct current *(DC)* to alternating current *(AC)*, to obtain a *SOFC* power system. Fig. 1.1 shows the schematic diagram of a fuel cell.

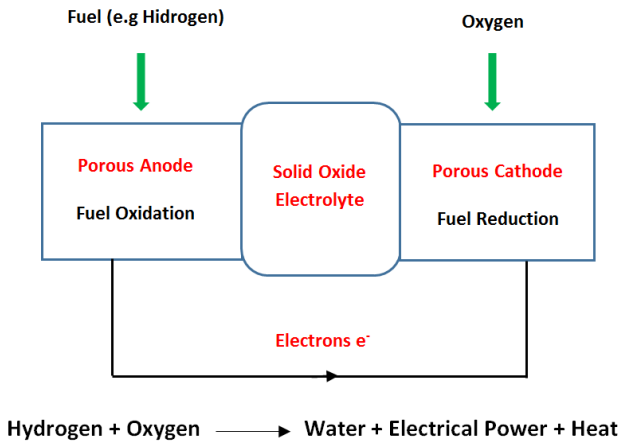

Figure 1.1 Schematical chart representing the general working principles of a fuel cell.

2. THEORETICAL INFORMATION

2.1 Overview

Transition metal oxides *(TMO's)* generate one of the most attractive types of inorganic solid displaying stimulating physical properties such as magnetic and optical resultant, structural, electrical transport due to the intense electron correlation in the systems. *TMO*'s have some remarkable phenomena such as high Curie temperature *(T_C)*, metal-insulator transition temperature *(T_{MI})*, kinds of magnetoresistance *(MR)* such as colossal magnetoresistance *(CMR).* These intrinsic complexes of those materials can cause the varieties of features and performances (69) (70). Metal oxides display an extensive range of properties in respect of functionalities, e.g., from semiconducting-insulator to conductor or superconductor, from antiferromagnetic-paramagnetic to ferromagnetic; from dielectric to ferroelectric, etc. due to having a multi-interactive coupling of the orbital, spin, charge, and lattice.

The manganese oxides that have the perovskite lattice structure, are broadly called 'manganites' are the most significant interacting systems (71). Perovskite manganite oxides are greatly matchless systems in materials so-called "strongly electron-correlated system" (72). Manganites possess a wide diversity of phases with orbital ordering, unusual spin, lattice, and charge. Perovskite-structured manganese oxide by the general formula of $A_{1-x}B_xMnO_3$ (where *A* is usually a lanthanide rare earth element and *B* is usually a divalent alkaline earth metal ion) compounds have raised great interest since its discovery due to their complex *CMR* and magneto-electrical features (73). These materials exhibit an interesting correlation by changing temperature, pressure, substituting, doping or applied magnetic field, etc. (74). Several major studies have proved that electromagnetic behavior manganites depend on the mixed valance state Mn^{3+}/Mn^{4+} play a considerable role in the electronic configuration. So, any perturbations on the valence of *Mn* ions cause the material from insulating to metallic and paramagnetic to ferromagnetic states (75). It is usually known that the physical features of the hole-doped-mixed valence manganites are directed by the close interaction among orbital degrees of freedom, lattice, spin, charge, and nanoscale inhomogeneities among competing phases (76).

2.2 History

Over the last few decades, among all oxide materials, manganites have emerged as one of the most engaging investigation fields for condensed matter physicists and material scientists. The mixed-valence manganese oxide perovskites also known as manganites discovered by Hary Jonker and J. H. van Santen in 1950 (77). They crystallized the first mixed-valence manganites and explained the preparation process, crystal structure, and magnetic features of the $(La_{1-x}Ca_x)MnO_3$ *(LCMO)* series, and rendered a major report of the electrical resistivity (78). Then, analogue significant results were derived for the $(La_{1-x}Sr_x)MnO_3$ *(LSMO)* and $(La_{1-x}Ba_x)MnO_3$ series with the range of solid solution was limited to $x<0.7$ or $x<0.5$ respectively. In 1951, Zener declared the interaction between electrons in the *d*-shells in ferromagnetic manganites. Hence, the idea of double exchange, which is believed to be the principal mechanism in these materials, was introduced. In 1954, *MR* and all transport properties were clarified by Volger and he remarked that the magnetoresistance of $(La_{0.8}Sr_{0.2})MnO_3$ is negative with a peak near the Curie temperature (79). In 1955, Wollan and Koehler executed a wide neutron diffraction researches on $(La_{1-x}Ca_x)MnO_3$ and, they clearly indicated the presence of ferromagnetic *(FM)* and antiferromagnetic *(AFM)* regions and the simultaneous occurrence of *FM* and *AF* regions in the *LCMO* system occasionally (80). In 1969 and 1970, prominent researches of flux-grown single crystals of $(La_{1-x}Pb_x)MnO_3$ with $0.2<x<0.44$ was performed by Searle and Wang (81) (82), Morrish et al. (83), and Leung et al. (84). They exposed the metallic conductivity below T_C and an enormous negative *MR* effect of about *20%* at *1 T* in the vicinity of T_C. Moreover, Goodenough and Longo expressed the theoretical predictions for the origin of the magnetic ordering and predicted an orbital and charge-ordered state in 1970 (85). In the 1990s, the relevance in the mixed-valence manganites continued by the fabrication of high-quality thin films with large *MR* by von Helmholtz et al. (86) and Chahara et al. (87). They interpreted the magnetoresistance in $La_{0.67}Ba_{0.33}MnO_3$, which was about *60%*. Then, the researches increased with the papers by McCormack et al. in 1994 (88). In the same year, Jin et al. printed that optimized films show particular magnetoresistance effects near T_C. They obtained a huge magnitude of magnetoresistance exceeding *99.92%* at *77 K* for a film made

of $La_{0.67}Ca_{0.33}MnO_3$ and it was named colossal magnetoresistance *(CMR)* (89). In 1998, inclusive research about metal-insulator transitions was printed by Imada et al (90). Then in 1999, Coey et al. analyzed broadly various parts of manganite physics, such as analyzing the electronic transport behavior, electronic ground states, the external impacts like pressure and temperature (91). In 2001, Salamon & Jaime pointed out the double exchange mechanism especially and the missing elements that cause a ginormous regeneration of curiosity in related materials (92) (93). In 2003, Dragotta and his group explained a detailed report about the phase separation in *CMR* and *CMR* systems (94). In 2006, Tokura (95) (96) and in 2008, Siwach et al. (97) were published papers about metal-insulator transition *(MI)* at temperature T_{MI}, paramagnetic-ferromagnetic *(PM-FM)* transition at Curie temperature (T_C), *CMR*, antiferromagnetism *(AFM)* at Néel temperature (T_N), charge ordering/orbital ordering *(CO/OO)* at T_{CO}.

Although researchers find out and utilize manganites proceed, much of nowadays' effort focuses on the mesoscopic formation and phase separation. In the past a few decades, a diversity of techniques on manganites have been improved on a length scale range of microns down to angstroms. This substantiality and exciting area are still being tried to explain and these compounds are the major example of the interaction between theory, experiment, and execution which are the heart of Condensed Matter and Materials Physics.

2.3 Perovskite Crystal Structure

The ideal manganese perovskite materials that display a cubic symmetry, are formalized by the general chemical form of $A_{1-x}B_xX_3$. In general, *A* is usually an alkali earth element *(Ca, Ba, Sr, etc.)* or a rare-earth element *(La, Pr, Sm, Gd, etc.)* and *B* could be *3d, 4d,* and *5d* transitional metal elements *(Mn, Ti, Co, Fe, etc.)* and *X* is an anion such as *(O, F, Cl)*. In this thesis, $La_{1-x}Sr_xMnO_3$ is chosen as the pristine sample which crystallizes in the cubic perovskite form as modeled in Figure 2.1 (98). The *B*-type ions (Mn^{3+}/Mn^{4+}) take place in the vacancy at the centers of the octahedral cages generated by *O* atoms meanwhile the *A*-type ions $(Sr^{2+}, Ca^{2+}, Pr^{3+}, La^{3+}, etc.)$ settle at the corners of the unit cell. Thus, the *B*-type ions fill at the center, the *O*-type ions sit at the face center (99). The *A*-type ions seat at the corners of the cube in the center-symmetrical cubic perovskite systems.

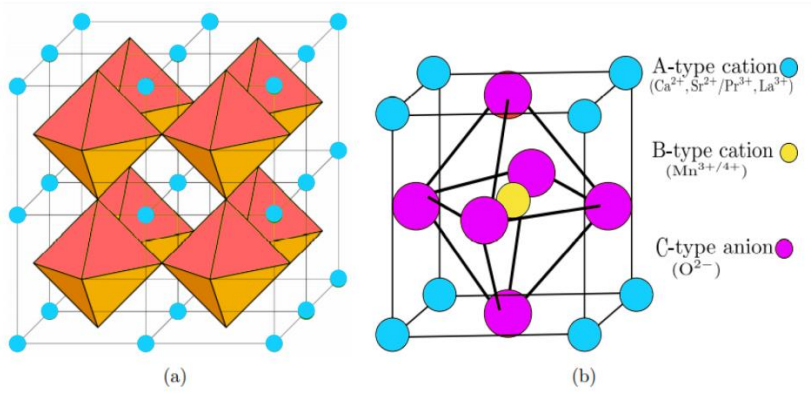

Figure 2.1. Crystal structure of $A_{1-x}B_xMnO_3$ manganese perovskite system. (a) The model of ABO_3 type perovskite oxides in *3-D* cubic system (b) The model of a single unit cell of perovskite-manganite with *C*-type O^{2-} anions and *B*-type $Mn^{3+/4+}$ cations, in the existence of *A*-type cation.

As shown in Fig. 2.1, the geometric structure can be depicted using a cubic unit cell with *A*-site ions located at the corners *(0, 0, 0)* and *B*-ions sitting at the body center *(½, ½, ½).* The oxygen ions settle at the face center *(½, ½, 0).* So, the structure of the octahedron forms around the *B* ions. It is a fact that the crystal structure correlates with the elements in a compound. Furthermore, the *A*, *B*, and *O* atoms have *12*, *6*, and *6* coordination numbers respectively.

Another essential point to understand manganites' structure and behavior is the 'tolerance factor, *t*. The crystal symmetry which is characterized by a perovskite compound depends on the relative size of its constituent elements. And, it is defined by Goldschmidt's tolerance factor as shown below (100) (101);

$$t = \frac{r_A + r_B}{\sqrt{2}\,(r_B + r_X)} \tag{1}$$

where r_A, r_B, and r_X are the effective ionic radii of rare earth elements, *Mn* ions, and oxygen, respectively. The tolerance factor *t* forecasts the stability of the perovskite phase approximately. The perovskite system form while the values of *t* are close to *1*. Thus, the tolerance factor can be used to categorize the perovskite distortions roughly (102):

- The top limit of the tolerance factor is approximately *1.04.*
- Cubic phase is expected for $0.9 \leq t \leq 0.97$
- The tetragonal or hexagonal phase is expected for $0.97 \leq t\ 1.02$
- Orthorhombic phase is expected for $0.8 \leq t \leq 0.9$

The lanthanum manganite family with the $LaMnO_3$ formula has an orthorhombic structure with $t=0.89$. Substituting larger ions like Ba^{2+} or Sr^{2+} for La^{3+} causes to the transition of a cubic structure because of increasing t value. This kind of substitution incurs a rise in the volume of the unit cell which creates distortions in the structure. These distortions cause a variance of the electronic and magnetic properties in the system (77).

In this thesis, $La_{1-x}Sr_xMnO_3$ *(LSMO)* is taken by the pristine sample. Substituting Cu^{2+}, $Co^{2+/3+/4+}$, $Fe^{2+/3+/4+}$, and Ti^{4+} ions modify the tolerance factor which significantly affects the structural and magneto-electrical properties. One can find the ionic radii of considered ions in Table 2.1 which are used for calculation *t*.

Table 2.1.Ionic radii in Cu^{2+}, $Co^{2+/3+/4+}$, $Fe^{2+/3+}$ *and* Ti^{4+} -substituted lanthanum manganite perovskites. The *A*-site cation radii are presented for twelve-fold and nine-fold coordination numbers (separated by comma), while the *B*-site cation radii are presented for six-fold coordination numbers (103).

A-site (Å)		B-site (Å)	O-site (Å)
		Mn^{4+} → 0.53	
		Mn^{3+} → 0.64	
La^{3+}	1.36, 1.216	Cu^{2+} →0.73	
		Co^{2+} →0.65 (HS), 0.745 (LS)	
Sr^{2+}	1.45, 1.31	Co^{3+} →0.545 (HS), 0.61 (LS)	O^{2-} → 1.4
		Co^{4+} →0.53 (HS)	
		Fe^{2+} → 0.61 (LS), 0.78 (HS)	
		Fe^{3+} →0.55 (LS), 0.645 (HS)	
		Fe^{4+} →0.585	
		Ti^{4+} → 0.605	

2.4 Crystal Structure of Lanthanum-Strontium-Manganese Oxides, $La_{1-x}Sr_xMnO_3$

Manganese perovskite systems in the form of $La_{1-x}Sr_xMnO_3$ *(LSMO)* are major compounds since they exhibit unique magnetic and transport properties in the present times (86) (104) (105). *LSMO* family compounds which have an unusually high-powered correlation between the spin, charge, and orbital possess substantial properties ranging from insulating/nonmagnet (paramagnetic or antiferromagnetic) paramagnetic insulating or metallic, ferromagnetic metallic, ferromagnetic conducting states.

The cubic perovskite structure of $La_{1-x}Sr_xMnO_3$ formed with a corner shared octahedral in the unit cell with *A* and *B* cations (12-coordination) and *6* oxygen anions (6-coordination). Doping *B* cations lead to an operative change in ferromagnetic ordering and conductivity at the same time. The phase diagram by doping concentration versus temperature graph and also all phase regions *(PMI, FMI, and FMM)* are given in Fig. 2.2 (106).

The primary sample $LaMnO_3$ is an insulator for all temperatures however, it exhibits paramagnetic properties at high temperatures, whereas it shows antiferromagnetic properties at low temperatures. When the doping is raised yet, approximately *x=0.1*, it remains an insulator for low-temperature range however, all spins become aligned, and it is the ferromagnetic state. Subsequently, for low-temperature state, it is a ferromagnetic metal at the *x=0.33* concentration, and it is a paramagnetic insulator in the high temperature state (107).

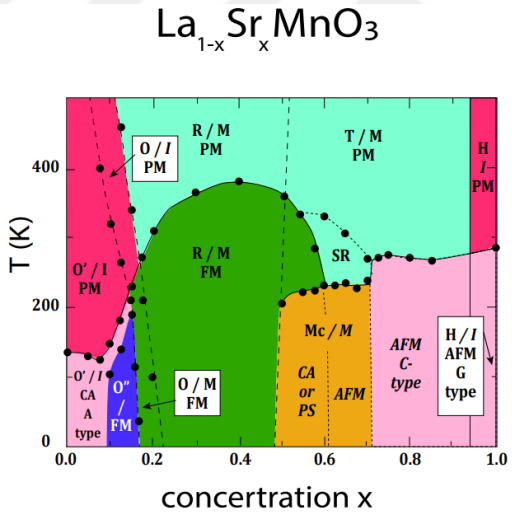

Figure 2.2. Phase diagram of *LSMO* compound with varying *x*-concentration. While $LaMnO_3$ is an insulator at all temperatures, increasing the doping of strontium to *x=0.33* incurs a metal-insulator transition at *~350K* (107). The abbreviation in the figure can be seen on the Appendix page.

The phase graph of the *Sr*-doped manganite $La_{1-x}Sr_xMnO_3$ is fairly complex because of displays multiplicity phases. The basic sample $LaMnO_3$ is a predominantly correlated insulator exhibiting anti-ferromagnetic and orbital ordering. It is considered that both the Jahn-Teller effect and Coulomb repulsion support the insulating behavior. *Sr* doping finds out charge carriers and prevents the long-range Jahn-Teller distortion (108).

2.4 Interactions in Manganites

The manganites which are mixed metal oxides containing manganese, include the main properties of charge ordering, colossal magnetoresistance and, metal-insulator transitions. These characteristic features are derived from intense electron-electron *(e-e)* interactions, electron-phonon *(e-p)* and magnetic interactions. Various significant interactions occur in these manganites among charge, orbital, spin, and lattice as Jahn-Teller Effect, Indirect (Super Exchange) Interaction, and Double Exchange Interaction. Such interactions and distortions take part in the electromagnetic properties, phase separation, charge ordering, half metallicity, and magnetoresistive properties of manganites (79).

2.4.1 Double Exchange Mechanism

Along with the discovery of the connection between ferromagnetism and electrical conductivity in manganites (77), Clarence Zener explained the double exchange mechanism in a series of papers (76) (12) (109). He proved that the existing magnetic exchange models failed to explain the situation in manganites and declared what is now known as the 'double exchange'. This mechanism can be defined as an interaction that occurs between two unequal Mn^{3+}/Mn^{4+} ions in mixed-valent perovskites through an oxygen atom.

The neighbor manganese spin moments are related with to the kinetic exchange between the e_g-electrons in the double exchange mechanism (110). In the main compound, $LaMnO_3$ (superexchange, insulating antiferromagnet), the valence state of *Mn* ion is *3+*. The *Mn* ion exceeds a mixed-valence state Mn^{3+}/Mn^{4+} by doping a divalent element such as Pb^{2+}, Ca^{2+}, Ba^{2+}, Sr^{2+}. The e_g electron of Mn^{3+} jumps to *O p*-orbital simultaneously thus, the electron fill in the empty *O p*-orbital. Then, the electron at the same spin which forms *O p*-orbital again jumps to the empty e_g orbital of Mn^{4+}. In other words, hole transfer between the adjacent *Mn* ions is as follows: the e_g electron transfers from the Mn^{+3} ion to the oxygen atom then, to the Mn^{+4} ion and vice versa (111). This interaction is known as the "double exchange mechanism" (112). The jumping of e_g electrons from Mn^{3+} to Mn^{4+} is crucial to the conduction treatment and the ferromagnetic coupling in doped manganites (86).

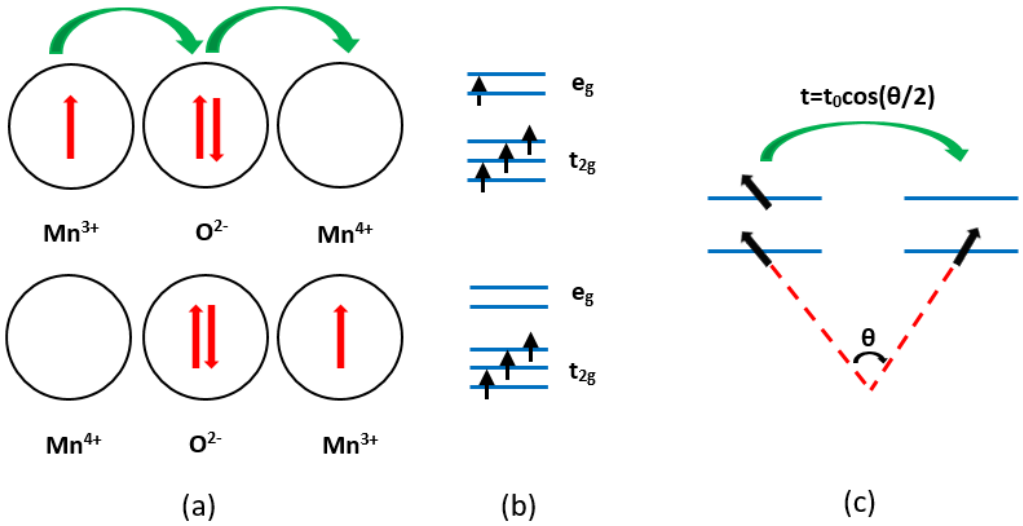

Figure 2.3. (a) Diagram of the Double Exchange mechanism that consists of the two *Mn* ions and one *O* ion. (b) The dynamism of e_g-electrons enhances if the localized spins are polarized (c) Intersite hopping parameter (113).

The electron hopping probability alters depending on the cosine θ between two spins in adjacent e_g orbitals. This leads to a larger mobile electron transfer at a lower θ. The external magnetic field can sequence the core spins from pristine disorder states to a higher-order state. Afterward, electron hopping occurs and a decrease in resistivity is seen. Namely, the arrangement of the manganese spins with external applied magnetic field results in increasing conductivity.

It is known that all individual ion or atom is constrained to align by a ferromagnetic Hund (Hund's rule) coupling. The conduction electrons do not replace their spin when they travel from ion to ion. These electrons act in a jumping manner in the crystal while the net spins of the incompleted *d* shells are parallel. In short, the conduction electrons cause to fall their kinetic energy if the background of the *d* shell spins or the t_{2g} spins of manganite is completely polarized.

The occurrence of metal-insulator transition behavior of $La_{1-x}A_xMnO_3$ mixed-valence manganites is clarified by Double Exchange interaction which appears in consequence of intense exchange interaction between the itinerant e_g electrons (or holes) and localized t_{2g} spins through the *Mn-O-Mn* path. In such a case, these exchange interactions can be infinite only in the case of the parallel alignment of the *t*-core spins which lays in the same direction for both Mn^{3+} to

Mn^{4+} ion. Hence, the spin direction does not alter during the hopping case. Moreover, according to Hund's rule, the antiarrangement of the unpaired electrons is not permitted. In reality, the *t*-core electrons are restricted. So, they can not participate in conduction whereas, e_g electrons may be bordered or itinerant. Thereby, only e_g electrons can participate in conduction during the hopping process. In this process, the e_g electron transfer depends on relative angle, θ between *Mn t*-core spins. Their formalism has illustrated that $t_{eff} = t\cos\theta/2$, where t_{eff} is the effective jumping of an electron between two nearest-neighbors *Mn* ions, θ is the angle between t_{2g} spins settled at the two *Mn* sites involved in the electron transfer.

2.4.2 Jahn-Teller Effect

A fundamental resource of complexity in manganites is the atomic structure. The incompleted shell of the *Mn* cation has a structured function in the electrical and magnetic properties of manganite like other transition metal oxides (114). Crystal-field splitting is liable for lifting the degeneracy of the *5*-fold degenerated states. *3d* energy levels of cations of transition metal complexes surrounded by oxygens generating octahedron are split into two levels: double degenerated e_g level and triple degenerated t_{2g} level. And also, the splitting energy of the crystal field is about *1 eV*. In addition, the Jahn-Teller lattice distortion can lead to further degeneration of the t_{2g} and e_g orbitals to d_{xy}, d_{xz}, d_{yz}, and $d_{x^2-y^2}$, $d_{3z^2-r^2}$ respectively. But, the ferromagnetic Hund's rule coupling energy which is about *2-3 eV*, is higher than the crystal field splitting energy so, the high spin state is actualized. The crystal-field splitting of the five-fold degenerate *3d* orbitals in *Mn* cations is illustrated in Fig. 2.4 (115) (96).

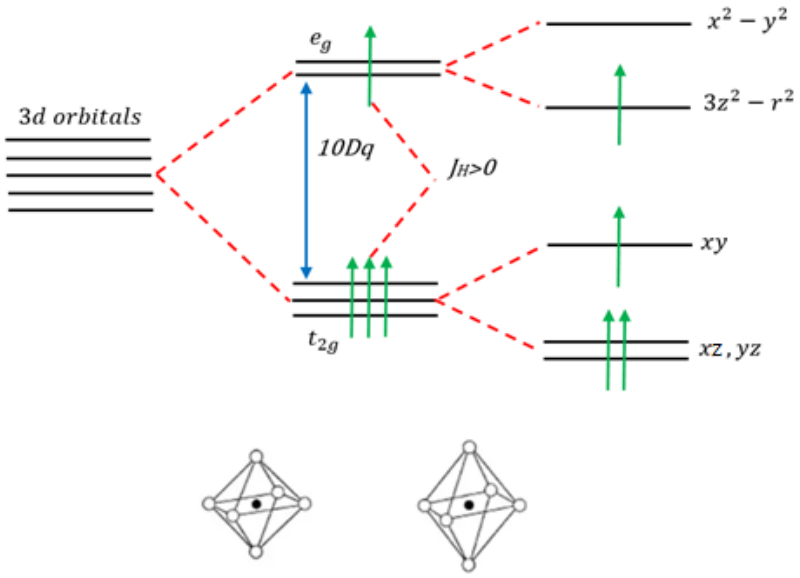

(a)

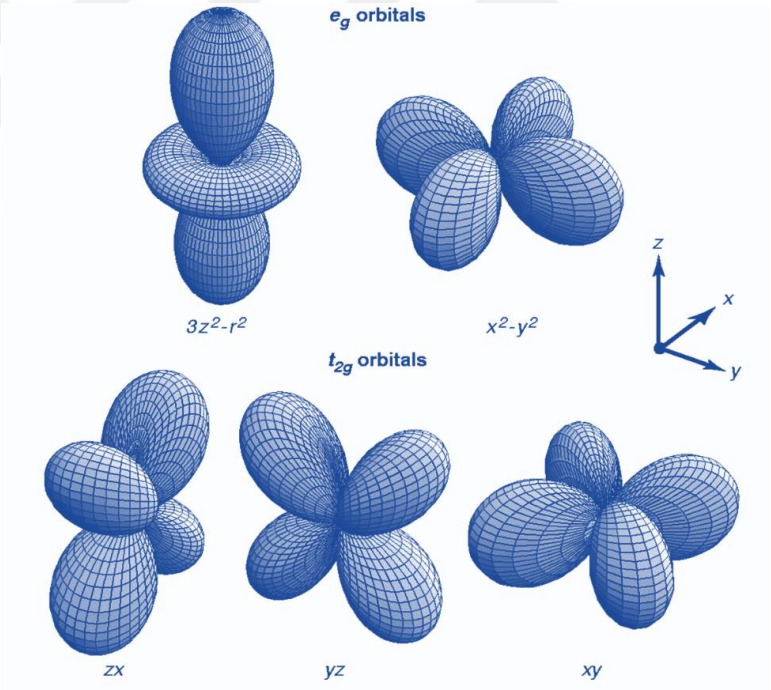

(b)

Figure 2.4. (a) The splitting of e_g and t_{2g} energy levels because of Jahn-Teller distortion. Here, J_H stands for Hund's coupling between orbitals. (b) The five *d* orbitals of Mn^{4+} and Mn^{3+} in a crystal field of octahedral symmetry: e_g orbitals ($d_{x^2-y^2}$, $d_{3z^2-r^2}$) and three t_{2g} orbitals (d_{xy}, d_{xz}, d_{yz}).

As seen in Fig. 2.4 part (a), in *d* electron manifold, the ground state splits as *3* electrons in the lower t_{2g} levels and *(1-x)* electron in the higher e_g level due to the crystal field. *x* stands for the *Sr* doping concentration in the compound of *LSMO*. While the e_g levels are occupated separately, for example as is the case in Mn^{3+}, this can lead to Jahn-Teller lattice distortion. For this reason, it splits the e_g energy levels into two assigned by an energy E_{JT}.

In Fig. 2.4 part (b), angular wave functions of the e_g and t_{2g} orbitals are seen. The orbital degeneracy of the e_g electrons occurs due to the motion of oxygen ions from their original positions for manganite materials. *21* modes of vibration for the motion of oxygen and *Mn* ions are known (116). But, only two modes of vibrations cause the splitting of the e_g doublet. These two types of distortions which are represented by Q_2 and Q_3 are related to the Jahn Teller effect. The distortion Q_3 is a tetragonal distortion that ensues an elongation or contraction of the MnO_6 octahedron concerning the occupied $3d_{3z^2-r^2}$ or $3d_{x^2-y^2}$ orbital. The distortion Q_2 is an orthorhombic distortion acquired by a significant superposition of the $3d_{3z^2-r^2}$ or $3d_{x^2-y^2}$ orbitals (117). The turnings of the octahedra are obtained in the deviation from 180^o of the *Mn-O-Mn* tilting angle and, Jahn Teller lattice distortion in $LaMnO_3$ is influenced by the Q_2 distortion.

The structure of the undoped compound of $LaMnO_3$ is shown in Fig. 2.5. All manganese atoms are placed on the Mn^{3+} configuration with three electrons in the t_{2g} band and one electron in the e_g band (112). At this stage, electrons can not act between ions due to intense Coulomb repulsion between them and thus, $LaMnO_3$ is a Mott insulator. After doping *Sr* concentration, La^{3+} ions replace with Sr^{2+} ions and thus, some manganese ions convert into Mn^{4+} to compensate. In this doped case, the e_g band is empty, which allows the probabilty for electrons to travel from the Mn^{3+} and Mn^{4+} ions.

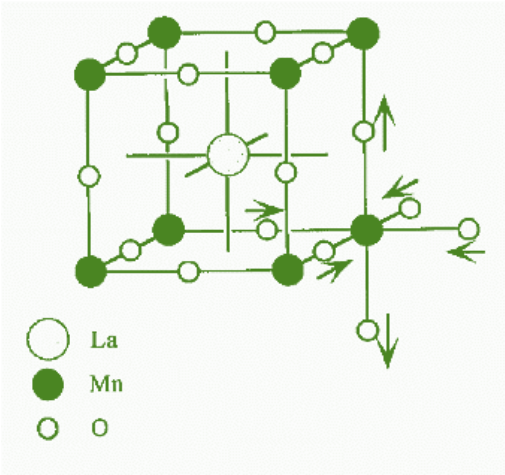

Figure 2.5. The exhibition of the oxygen ions surrounding the manganese ions in the perovskite structure of $LaMnO_3$. The arrows point to one possible Jahn-Teller distortion.

2.4.3 Indirect Exchange (Superexchange) Interaction

Superexchange *(SE)* interaction is suggested by H. A. Kramer to explain the magnetic properties of transition metal oxides (118). *SE* interaction is described as an indirect exchange interaction between non-adjacent magnetic ions *(Mn)* with the same valance separated by a nonmagnetic ion *(O)*. Ferromagnetism in manganites oxides may be clarified by *SE* interaction besides *DE* interaction (119). The distance between magnetic ions is far away from the direct exchange interaction. Thus, *SE* interaction occurs between *Mn* ions from the same *2p* oxygen orbital that has antiparallel spins concerning Pauli exclusion principle leading mostly to antiferromagnetism. That interaction occurs only *t-core* spins of the magnetic ion which has an anti-parallel alignment. In the state of *MnO* or ABO_3, the ↑spin *p*-electron can hop to the left, cation *A*. Hence, the configuration of *d*-spins is either in parallel ↓↓ or anti-parallel ↓↑. In such a circumstance, the parallel configuration costs more energy and falls foul of the Pauli Exclusion principle so, the effective exchange is antiferromagnetic. Whereas, the geometry of the internal, e.g. 180^o bond angle $(M\text{-}O^{2-}\text{-}M)$ usually creates the strongest strength of the anti-parallel coupling between metal ions *M*, plays a major role, and can even decide the sign of the interaction. One another instance is $LaMnO_3$ that involves only Mn^{3+} ions. The $LaMnO_3$ has an *A*-type antiferromagnetic structure where ferromagnetic $Mn^{3+}\text{-}O\text{-}Mn^{3+}$ superexchange concludes within

parallel lattice planes and ensures a well-enough ordering of the movement of the filled e_g orbitals, with adjacent planes coupled antiferromagnetically (120) (121).

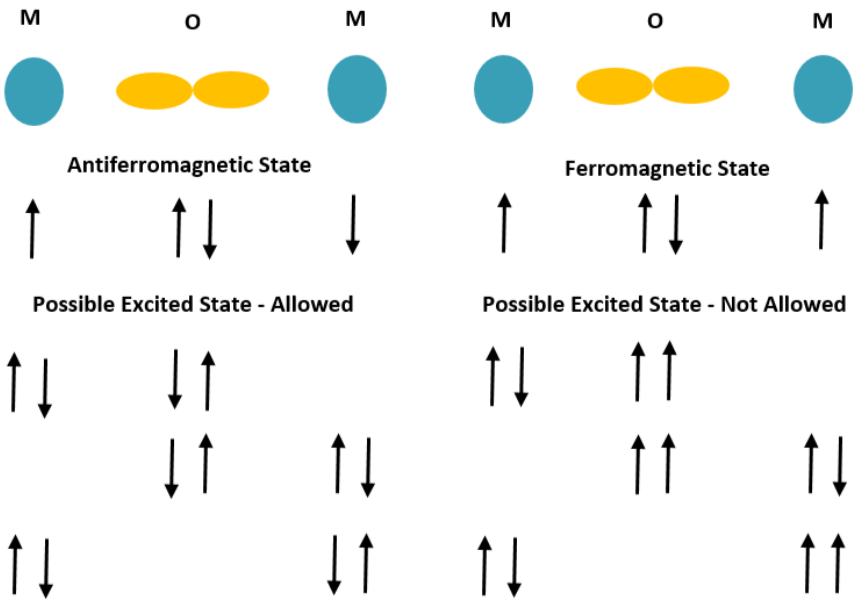

Figure 2.6. Superexchange Interaction.

2.5 Magnetoresistance *(MR)* Phenomena

Magnetoresistance *(MR)* is described as the change of resistance of compounds subjected to an external magnetic field. Another saying, it is the ratio of the change in resistivity of an external magnetic field. Although the resistivity of some materials only is subjected to temperature, the resistivity of some materials is subjected to the value of the applied magnetic field. The equation of the magnetoresistance can be written as;

$$MR = \frac{\rho(H)-\rho(0)}{\rho(0)} \quad (2)$$

where $\rho(H)$ is resistivity in an applied magnetic field and $\rho(0)$ is resistivity in zero applied magnetic field.

Magnetoresistance is classified into five groups: giant magneto-resistance *(GMR)* and colossal magneto-resistance *(CMR)*, tunneling magnetoresistance (TMR), anisotropic magnetoresistance *(AMR)*, and extraordinary magnetoresistance *(EMR)*.

Giant magnetoresistance, one of the *MR* varieties, is a seminal value within a few percent the *MR* value exceeds the anisotropic magnetoresistance considerably (122). The meaning of giant magnetoresistance is a quantum mechanical phenomenon seen in multi-layered thin-film heterostructures. These heterostructures formed with alternating *FM* and *NM*-metallic phases. (122). The way of the magnetization process in the *FM* layer can enormously affect the resistivity of the system (123). For instance, the resistivity decreases comparatively with the parallel arrangement and comparatively increases with the anti-parallel arrangement. Thus, one can examine the direction of magnetization by the implementation of the magnetic field. Moreover, the *GMR* impact forms by electron scattering on the spin orientation.

Secondly, colossal magnetoresistance is a huge *MR* in manganites oxides which is greater than the *GMR* effect. Many theories which have been purposed to explain the *CMR* mechanism, have suggested the key role played by the Mn^{3+}/Mn^{4+} mixed valance state in the *CMR* phenomenon (124). It occurs around T_C and arises from the spin disorder suppression under the effect of high magnetic field values, which retard their technological implementation.

Another type of *MR*, tunneling magnetoresistance becomes in a magnetic tunnel junction *(MTJ)*. It is a constituent including two ferromagnets is disparted by a thin insulator. In general, *MTJ* is originated by a thin insulator layer enough *(~ nm)* between two ferromagnetic layers (125). *TMR* effect is based on spin-dependent tunneling. For example, only up-spin electrons can only tunnel into up-spin states, and down-spin electrons can tunnel to down-spin states (126). Hence, there are two possible configurations: antiparallel and parallel. The carriers can only tunnel from one side to the other in the parallel configuration. Thus, the considered resistances are various for parallel and antiparallel magnetization arrangement of the electrodes. This is the foundation of tunneling magnetoresistance *(TMR).* The equation of *TMR* is:

$$TMR = \frac{\Delta R}{R} = \frac{R_{AP}}{R_P} \tag{3}$$

R_P and R_{AP} denote the resistance when the magnetization of the two *FM* electrodes are parallel and antiparallel. In addition; manganites are used as a source of the ferromagnetic layer in magnetic *TJ* (127) (128) (129).

As for anisotropic magnetoresistance *(AMR)*, is the main tendency in which the electrical resistivity is correlated with the corresponding angle between the magnetization direction and the electric current direction (130) (131). In other words, it occurs in ferromagnets in which the resistivity is connected to the angle between the current and magnetization direction. The *AMR* impact depends on the simultaneous motion of magnetization and spin-orbit interaction. Thus, the resistance of a region with *M* parallel to the applied current *I* is different from the resistance of a region with *M* perpendicular to *I*. The *AMR* effect has been researched comprehensively both experimentally (132) (133) (134) and theoretically (135) (136). In many materials, especially magnetic transition metals, the *AMR* ratio is often defined by (137):

$$\frac{\Delta\rho(\theta)}{\rho} = \frac{\rho(\theta)-\rho_{\perp}}{\rho_{\perp}} \tag{4}$$

with $\rho_{\perp} = \rho(\pi/2)$, where $\rho(\theta)$ is the resistivity for θ.

Extraordinary magnetoresistance *(EMR)* is defined as the altering in electrical resistance upon the implementation of an enormous magnetic field that can be greater than *1,000,000%* at room temperature. Its magnitude is greater than other magnetoresistance impression such as *GMR* and *CMR* (138). It generates in hybrid structures which consist of semiconductors and metal. The current flows through the metal with no magnetic field (at low resistance). But, the current is strained to run through the semiconductor with the large magnetic field and, the system has much higher electrical resistance because of the Hall angle approaching *90°* (139). Thus, the system geometry is affected greatly. The *EMR* effect has many possible benefits for applications of different geometries of *EMR* devices (140).

2.6 Conduction Mechanisms

A major behavior has been examined in $Ln_{1-x}A_xMnO_3$ (where *Ln* is lanthanide and *A* is a divalent cation) by doping of divalent cations such as Ba^{+2},

Sr^{+2}, or Ca^{+2}, etc. at the *Ln* site. The $LnMnO_3$ compound which is an insulator has been investigated on the creation of Mn^{+4} state with the interaction Mn^{+4} and Mn^{+3} owing to the hoping of the electron from one part to another correlate with electronic transport in them. Two kinds of transition are displayed by the doped manganites. The first one is the electrical transition from insulating/semiconducting state to metallic state. The transition occurs at peak temperature T_{MI}. The second one is the magnetic transition from paramagnetic state to ferromagnetic state, and it actualizes at Curie temperature T_C. The transport and magneto-transport properties depend on doping, grain morphology, average ionic radius, heat treatment, size variance, etc. To research the resistivity in the semiconducting or insulating and metallic regions, there are significant models for high temperature and low-temperature regions.

Electrical transport is probably the most remarkable physical feature of the manganites. Hopping conduction explained that is electrical conduction where the carriers transported with electrons hopping from one localized state to another. Electron transport through a localized state within the bandgap of a semiconductor is shown in Fig. 2.7.

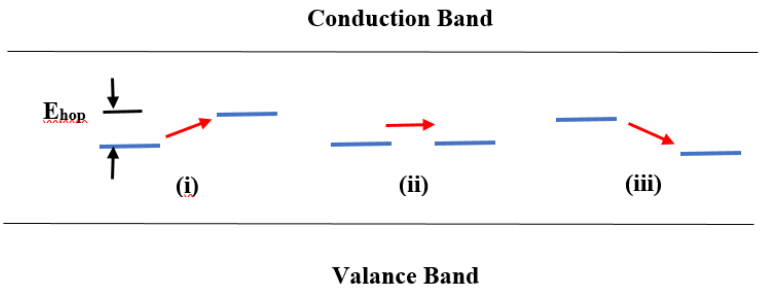

Figure 2.7. Electron transport between localized states (i) thermally supported tunneling (ii) tunneling which is independent temperature (iii**)** tunneling with the emission of a phonon and independent of temperature.

According to Fig. 2.7, in the first case (i), electron scatters from lower energy state to higher energy state. That hopping which is thermally supported tunneling and depends on temperature requires thermal energy. E_{hop} is the energy difference in this movement. In the second case (ii), the electron jumps between equivalent energy states. This type of movement is a tunneling process, is independent of temperature. In the third case (iii), the electron jumps from a

higher energy state to a lower energy state. This type of process is a tunneling transport with the emission of phonons and is independent of temperature.

Additionally, there are essential conditions to occur hopping. At first, there should be an overlapping of the wave function of the two localized states. The other one is that empty and occupied states must be present for the occurrence of hopping. This condition requires hopping which should take part between states close to the Fermi level. And, the last one is that energy is needed to jump from a localized state to another localized state with a higher energy level.

2.6.1 High-Temperature Region

In the high-temperature part at $T>T_{MI}$, *LSMO* is a semiconducting insulator. In this regime, there are four significant models to support experimental data. i) thermally activated hopping model *(TAH)* (141) ii) the nearest neighbors hopping model *(NNH)* (142) and iii) a variable range hopping *(VRH)* model (143) iv) small polaron hopping model *(SPH)* (144).

2.6.1.1 Thermally Activated Carriers Model

According to the considered model, the electrons are excited thermally across the band gap from the valance band to the conduction band. In this model, the resistivity is explained by the equation below;

$$\rho = \rho_0 \exp(\frac{E}{k_B t}) \tag{5}$$

where E is the activation energy, ρ_0 is the residual resistivity and k_B is the Boltzman constant *($k_B = 8.617x10^{-5}\ eV.K^{-1}$)*

This elementary model is connected with the resistivity given by the equation below;

$$\rho = (n\ e\ \mu)^{-1} \tag{6}$$

where n is the carrier density on the conduction band, e is the charge of the electron and μ is the carrier mobility. The dominating coefficient is generally the thermally activated form of n, and μ is accepted to be independent of temperature. If the charge-ordered phase and conduction mechanism in the insulating

paramagnetic result from the thermally activated carriers, the activation energy should be particular for each phases. Then, a transition from the paramagnetic to charge-ordered states emerges with an instantaneous change of gradient in the logarithm of resistance versus temperature.

2.6.1.2 Nearest Neighbour Hopping Model

It is recognized that e_g electrons are correlated with lattice distortions (i.e. they create polarons) in the paramagnetic state. Electrical conduction goes on by polaron movement. The size of the lattice distortions for the considered model is alike to unit cell size. Also, the polarons travel between the nearest neighbor part. The resistivity is written as below;

$$\rho = ATexp(\frac{E}{k_B T}) \tag{7}$$

where E is the required energy to move a polaron and A is a constant. But, the intense electron-polaron coupling is explained that the movement of the charge carriers is slow as regards the lattice vibration. The movement of the lattice and the electrons cannot be distinguished. Moreover, research in a non-adiabatic limit is so complex (145). The resistivity is written as below;

$$\rho = AT^{3/2}\exp(-\frac{E}{k_B T}) \tag{8}$$

2.6.1.3 Variable Range Hopping *(VRH)* Model

When the temperature is enough low, the possibility of the electron thermal activation between states which are close in space but far in energy gets smaller than that of electron jumping between some more far states whose energy levels happen to be too close to each other (146). The characteristic hopping distance d_{vr} increases with declining temperature for the considered case. Hence, that kind of hopping is called the variable range hopping *(VRH)* model.

The average distance between the nearest neighbor hopping d_{nn} and variable range hopping d_{vr} are seen below Fig. 2.8.

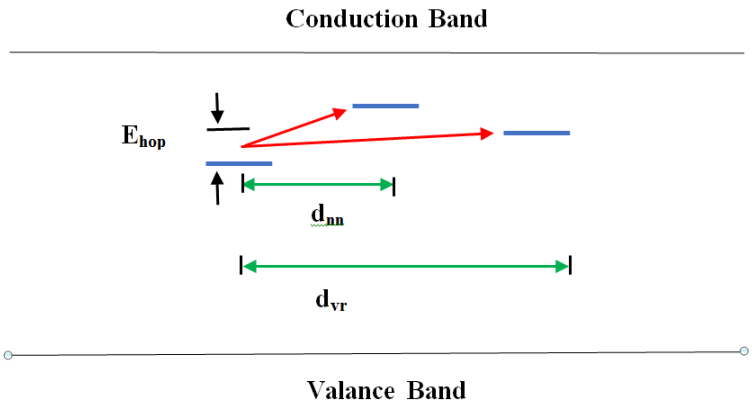

Figure 2.8. The distance of nearest neighbor hopping and variable range hopping.

The resistivity is written in semiconducting or insulating regions by using variable range hopping *(VRH)* model for uncorrelated carriers as below (91) (143) (147);

$$\rho = \rho_0 \exp\left(\frac{T_0}{T}\right)^{\frac{1}{(1+d)}} \tag{9}$$

where *d* is the dimensionality and for 3D systems *(d=3)*(*3D-VRH* model), thus it can be written as;

$$\rho = \rho_0 \exp\left(\frac{T_0}{T}\right)^{\frac{1}{4}} \tag{10}$$

where T_0 is the Mott characteristic temperature and is related to the carrier localization length by the expression (148);

$$T^0 = \frac{18}{k_B N(E_F) a^3} \tag{11}$$

k_B is the Boltzmann's constant, *a* is the localization length and $N(E_F)$ is the density of states at the Fermi level. The value of the localization length should be comparable to *Mn-O* distances for the *VRH* model (143).

Furthermore, for the two-dimensional conductance *(2D-VRH), d=2,* and the equation is given by (149);

$$\rho = \rho_0 \exp\left(\frac{T_0}{T}\right)^{\frac{1}{3}} \tag{12}$$

The *VRH* model is extensively fitted with the resistivity data for the range of $T_{MI}<T<\theta_D/2$. According to this model at this temperature range, carriers jump

from site to site with hopping energy E_h, passing a distance R_h, which are temperature-dependent parameters and can be calculated by the $E_h(T) = \frac{1}{4} k_B T^{3/4} T_0^{1/4}$ and $R_h(T) = \frac{3}{8} L(\frac{T_0}{T})^{1/4}$ equations (150).

In doped manganites, the randomness in spins and fluctuations in Coulombic potential is originated due to rising in the size disorder with doping *x* level. Therefore, beyond the *Mn-O* distances, the carriers have some potential differences to jump at farther distances and so conduct through the variable range hopping.

2.6.1.4 Small Polaron Hopping *(SPH)* Model

The small polaron hopping model shows up to be most suitable for manganites with rare-earth ions of smaller ionic radii as the small polarons are originated due to the structural distortions due to the lower ionic radii. The existence of small polarons has a major mission in especial transport features of manganites (151).

This model is very relevant at the $T>\theta_D/2$ temperature range where θ_D is the Debye temperature and $\theta_D/2$ is the linearity deviation temperature with this model.

The resistivity is written for adiabatic small polaron hopping *(ASPH)* conduction as below (149);

$$\rho = \rho_a T \exp(\frac{E_a}{k_B T}) \tag{13}$$

Also, the value of E_a was calculated by multiplying the Boltzmann constant with the experimental data of coefficient *A* which is obtained from the fitting data as seen below;

$$A = \frac{E_a}{k_B} \tag{14}$$

Moreover, the resistivity is written for non-adiabatic small polaron hopping *(NASPH)* conduction as below (149);

$$\rho = \rho_a T^{3/2} \exp(\frac{E_a}{k_B T}) \tag{15}$$

where is ρ_a is the residual resistivity, k_B is Boltzmann constant, E_a the *ASPH* activation energy for hopping conduction, and *T* is the absolute temperature (144) (152).

2.6.2 Low-Temperature Region

In the metallic region that is $T<T_{MI}$, the source of resistivity and electron conduction mechanism have been explained by fitting the resistivity data to an overall polynomial equation as below;

$$\rho = \rho_0 - \rho_{0.5}T^{0.5} + \rho_2 T^2 + \rho_{4.5}T^{4.5} + \rho_5 T^5 + \ldots + \rho_n T^n \qquad (16)$$

where the term ρ_0 represents resistivity due to grain/domain boundary effects (153) (154) (155). The second term $\rho_{0.5}T^{0.5}$ occupies because of contributions from the correlated electron-electron *(e-e)* interactions scattering from static in-homogeneity in *3D* (156), the third term $\rho_2 T^2$ gives the electron-electron *(e-e)* scattering duration in ferromagnetic-metallic *(FM)* state (155), the fourth term is represented to the electron-magnon *(e-m)* scattering process in the ferromagnetic phase (155) and the last term $\rho_5 T^5$ indicates electron-phonon *(e-p)* interaction (155). Moreover, *n* is a higher-order term and may take values *n=2.5, 3, 4.5,* and *7.5* so, ρ_n is the corresponding resistivity coefficient (157) (158) (159) (93) (160). For instance, the value of *n* has been estimated to be *5* for electron-phonon scattering as it is *4.5* for electron-magnon scattering (161). In this equation, ρ_0 is residual resistivity at *T=0* and ρ_2 is the resistivity created by an electron-electron scattering and ρ_n is the electron-magnon or electron-phonon scattering coefficient (142).

In this thesis, to understand the electrical conduction mechanism for below T_{MI} $(T<T_{MI})$ (both the presence and absence of magnetic field), the electrical resistivity data are usually fitted using the following equations:

- Residual weak electron-electron scattering equation:

$$\rho = \rho_0 - \rho_{0.5}T^{0.5} + \rho_2 T^2 \qquad (17)$$

- Residual weak electron-electron and electron-phonon scattering equation:

$$\rho = \rho_0 - \rho_{0.5}T^{0.5} + \rho_2 T^2 + \rho_5 T^5 \qquad (18)$$

3. MATERIALS AND METHODS

3.1 Preparation of the Samples

In this thesis, the first series of manganites of the form $La_{0.8}Sr_{0.2}Mn_{1-x}B_xO_{3\pm\delta}$ were prepared by the conventional solid state reaction method. The immensely purified powders *(>99.9 %*, from the Alfa Aesar) of La_2O_3, $SrCO_3$, MnO_2, and B_xO: *CoO, CuO,* Fe_2O_3, and TiO_2 *(x=0.0 and 0.1)* were weighted in stoichiometric proportion with a precision microbalance (Pic. 3.1).

Picture 3.1. XR 205SM-DR Precisa balance.

Table 3.1. The molecular weight of the powders used in this work.

COMPOUNDS	ATOMIC WEIGHT
La_2O_3	325.82
$SrCO_3$	147.63
MnO_2	86.94
CoO	74.93
CuO	79.54
Fe_2O_3	159.69
TiO_2	79.90

The powders were mixed and ground by hand for *30* minutes one by one in an agate mortar. The heating process included four main steps. In the first step, the mixed powders were calcinated at *800 ℃* for *10 h*. In the second step, after mixing for *15* minutes, the calcinated powders were annealed at *900 ℃* for *20 h*. They were pressed at *3000* psi at room temperature for *5* minutes with a manual hydraulic press (Pic. 3.2) to form a pellet.

Picture 3.2. TSEK TÜMAS manual hydraulic press.

Then, the bulks were annealed at *1150 ℃* for *24 h* for the third time. In the last step, to obtain better crystallization, the bulks were crushed and ground till we got ultrafine powder. The powders were consolidated into pellets of approximate dimensions *40 mm x 8 mm x 1.6 mm* and sintered at *1250 ℃* for *24 h*. Each heating rate is *5 K* per minute and each cooling rate is *3 K* per minute. The calcination and sintering processes of the bulks were conducted using the programmable furnace (PROTHERM-Model PTF12/75/200) (Pic. 3.3). However, another furnace (PROTHERM-Model PLF 150/5) was used for the last sintering process to reach *1250 ℃*.

Picture 3.3. PROTHERM (Model PTF 12/75/200) programmable furnace.

The sample synthesis procedure was schematically depicted as shown below:

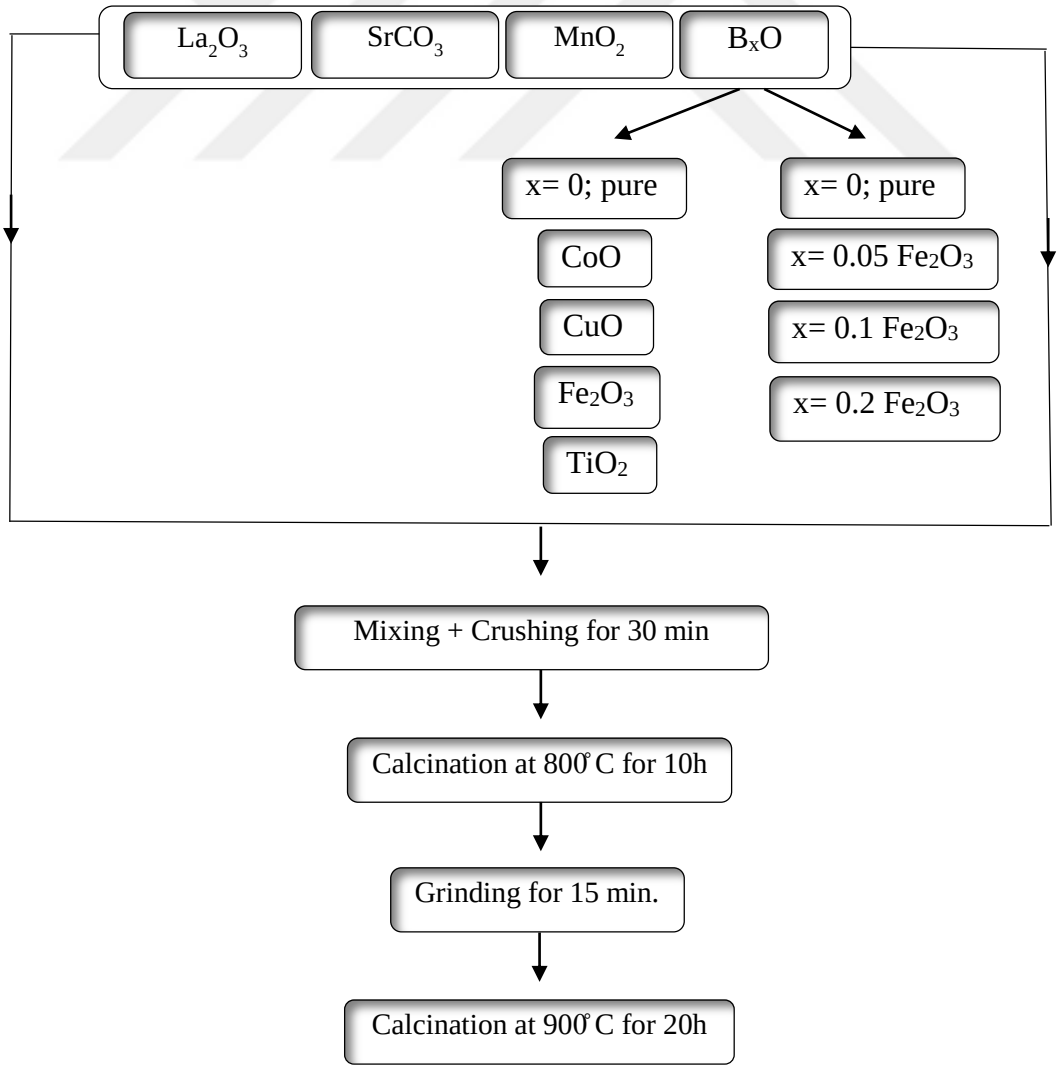

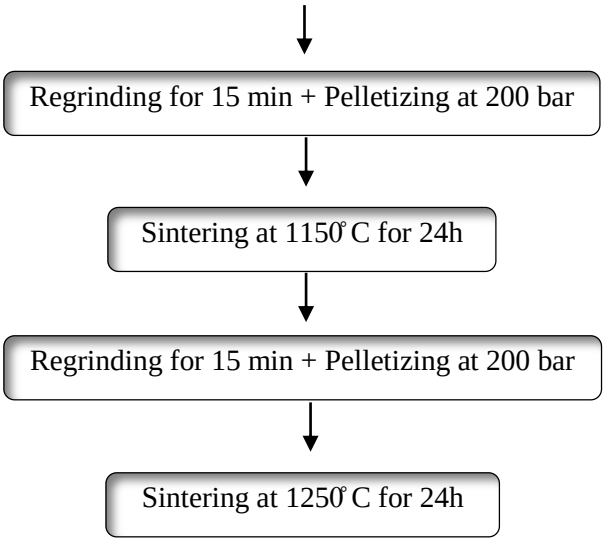

Figure 3.1. The sample synthesis procedure by the solid-state reaction method.

The second series of manganites of the form $La_{0.8}Sr_{0.2}Mn_{1-x}Fe_xO_3$ were prepared with different moles of *x=0.0, 0.05, 0.1*, and *0.2* by conventional solid-state reaction method. Thus, the ideal sample preparation procedure, which obtained in the first serie, applied for the second series preparation. The fourth chapter of the thesis we present the impression of iron substitution on the structural, electrical and magnetic properties of the manganite perovskite system.

3.2 Structural Analysis

Powder X-Ray diffraction analysis, scanning electron microscopy *(SEM)* images, electron dispersive *X*-Ray *(EDX)* measurements, resistivity and magnetoresistance measurements were carried out the examine the structural characterization of the samples.

3.2.1 X-Ray Diffractometer *(XRD)* Measurements

Measurements of *X*-Ray diffractometer are one of the most important results to examine the structure of sample from the scattering pattern. X-ray diffraction method is utilised for phase identification and lattice parameter determination. The working mechanism depends on the interaction between high-energy beams of radiation or charged particles and a material. While an electromagnetic wave goes into a crystal, it is scattered by the electrons inside. A constructive interference occurs between the various scatters for significant angles of incident

beam, however destructive interference eliminates the diffracted beam. By determining at which angles the constructive interference actualized it can obtained the geometrical ordering of the atoms inside the crystal (162) (163). *X*-Ray diffraction method is related to the principle of Bragg's law of diffraction as below:

$$2dsin\theta = n\lambda \tag{19}$$

where d is the space between the crystalline lattice planes, θ is the angle between the incident *X*-ray beam and crystalline plane, λ is the wavelength of the incident X-ray beam and n is the order of diffraction.

In this work, the phase identifications of the samples were investigated by *XRD* by using Rigaku MultiFlex *2kW* diffractometer (Pic. 3.4) with *CuKα* radiation *(λ=1.5418 Å)* in the range of *20–80°* at a scan speed of *3°/min* and a step increment of *0.02°* at room temperature. Phase purity and lattice parameters were obtained from the *XRD* diffraction. The Jana refinement analysis was applied to compare the experimental *XRD* results of the samples with the aid of *JANA* program to calculate the lattice parameters.

Picture 3.4. Rigaku MultiFlex 2kW X-Ray Diffractometer.

Picture 3.5. A picture from Rigaku X-ray diffractometer system during the powder X-ray diffraction.

3.2.2 Scanning Electron Microscopy *(SEM)* Measurements

A scanning electron microscope takes photographs of samples by scanning the surface by an electron beam. While the incident electron beam interacts the atoms of the sample, a data signal about the composition and surface topography are derived. In this work, crystallinity, grain size, and grain connectivity of the samples were examined by Scanning Electron Microscopy *(SEM)* JEOL 6390-LV (Pic. 3.6), operated at an acceleration voltage of 20 kV.

Picture 3.6. JEOL JSM-6390LV Scanning Electron Microscope.

3.2.3 Electron Dispersive X-Ray *(EDX)* Measurements

Energy dispersive X-Ray *(EDX)* analysis is a major method to investigate the elemental examination or chemical identification of a material. As it is well known that if an atom is at ground state (or unexcited), the discrete energy levels are at rest. The incident electron beam (high-energy beam of charged particles) can evoke an electron in an inner shell of the atom and the electron is ejected from the shell. Thus, a hole forms in the inner shell. Then, an electron from an outer (higher-energy) shell fills the hole occurred. Hence, the energy gap due to the outer and the inner shell is emitted in the form of a photon. Energy dispersive spectrometer qualifies the number and energy of the photon released from the material and the elemental composition of the material is analysed. In this thesis, the elemental distributions and compositions in the samples were examined with the Oxford *X*-ray micro-probe analysis connected to *SEM (EDX)*. IXRF SYSTEMS Model 550i Analyzer (Pic 3.7) was used to explore the photons emitted from the samples.

Picture 3.7. IXRF Systems Model 550i Analyzer.

3.2.4 Magnetic and Electrical Measurements

The electrical features of the considered samples were researched by dc resistance versus temperature measurements using 5 mA dc current in the temperature range from 20 to 320 K in the Helium gas contact cryocooler from CRYO Industries (Pic. 3.8). This system utilizes helium gas as the refrigerant and is assembled to interface with many kinds of apparatus that require cryogenic temperatures. Moreover, the magnet is a close-cycle cryocooled Nb_3Sn

superconducting magnet. The temperature was adjusted by using a cryogenic temperature controller from Cryogenic Control Systems (Model 32B), which has a stability of 3 mK at 320 K. The pressure inside the cryocooler was calibrated by using Varian Vacuum Pumping System Model 969-8227.

Electrical resistance measurements give us many practical data about the electrical features of the sample. The experimental results of electrical resistance versus temperature provide information about the different temperature-dependent electronic phase transitions. Furthermore, it ensures us both an uncomplicatedly achievable and certain value of the transition temperature and opinion of the quality of the sample.

Picture 3.8. Cryostat system for the resistivity measurements.

A Keithley 2400 source meter and a Keithley 2700 multimeter (Pic. 3.9) were used for the standard four-probe measurements, which allow us to find the true specimen resistance without consisting of the contact resistance between the probes and the specimen (164) (165).

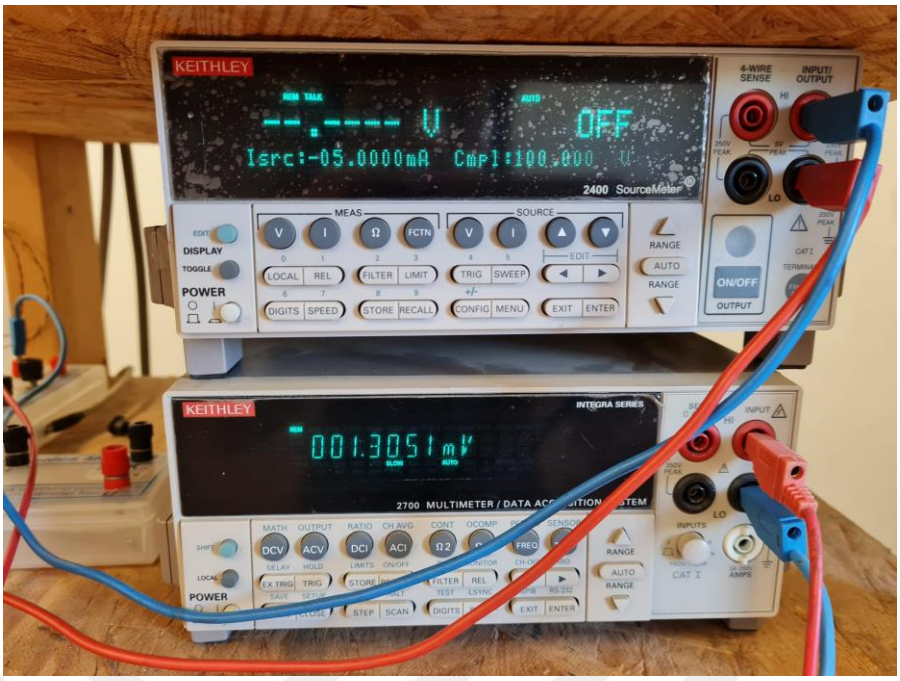

Picture 3.9. Keithley 2400 source meter and Keithley 2700 multimeter.

Low contact resistance is preferred because of the small resistance of the samples. Therefore; the standard four-probe method was chosen to evaluate the value of resistance. In order to use this method, the samples were cut in a rectangular bar shape by a fret-saw. The silver paste was spread at the ends of the sample for current and midpoints for voltage contacts. Thin copper wires that have little resistance were connected with silver paint (Pic. 3.10) As shown in same picture, the current was passed through the outer probes *(I_+ & I_-)* and the resultant potential difference occurred between the two points was measured by using the inner probes *(V_+ & V_-).* The value of the resistance can be obtained with Ohm's Law as below;

$$V=I.R \tag{20}$$

where V is the voltage and I is the current passed.

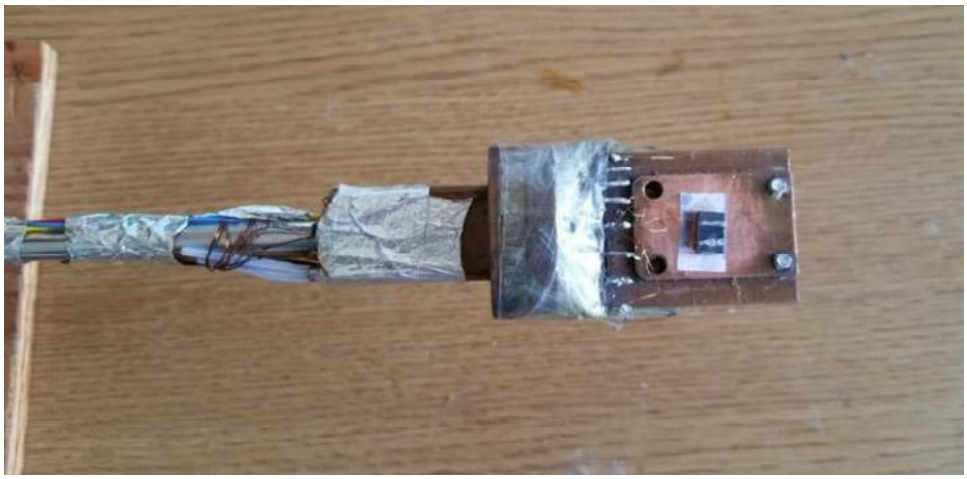

Picture 3.10. Experimental set-up for the 4-point probe measurement.

The net resistivity *(ρ)* of the sample is calculated by using dimension of the sample. With the aid of the current and voltage measured, the resistivity of the samples computed by the following equation;

$$\rho = \frac{R.A}{l} \tag{21}$$

where ρ denotes the resistivity of a material, R is the resistance, $A = w \times t$ is the cross-sectional area of the sample (w: width, t: thickness) and l is the shortest distance between the voltage probes. The samples were cooled down to 20 K by using Helium gas. Then, the temperature was increased by controlling a heater. While the temperature was going up slightly, resistance was measured at every value of the temperature. Hence, resistance versus temperature graphs were obtained. Moreover, these measurements were repeated at *1* Tesla for each samples.

Picture 3.11. Superconducting Coil Magnet System.

4. RESULT AND DISCUSSIONS

The *LSMO* system serves an important platform to investigate several physical features. Thus, its unique features have been investigated considerably, recently (1) (17) (20) (21). However, the substitution at *B*-site in manganites are relatively less explored. This section deals with the results of transition metals doped $La_{0.8}Sr_{0.2}Mn_{0.1}O_3$ *(LSMO)* manganite systems which are prepared by using conventional solid-state reaction method. To analyze the structural, magnetic, and electrical-transport features of *B*-site substituted manganese perovskites, we replaced *10 %* of *Mn* ions with different transition metals as ***Cu, Co, Fe*** and ***Ti***.

4.1 Transition Metal Effects in *LSMO* System

In this part of the thesis, we have analysed the comparative investigation of 10% transition metal (*TM*) substituting of the *Mn*-site in $La_{0.8}Sr_{0.2}Mn_{0.1}O_3$ *(LSMO)* system, i.e. $La_{0.8}Sr_{0.2}Mn_{0.9}Cu_{0.1}O_3$, $La_{0.8}Sr_{0.2}Mn_{0.9}Co_{0.1}O_3$, $La_{0.8}Sr_{0.2}Mn_{0.9}Fe_{0.1}O_3$, $La_{0.8}Sr_{0.2}Mn_{0.9}Ti_{0.1}O_3$. Hereafter, the samples are coded referred as ***S 0, Cu, Co, Fe***, and ***Ti,*** respectively.

4.1.1 X-Ray Diffraction *(XRD)* Refinement Analyses

At first, the powder X-ray diffraction measurements with CuK_α radiation at room temperature are performed after each sintering process to obtain the ideal phase of the considered compounds. As seen in Fig. 4.1, the unreacted peaks such as manganese (III) oxide (Mn_3O_4), which is indicated by the (⁂) symbols, is detected at *900 ºC* for all samples. It is observed that these unreacted peaks disappear as the temperature increases. And, it is verified by *XRD* results that there is single-phase formation of all samples. Moreover, the intensity of diffraction peaks for the *LSMO* perovskite phase increases when the sintering temperature increases from *900 ºC* to *1250 ºC*. It denotes that crystallinity of *LSMO* gets better (166). It is seen that the final temperature is decided at *1250 ºC* because of having an excellent perovskite structure and no unreacted peaks.

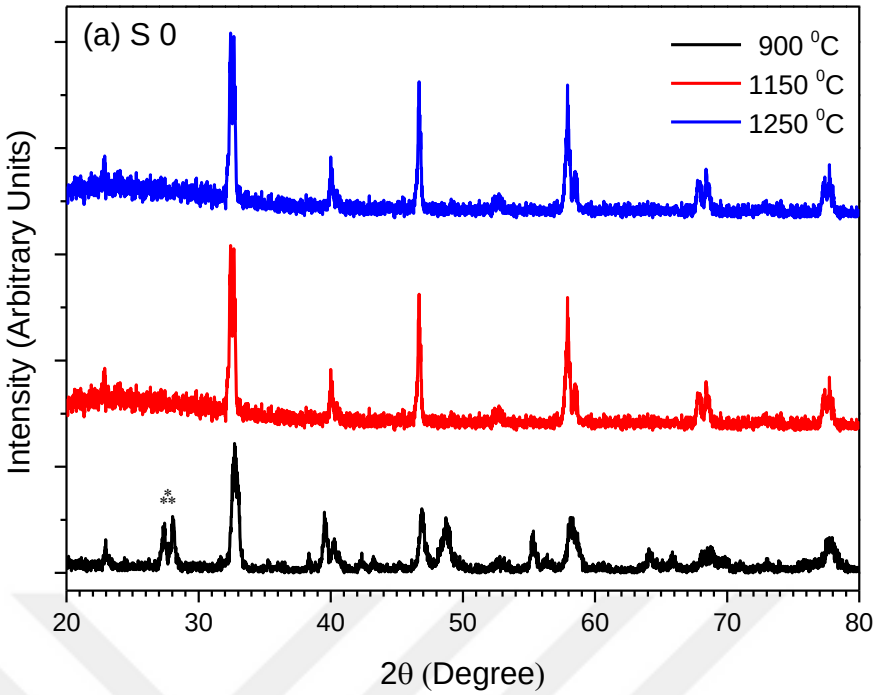
(a) S 0
900 °C
1150 °C
1250 °C
Intensity (Arbitrary Units)
20
30
40
50
60
70
80
2θ (Degree)

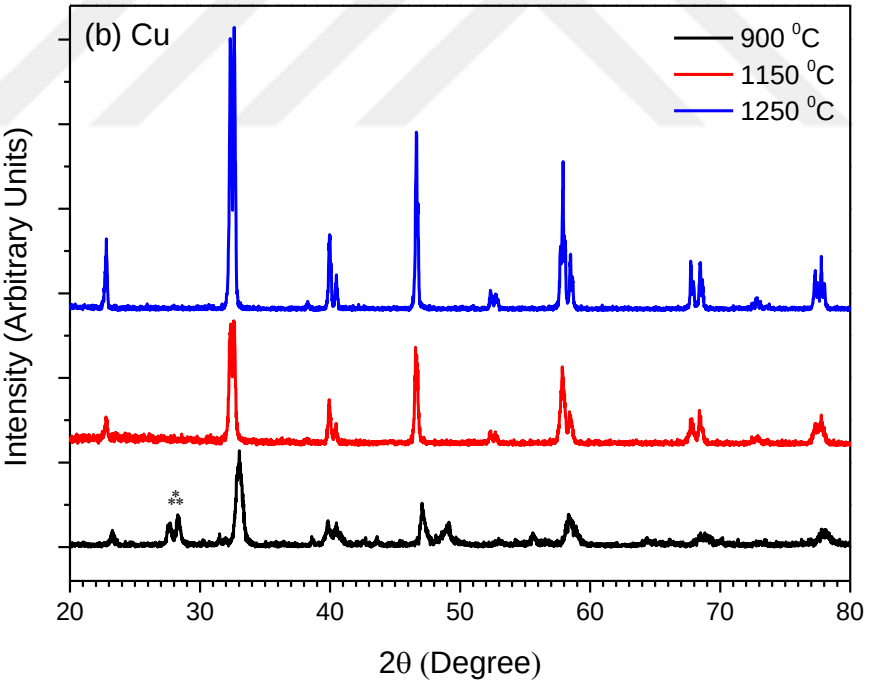
(b) Cu
900 °C
1150 °C
1250 °C
Intensity (Arbitrary Units)
20
30
40
50
60
70
80
2θ (Degree)

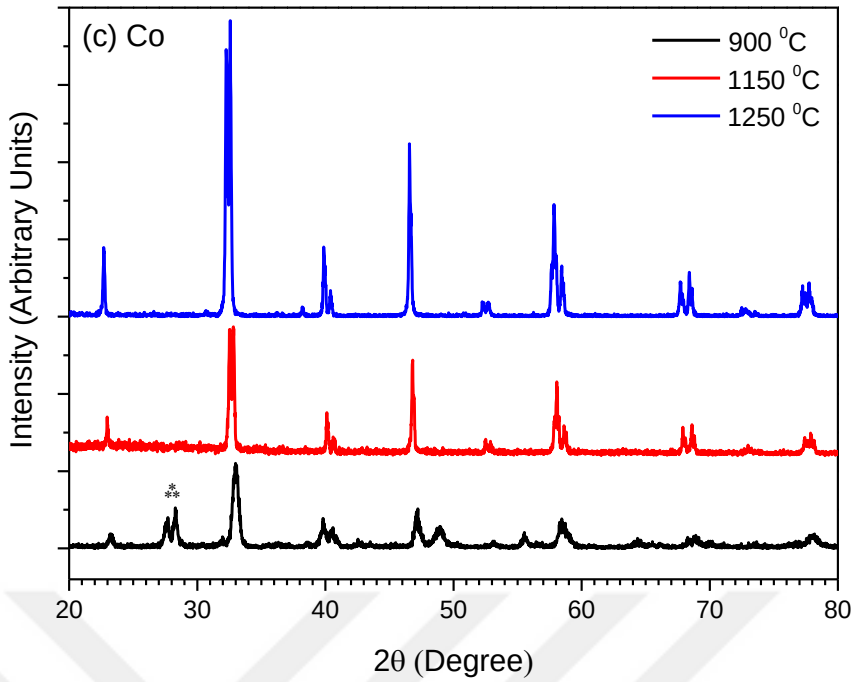
(c) Co
900 °C
1150 °C
1250 °C
Intensity (Arbitrary Units)
20
30
40
50
60
70
80
2θ (Degree)

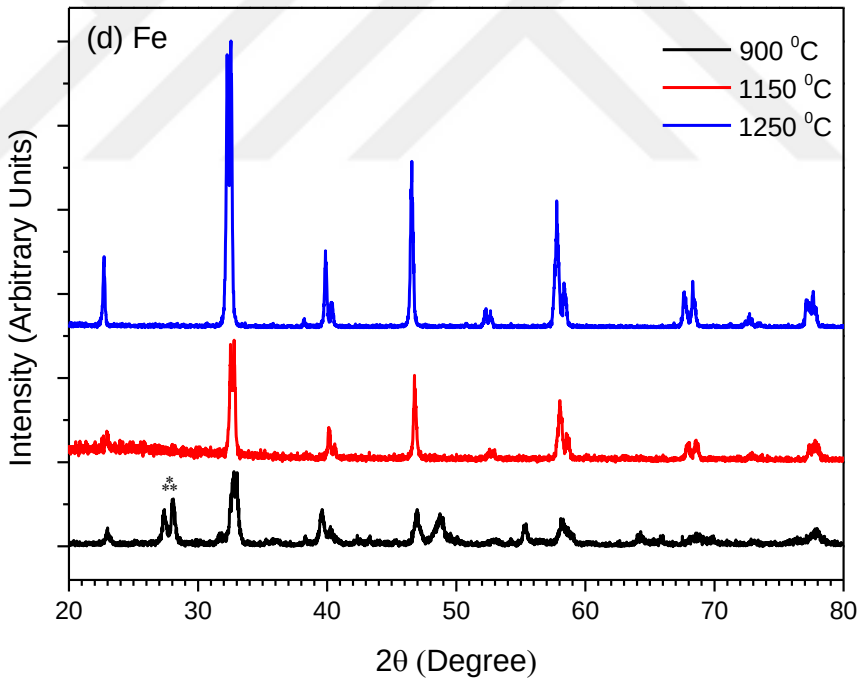
(d) Fe
900 °C
1150 °C
1250 °C
Intensity (Arbitrary Units)
20
30
40
50
60
70
80
2θ (Degree)

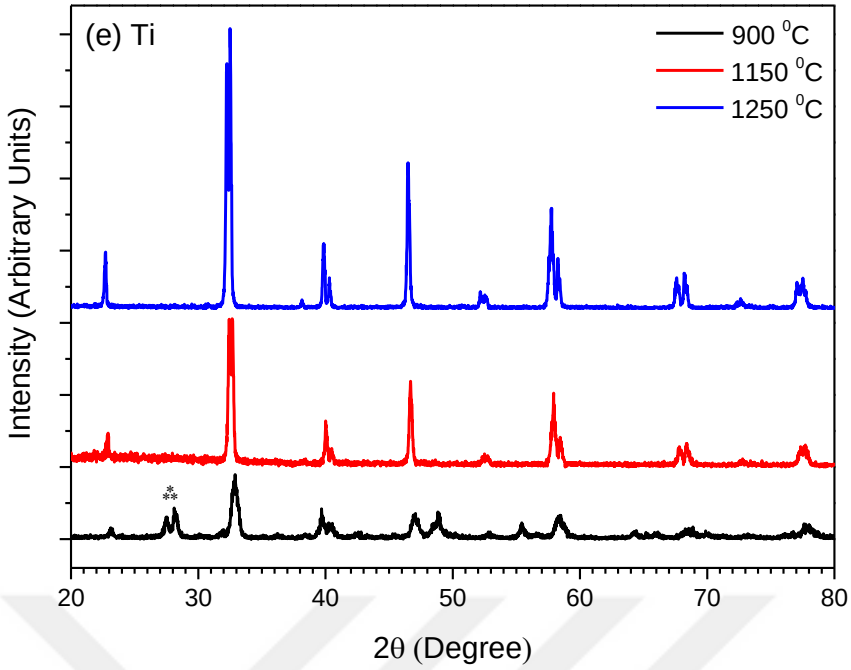

Figure 4.1. X-ray diffraction pattern for $La_{0.8}Sr_{0.2}Mn_{1-x}B_xO_{3\pm\delta}$ compounds with *B:* ***(a) S 0*** *x=0.0,* ***(b) Cu*** *(x=0.1),* ***(c) Co*** *(x=0.1),* ***(d) Fe*** *(x=0.1) and* ***(e) Ti*** *(x=0.1)* after each heating process.

The powder X-ray diffraction analysis was performed to investigate the structural analysis and phase characterization. In order to analogize the influence of substitution of transition metals on *LSMO, XRD* patterns of the pure sample ***(S 0)*** and transition metal substituted sample were plotted one by one in the same graph. Also, the structural parameters obtained from the Jana refinements are tabulated in Table 4.1 It is seen that the lattice parameters slightly increase by substituting ***Cu***, and as expected, the unit cell volume increase. When the main peaks, corresponding to planes of *(2-10)* and *(104),* were enlarged (see inset of Fig. 4.2), it is seen that they are shifted slightly towards to lower angle sides (detailed view of the angle between *32.98°* and *32.64°* is displayed). The angle shift case and increase in lattice parameters could be explained in such a way that ***Cu*** atoms go into the *LSMO* lattice to substitute for *Mn* atoms in *B* sites and they create a new compound of $La_{0.8}Sr_{0.2}Mn_{1-x}Cu_xO_3$ *(LSMCO)* phase (22). Furthermore, the larger ionic radius of Cu^{2+} $(<r_{Cu2+}>)=0.73$ *Å* confront with that of Mn^{3+} and Mn^{4+} $(<r_{Mn3+}>)=0.645$ *Å,* $(<r_{Mn4+}>)=0.53$ *Å* cause the slight lattice expansion and the increase cell parameters (23).

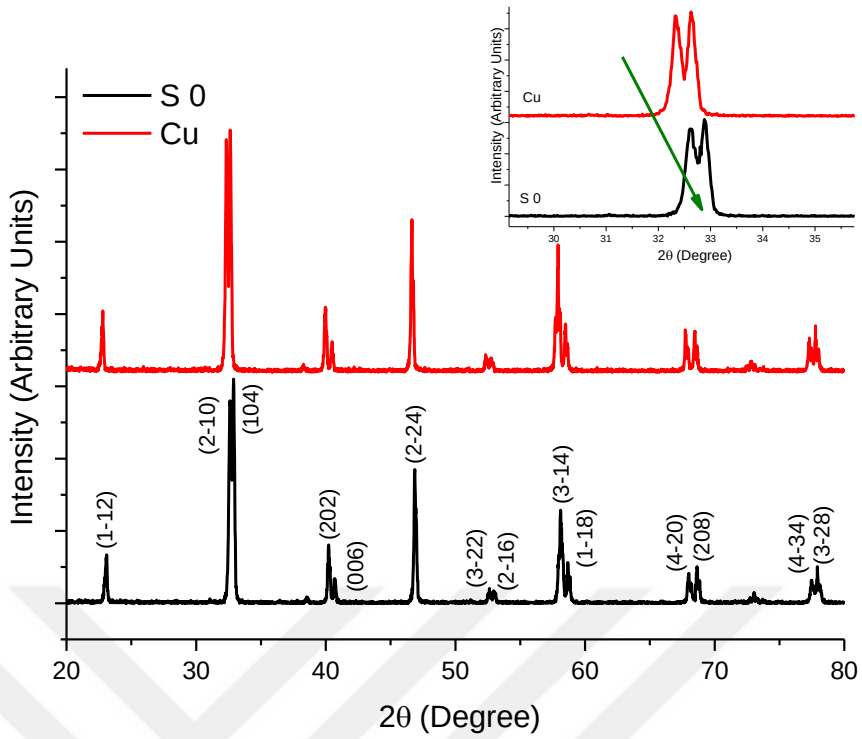

Figure 4.2. X-ray diffraction pattern and layers of $La_{0.8}Sr_{0.2}MnO_3$ and $La_{0.8}Sr_{0.2}Mn_{0.9}Cu_{0.1}O_3$. Inset shows the strongest intensity shift with substitution.

One can check from the inset of Fig. 4.3 that the strongest peak shift to the lower angles, cell parameter and unit cell volume increase which is clearly seen on Table 4.1. The reason of the change in the structural parameters should be explained by considering ionic radius and valence states of the *B*-site cations (31). Similar to manganese ions cobalt also possess different spin and valence states in ABO_3 structure (167). The spin states of Co^{2+}, Co^{3+}, and Co^{4+} ions can be obtained in high-spin state *(HS)* or low-spin state *(LS).* For this reason, any perturbation raising from the valence and spin states of *Mn* and ***Co*** cations significantly change the lattice parameters and unit-cell volume. For instance, the ionic radius of Co^{2+} cation $(<r_{Co2+}>)= 0.65$ *Å* in the *HS* is greater than the Mn^{3+} ion $(<r_{Mn3+}>)=0.64$ *Å* and so, they can be replaced by each other. Or, it is expected that Mn^{4+} ions whose ionic radius is $(<r_{Mn4+}>)=0.53$ *Å,* can be replaced by Co^{3+} ions whose ionic radius is $(<r_{Co3+}>)= 0.61$ *Å* in the low spin state. In accordance with these possibilities, the increase in cell parameters and volume by substituting of ***Co*** is acceptable (31).

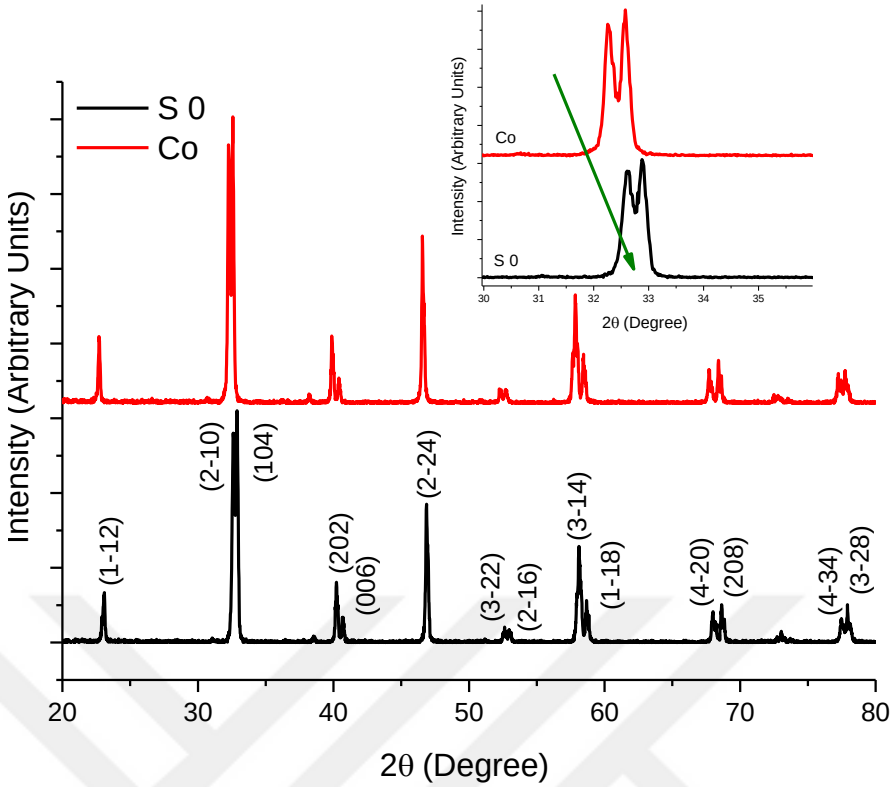

Figure 4.3. X-ray diffraction pattern and layers of $La_{0.8}Sr_{0.2}MnO_3$ and $La_{0.8}Sr_{0.2}Mn_{0.9}Co_{0.1}O_3$. Inset shows the strongest intensity shift with substitution.

Based on the *XRD* study of ***S 0*** and ***Fe*** (Fig. 4.4), it is observed that the peaks shift to the left (lower angle side) after the transition element of ***Fe*** is substituted in ***S 0***. The change in the cell-volume can be also clearly seen from the *XRD* graph by enlarging the shift of the diffraction peaks (insets of Fig. 4.4). The shift in the lower angles at the strongest peak with the ***Fe*** amount is evidence of the increase in the structural parameters (103). *LSMO*, perovskite manganite substituted with ***Fe*** at site-*B*, can be affected by the mismatch of ionic radius between ***Fe*** ions and ***Mn*** ions. After refinement analysis, structural parameters of the considered samples are obtained and they are given in Table 4.1. It is noticed that there is an increase in the lattice constants and unit cell volume with substituting ***Fe***. According to the literature, the charge concentration of ***Fe*** ions can be in the high-spin Fe^{2+}, high-spin Fe^{3+}, and Fe^{4+} states (103). The *B*-site cations for 6 coordination number, the ionic radius of Fe^{4+} *(*$(<r_{Fe4+}>=0.585$ *Å)* is larger than the ionic radius of Mn^{4+} *(*$(<r_{Mn4+}>=0.53$ *Å).* The high spin state ionic radius of Fe^{3+} *(*$(<r_{Fe3+}>=0.645$ *Å)* is the same with Mn^{3+} *(*$(<r_{Fe3+}>=0.645$ *Å)* and larger than Mn^{4+}. Also, Fe^{2+} *(*$(<r_{Fe2+}>=0.78$ *Å)* is larger than both Mn^{3+} and

Mn^{4+} (103). In addition, for the charge neutrality, it is deduced that Fe^{4+} ions substitute Mn^{4+} ions and Fe^{3+} ions substitute Mn^{3+} ions. For our situation, it is estimated that the ionic state of Fe^{4+} is dominant in the perovskite ceramics and the overall iron substitution causes a change in the relative cation fractions of the mixed-valence states of the manganese ions, which leads to an increase in the number of Mn^{4+} cations, as a result, the structural parameters, as well as unit cell volume, is increased.

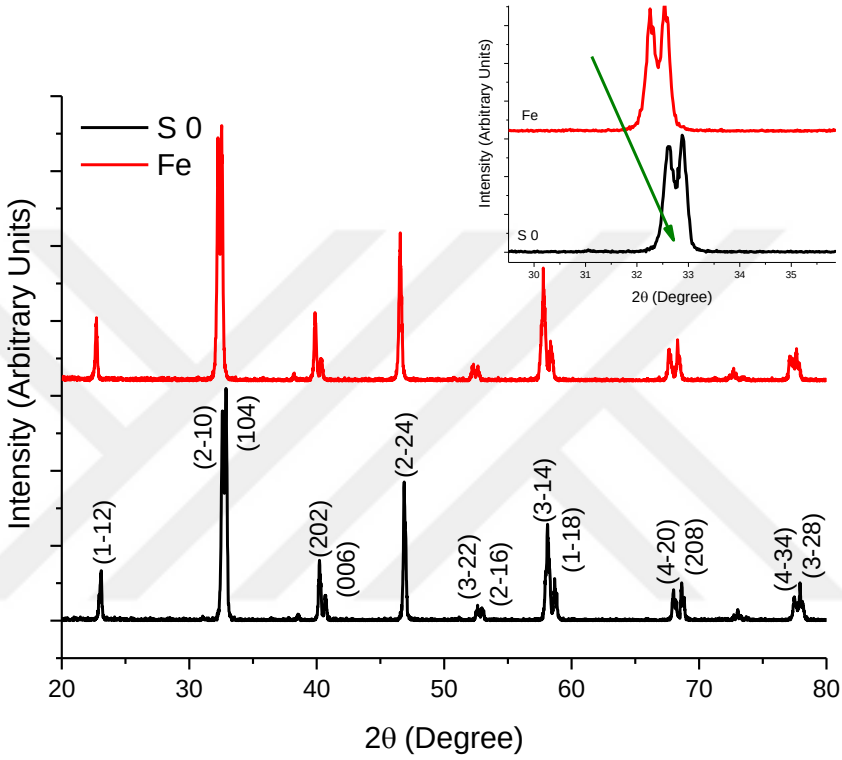

Figure 4.4. X-ray diffraction pattern and layers of $La_{0.8}Sr_{0.2}MnO_3$ and $La_{0.8}Sr_{0.2}Mn_{0.9}Fe_{0.1}O_3$. Inset shows the strongest intensity shift with substitution.

As for *XRD* analysis of ***S 0*** and ***Ti,*** it is clearly seen in Fig. 4.5 that the peak with the strongest intensity is shifted to the lower angles by substitution of *Ti*. The corresponding structural parameters derived by Jana refinement results of the powder *XRD* analysis are listed in Table 4.1. As seen in Table 4.1, there is an increase in lattice parameters with ***Ti*** substituting because of the larger ionic radii of Ti^{4+} *(($<r_{Ti4+}>$)=0.605 Å)* ion as compared to that of Mn^{4+} *(($<r_{Mn4+}>$)=0.53 Å)* ion (103) (168).

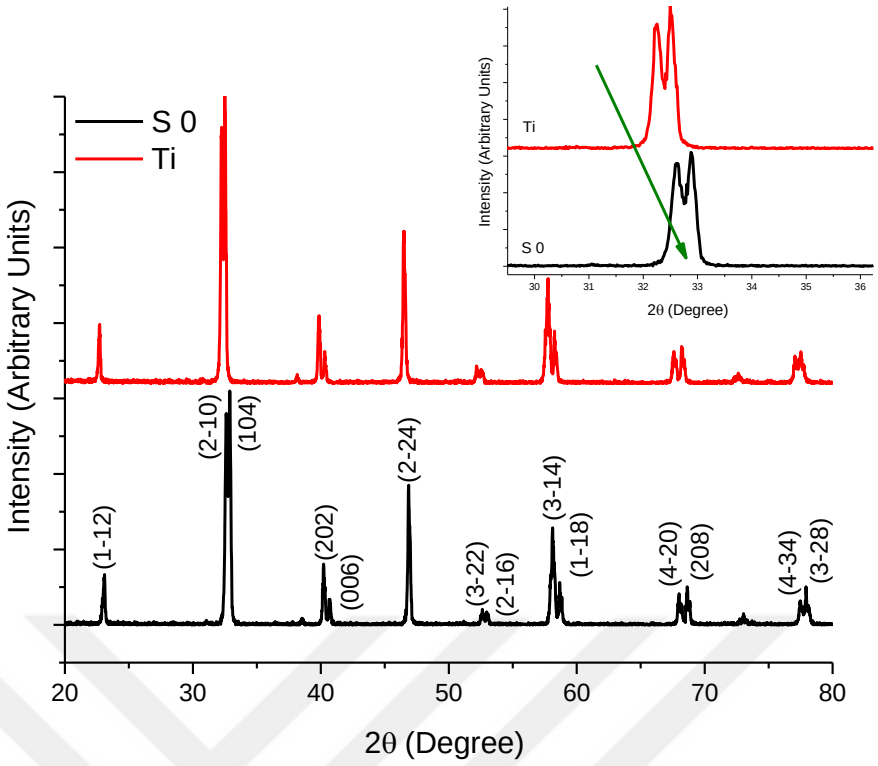

Figure 4.5. X-ray diffraction pattern and layers of $La_{0.8}Sr_{0.2}MnO_3$ and $La_{0.8}Sr_{0.2}Mn_{0.9}Ti_{0.1}O_3$. Inset shows the strongest intensity shift with substitution.

In addition to all binary *XRD* analysis, *XRD* measurements for all samples are plotted in the same graph to observe the rate of shifting according to the reference sample of ***S 0***. As seen in the Fig. 4.6, the degree of shifting increases in the following order of ***Cu, Co, Fe*** and ***Ti.***

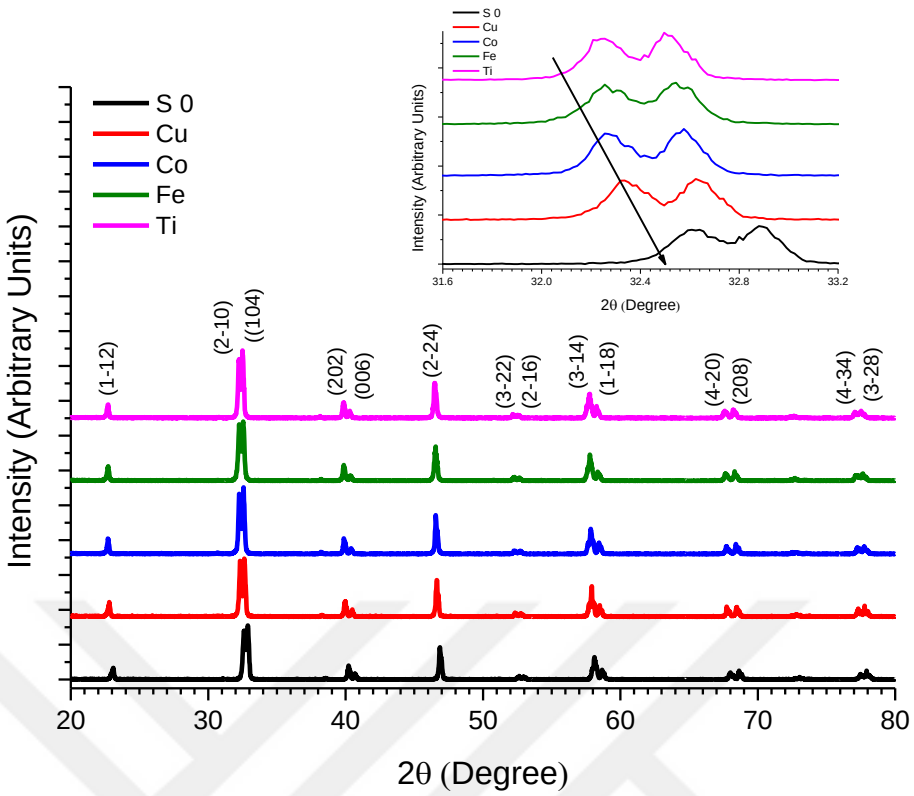

Figure 4.6. X-ray diffraction pattern and layers of $La_{0.8}Sr_{0.2}MnO_3$, $La_{0.8}Sr_{0.2}Mn_{0.9}Cu_{0.1}O_3$, $La_{0.8}Sr_{0.2}Mn_{0.9}Co_{0.1}O_3$, $La_{0.8}Sr_{0.2}Mn_{0.9}Fe_{0.1}O_3$ and $La_{0.8}Sr_{0.2}Mn_{0.9}Ti_{0.1}O_3$ after the last annealing process at *1250 ºC*. Inset shows the strongest intensity shift with substitution.

Moreover, Jana refinement powder *XRD* patterns were done for all samples (Fig. 4.7). The crystal structure of the samples has fitted with the rhombohedral space group *($R\bar{3}c$) (No:167).* According to the data obtained with the Jana refinement (see Table 4.1), the lattice parameters slightly increased in the order of ***S0, Cu, Co, Fe,*** and ***Ti***. Also, the cell volume slightly increases in the same order. There is an important point here that, the experimental *XRD* pattern and the fitted pattern match very well according to fitting quality factors (*Goodness of Fit-GOF*, R_p and R_{wp}*).* Refinement parameters are listed in Table 4.1. The peaks are considerably sharp and have a high intensity. So, this gives us that the considered compounds are clearly crystalline. It is obtained that the ceramic samples have a single phase without impurities in each sample that has been substituted with transition metal which shows that there is no structural transition in the entire sample made with substitution. In other words, no secondary phases corresponding to the unreacted transition metal, any oxide of a transition metal, or manganese dioxide were detected from the *XRD*.

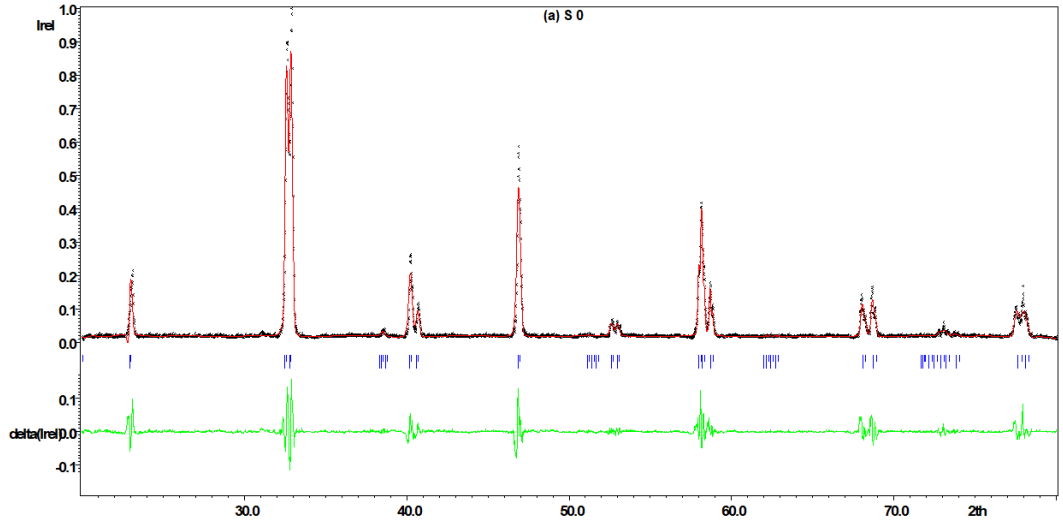
(a) S 0
Irel
1.0
0.9
0.8
0.7
0.6
0.5
0.4
0.3
0.2
0.1
0.0
delta(Irel)
0.1
0.0
-0.1
30.0
40.0
50.0
60.0
70.0
2th

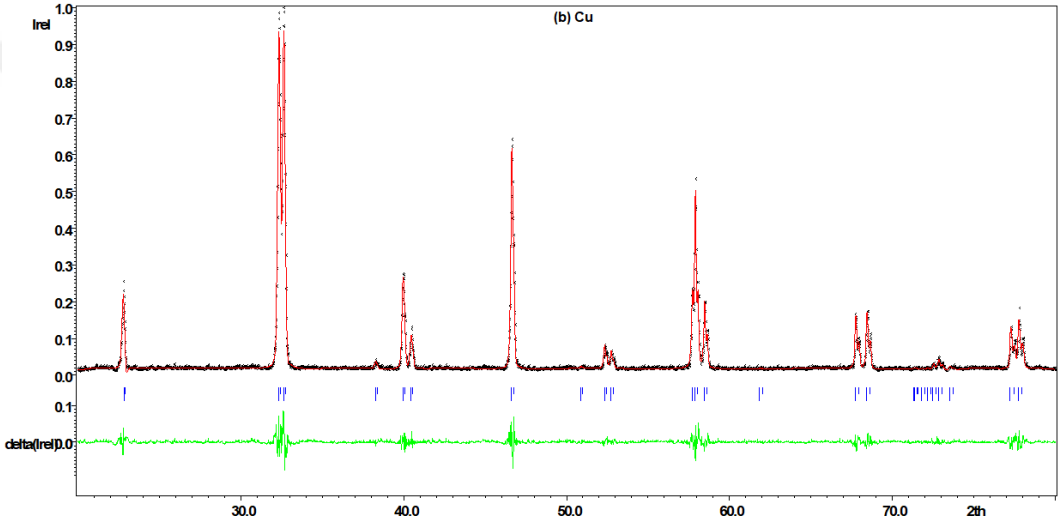
(b) Cu
Irel
1.0
0.9
0.8
0.7
0.6
0.5
0.4
0.3
0.2
0.1
0.0
0.1
delta(Irel)
0.0
30.0
40.0
50.0
60.0
70.0
2th

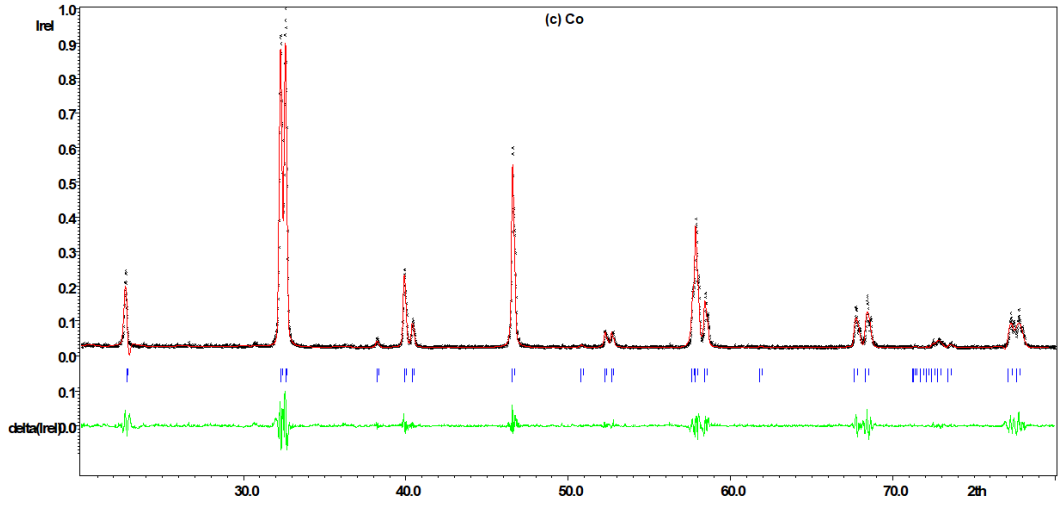
(c) Co
Irel
1.0
0.9
0.8
0.7
0.6
0.5
0.4
0.3
0.2
0.1
0.0
0.1
delta(Irel)
0.0
30.0
40.0
50.0
60.0
70.0
2th

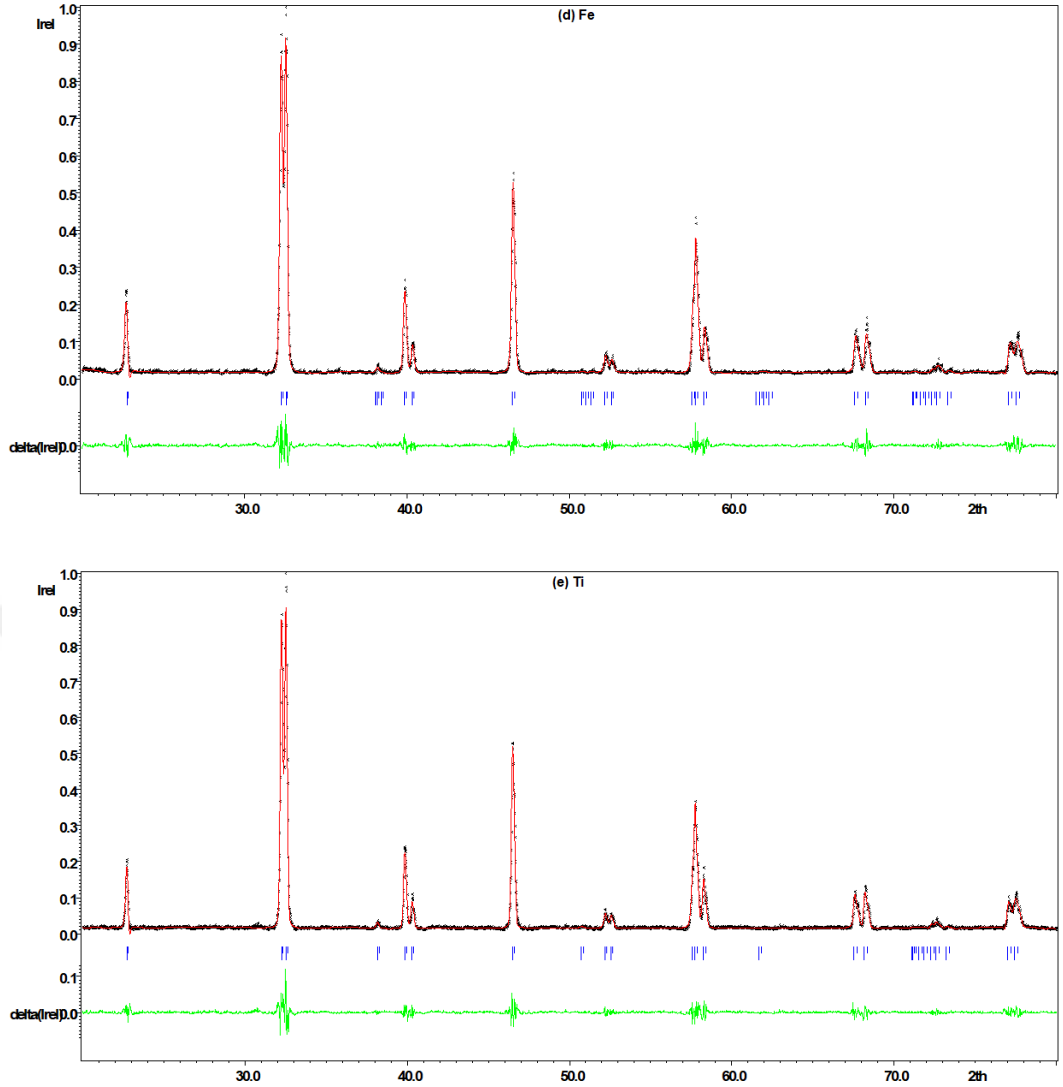

Figure 4.7. Results of Jana refinement of powder *XRD* spectra for $La_{0.8}Sr_{0.2}Mn_{1-x}B_xO_{3\pm\delta}$ compounds with *B:* ***(a) S 0*** *x=0.0,* ***(b) Cu*** *(x=0.1),* ***(c) Co*** *(x=0.1),* ***(d) Fe*** *(x=0.1)* and ***(e) Ti*** *(x=0.1)* at room temperature. Black cross lines represent to experimental data and the red solid lines are calculated fits. Blue vertical bars correspond the Bragg reflections for the space group *($R\bar{3}c$).* The difference pattern between the experimental and calculated data is given at the bottom with the green line.

Moreover, the average crystal size of the materials was calculated using Debby Sherer equation (169);

$$d_{max} = \frac{0.9\lambda}{\beta \cos\theta} \tag{22}$$

where *D* is the crystallites size (nm), λ is the wavelength (nm), β is the full width at half maxima *(FWHM)* and θ is the Bragg's diffraction angle. The calculated values of d_{max} for all samples are given in Table 4.1.

Table 4.1. The structural parameters for $La_{0.8}Sr_{0.2}MnO_3$, $La_{0.8}Sr_{0.2}Mn_{0.9}Cu_{0.1}O_3$, $La_{0.8}Sr_{0.2}Mn_{0.9}Co_{0.1}O_3$, $La_{0.8}Sr_{0.2}Mn_{0.9}Fe_{0.1}O_3$, $La_{0.8}Sr_{0.2}Mn_{0.9}Ti_{0.1}O_3$ samples.

Sample	**S0**	**Cu**	**Co**	**Fe**	**Ti**
Space Group	**R-3c**	**R-3c**	**R-3c**	**R-3c**	**R-3c**
a (Å)	5.503	5.529	5.536	5.540	5.544
c (Å)	13.318	13.365	13.381	13.398	13.416
V (Å)^3	349.360	353.952	355.238	356.190	357.18
GOF	**0.93**	**0.62**	**0.64**	**0.61**	**0.63**
Rp	12.92	8.59	7.37	8.14	8.40
W_{RP}	17.89	11.38	10.28	11.12	11.46
D (nm)	33.68	27.63	51.17	37.60	45.27
Grain Size (µm)	2.45	4.77	2.67	3.27	2.21

4.1.2 Scanning Electron Microscopy *(SEM)* Analyses

The analysis of the microstructure of the ceramic compounds has a crucial importance since one has an idea about the microstructural aspects of the material such as grain structure, grain size distribution, voids, porosities, etc. In accordance with this purpose, the experimental data obtained with the use of scanning electron microscopy are presented in Fig. 4.8, 4.10, 4.12, 4.14 and 4.16 at the same magnification *(x3000).* All micrographs represent the typical results of the perovskite ceramics. Histograms of each *SEM* micrographs display the size distribution of the particles which are shown in the Fig. 4.9, 4.11, 4.13, 4.15 and 4.17. The microscopic images obviously show that all the manganite ceramics are formed of polycrystalline microstructure and most of the grains are almost spherical in shape with nonuniform size distribution. Also, slight agglomeration with varying degrees is obtained with cobalt and titanium substituted samples. The average particle sizes are calculated by using Gaussian fitting method (170) which increases from *2.45 µm* for ***S0*** sample to the *4.77 µm* for ***Cu*** sample, *2.67 µm* for ***Co*** sample, *3.27 µm* for ***Fe*** sample except *2.21 µm* for ***Ti*** sample. The decrease in grain size has been noticed with substituting ***Ti*** (171). Furthermore, as the particle size of all samples was compared to each other, it was observed that the ***Cu*** sample had so much larger particle size.

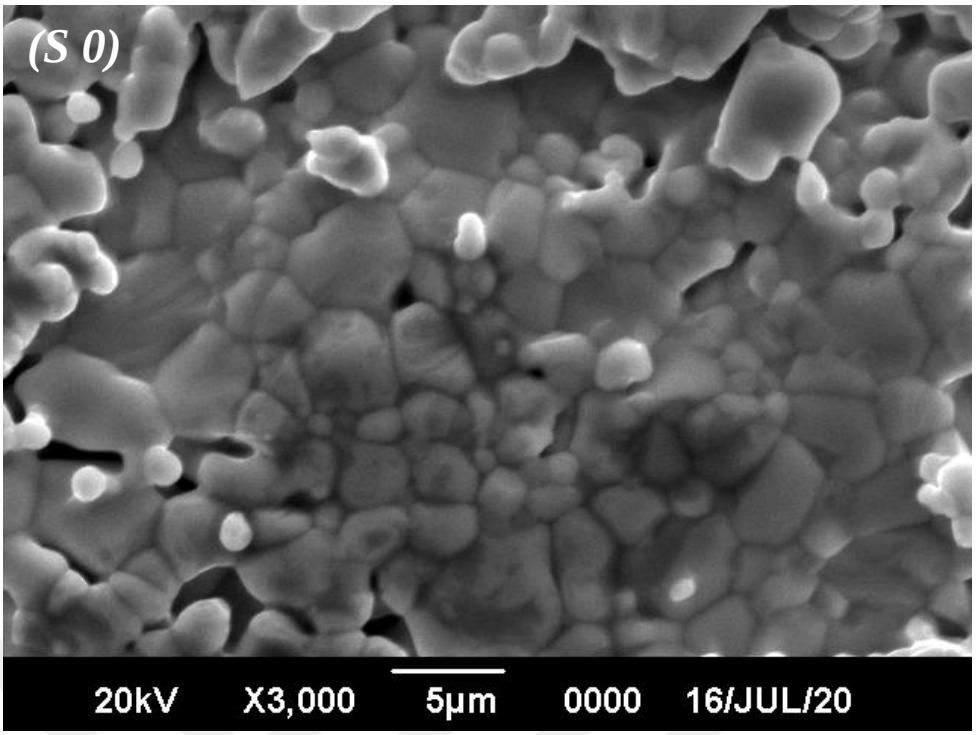

Figure 4.8. *SEM* view of the $La_{0.8}Sr_{0.2}MnO_3$.

As for particle size distribution graphs according to the *SEM* images;

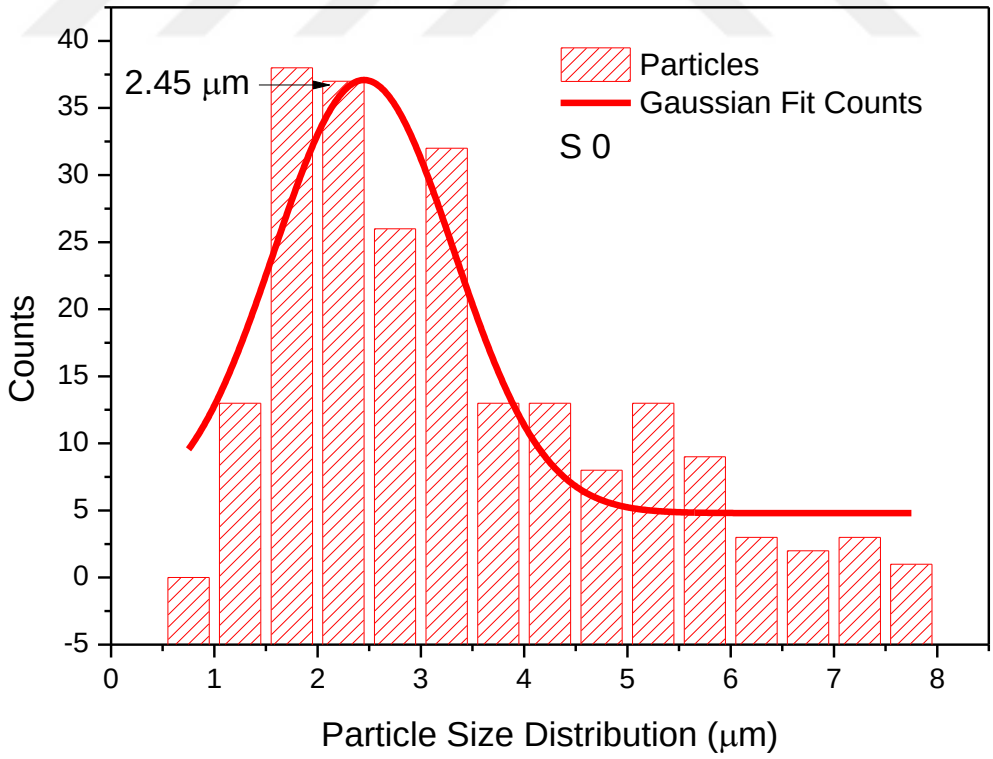

Figure 4.9. Average particle size distribution graph of the $La_{0.8}Sr_{0.2}MnO_3$.

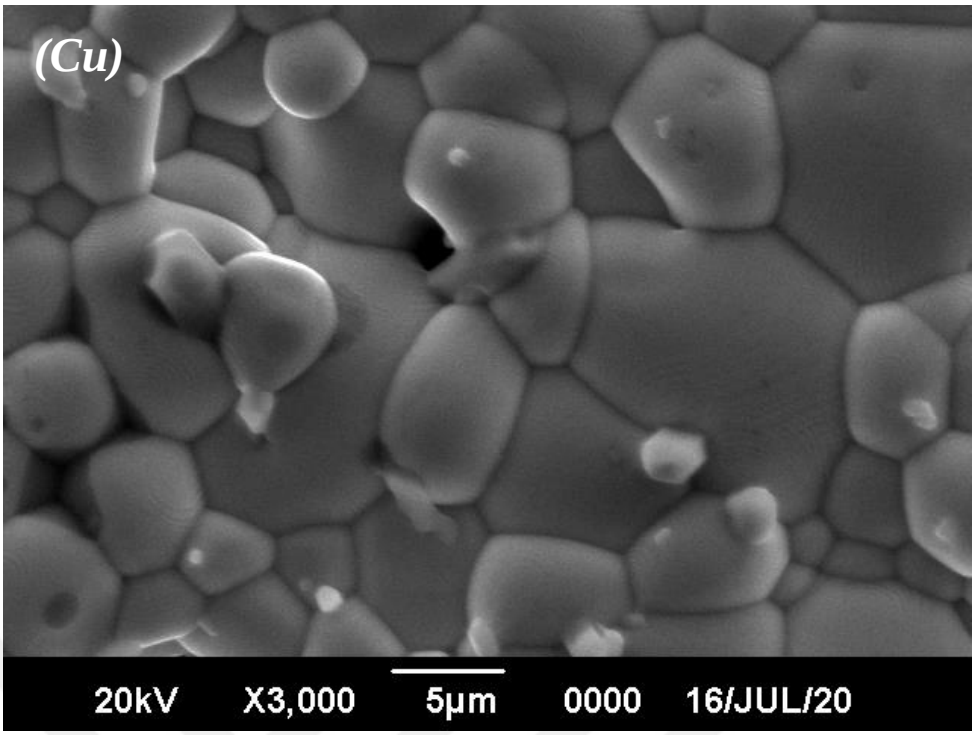

Figure 4.10. *SEM* view of the $La_{0.8}Sr_{0.2}Mn_{0.9}Cu_{0.1}O_3$.

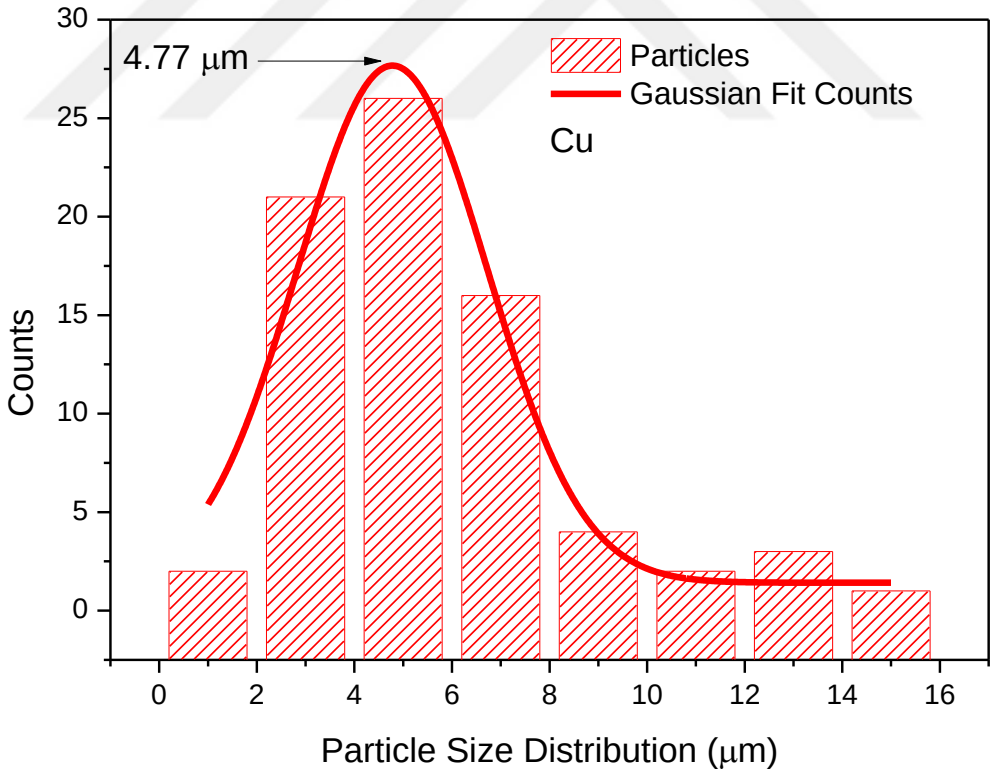

Figure 4.11. Average particle size distribution graph of the $La_{0.8}Sr_{0.2}Mn_{0.9}Cu_{0.1}O_3$.

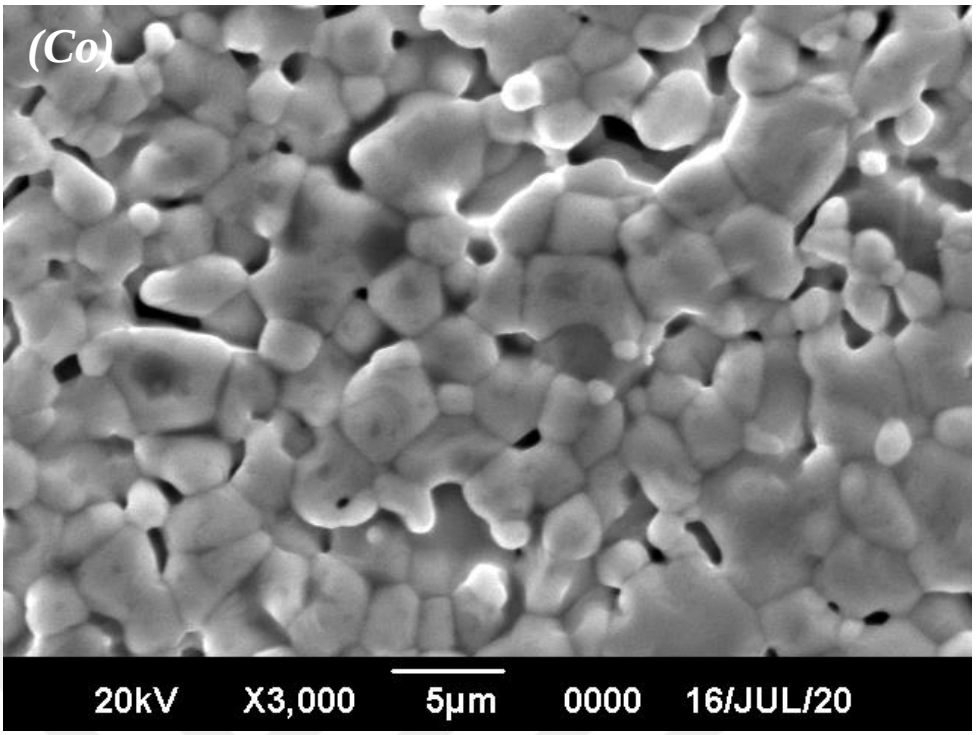

Figure 4.12. *SEM* view of the $La_{0.8}Sr_{0.2}Mn_{0.9}Co_{0.1}O_3$.

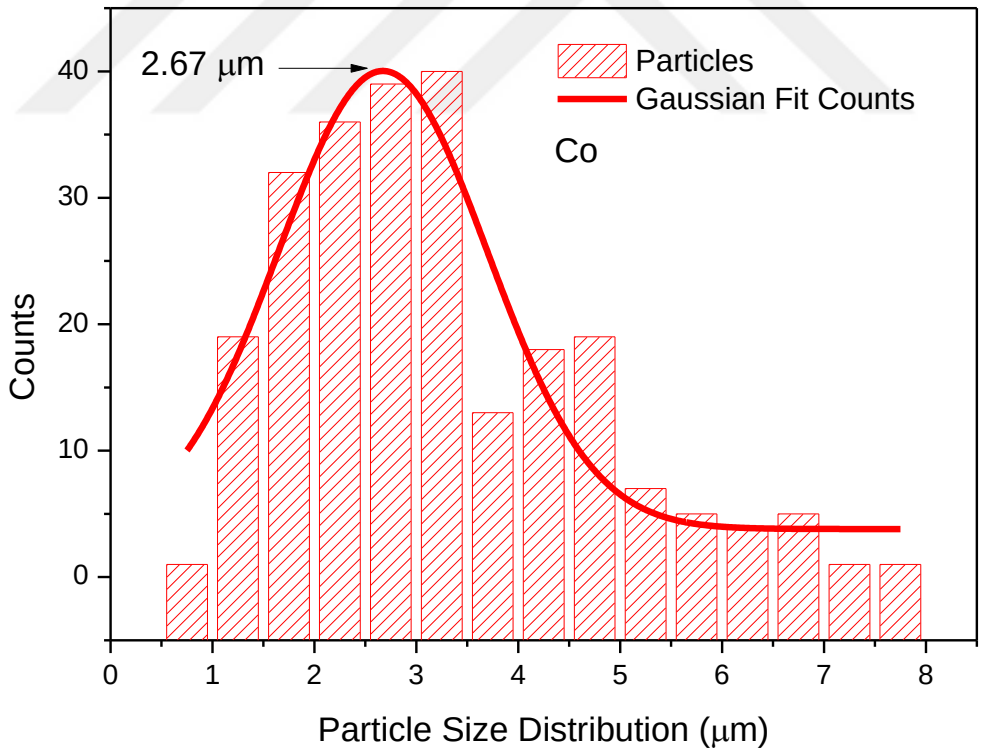

Figure 4.13. Average particle size distribution graph of the $La_{0.8}Sr_{0.2}Mn_{0.9}Co_{0.1}O_3$.

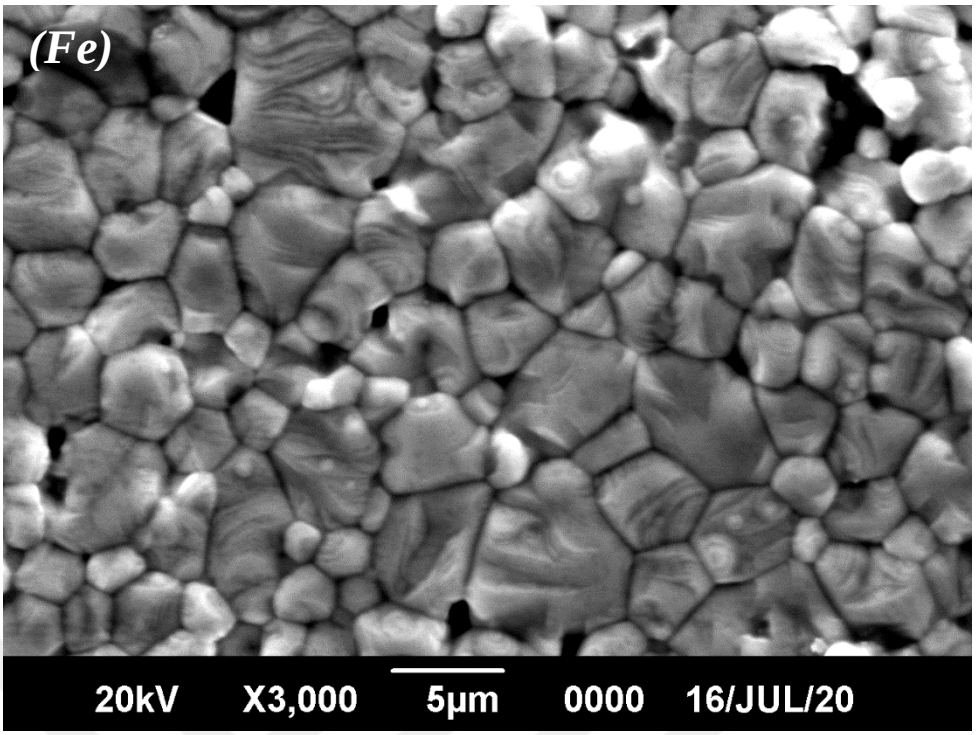

Figure 4.14. *SEM* view of the $La_{0.8}Sr_{0.2}Mn_{0.9}Fe_{0.1}O_3$.

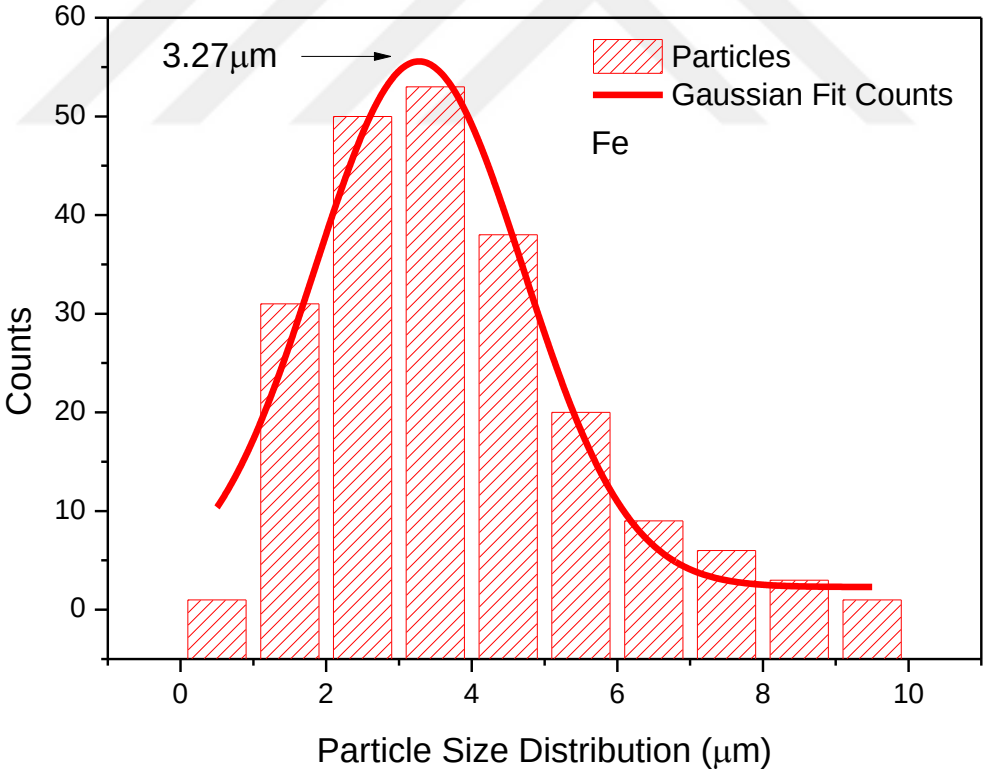

Figure 4.15. Average particle size distribution graph of the $La_{0.8}Sr_{0.2}Mn_{0.9}Fe_{0.1}O_3$.

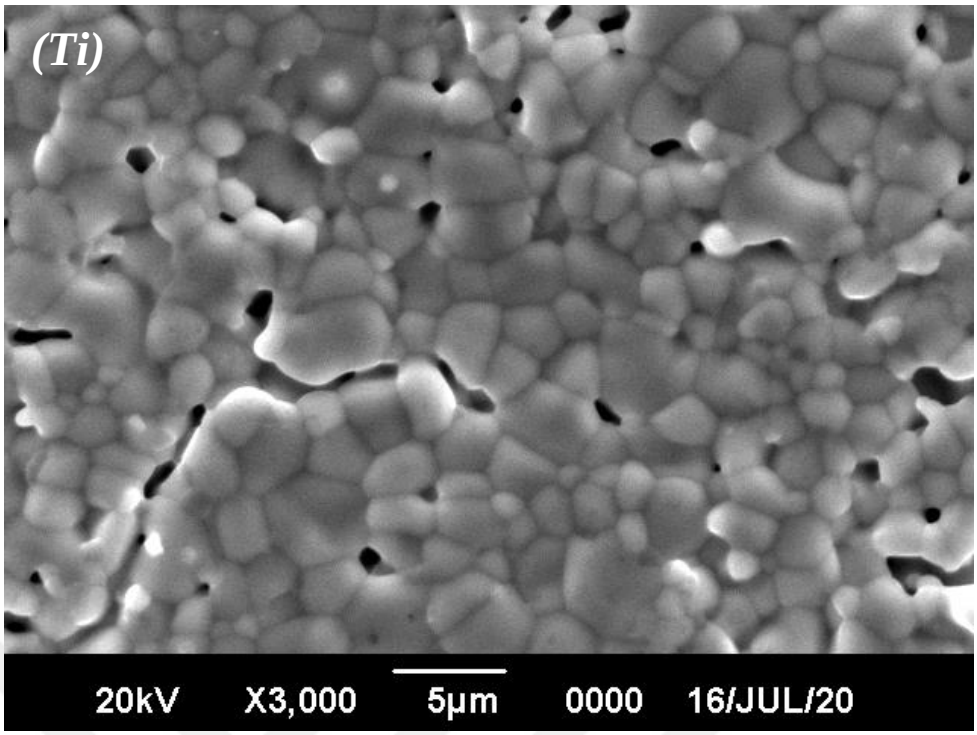

Figure 4.16. *SEM* view of the $La_{0.8}Sr_{0.2}Mn_{0.9}Ti_{0.1}O_3$.

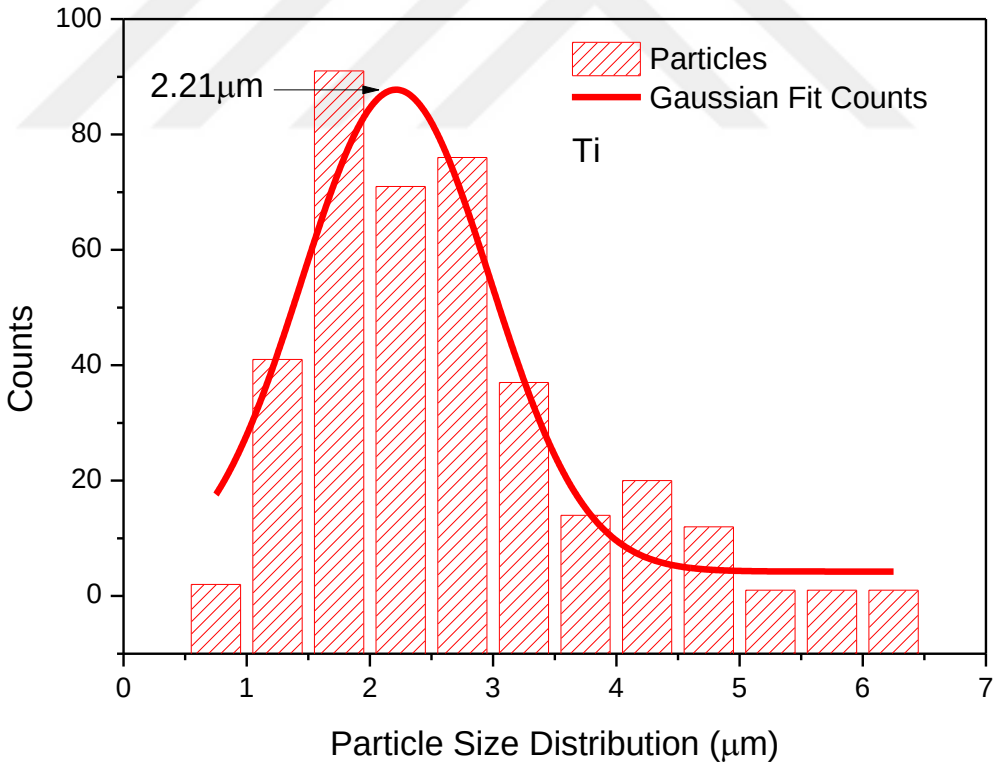

Figure 4.17. Average particle size distribution graph of the $La_{0.8}Sr_{0.2}Mn_{0.9}Ti_{0.1}O_3$.

4.1.3 Electron Dispersive X-Ray *(EDX)* Analyses

Energy dispersive *X*-ray *(EDX)* spectrum shown in Fig. 4.18 indicates the presence of elements in the examined samples close to their chemical composition. Our *EDX* spectra results approve the availability of the main elements ***La, Sr, Mn, O*** and substituted transition metals ***Cu, Co, Fe*** and ***Ti*** in the considered compounds. Moreover, no impurity is noticed in them and their associated quantitative analysis affirms the presence of constituents at almost desired stoichiometry, which are presented in Table 4.2 (24).

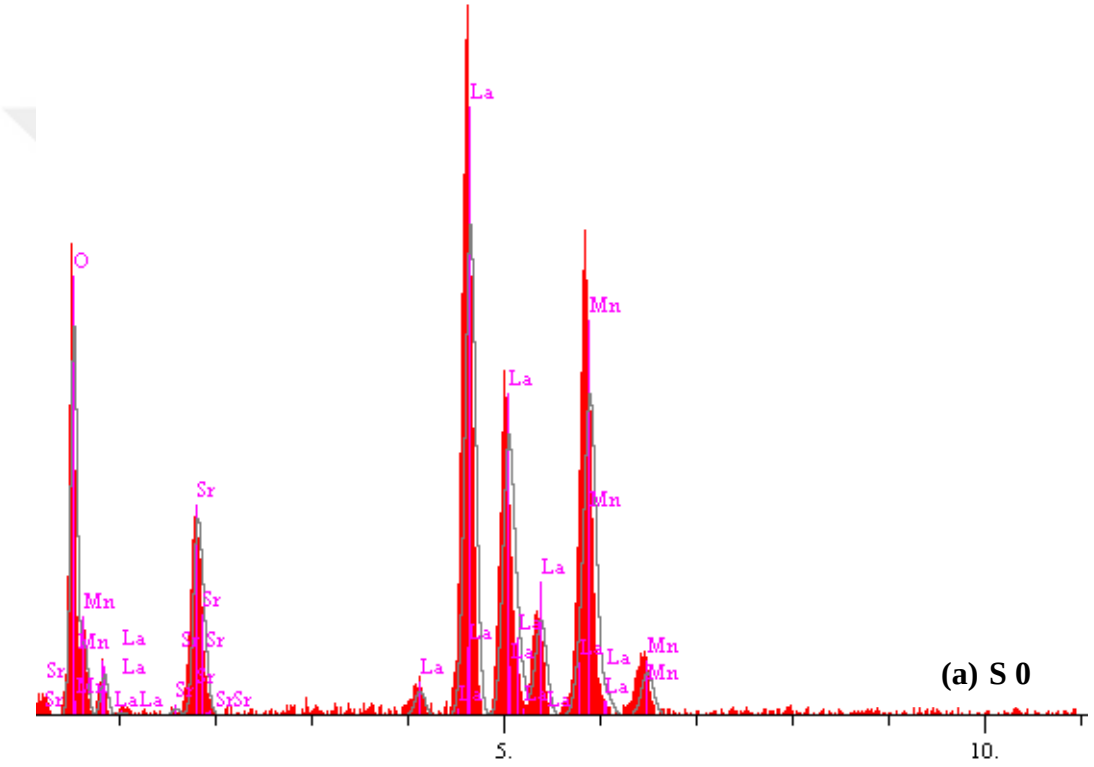

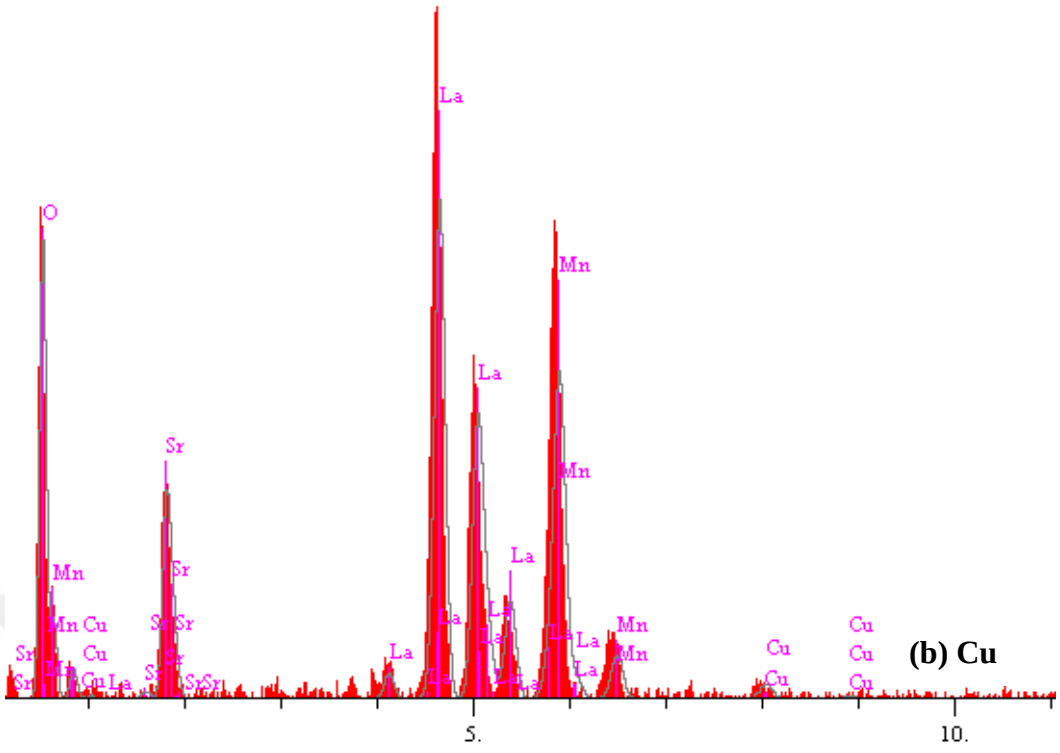

(b) Cu

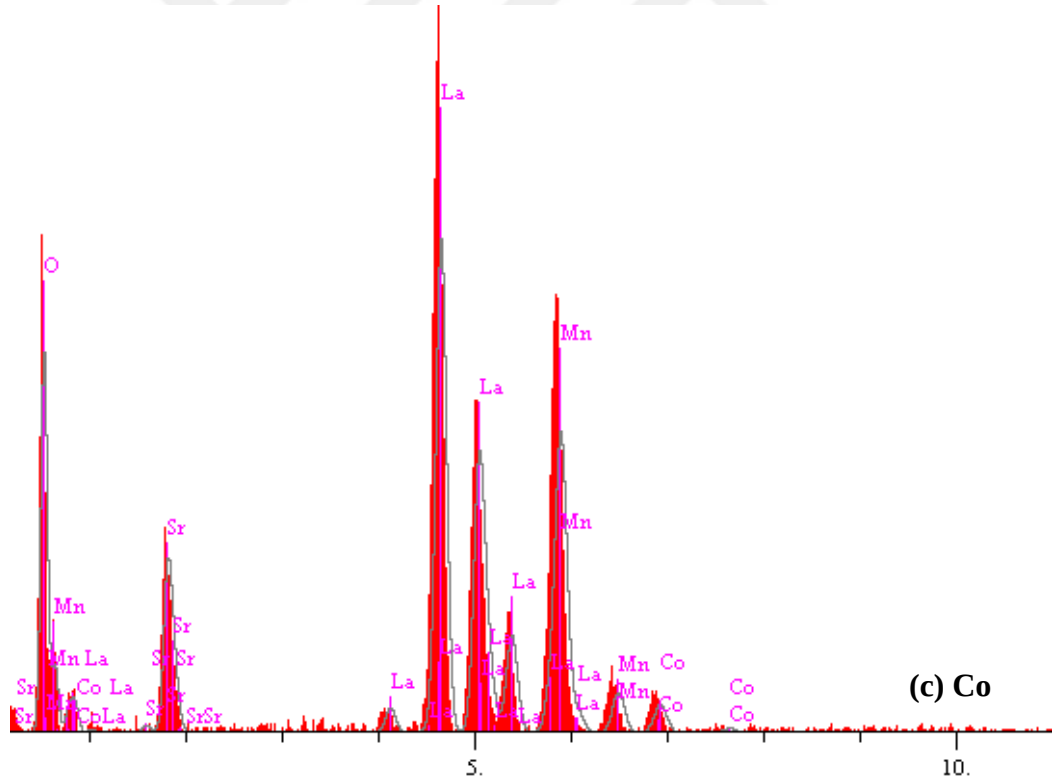

(c) Co

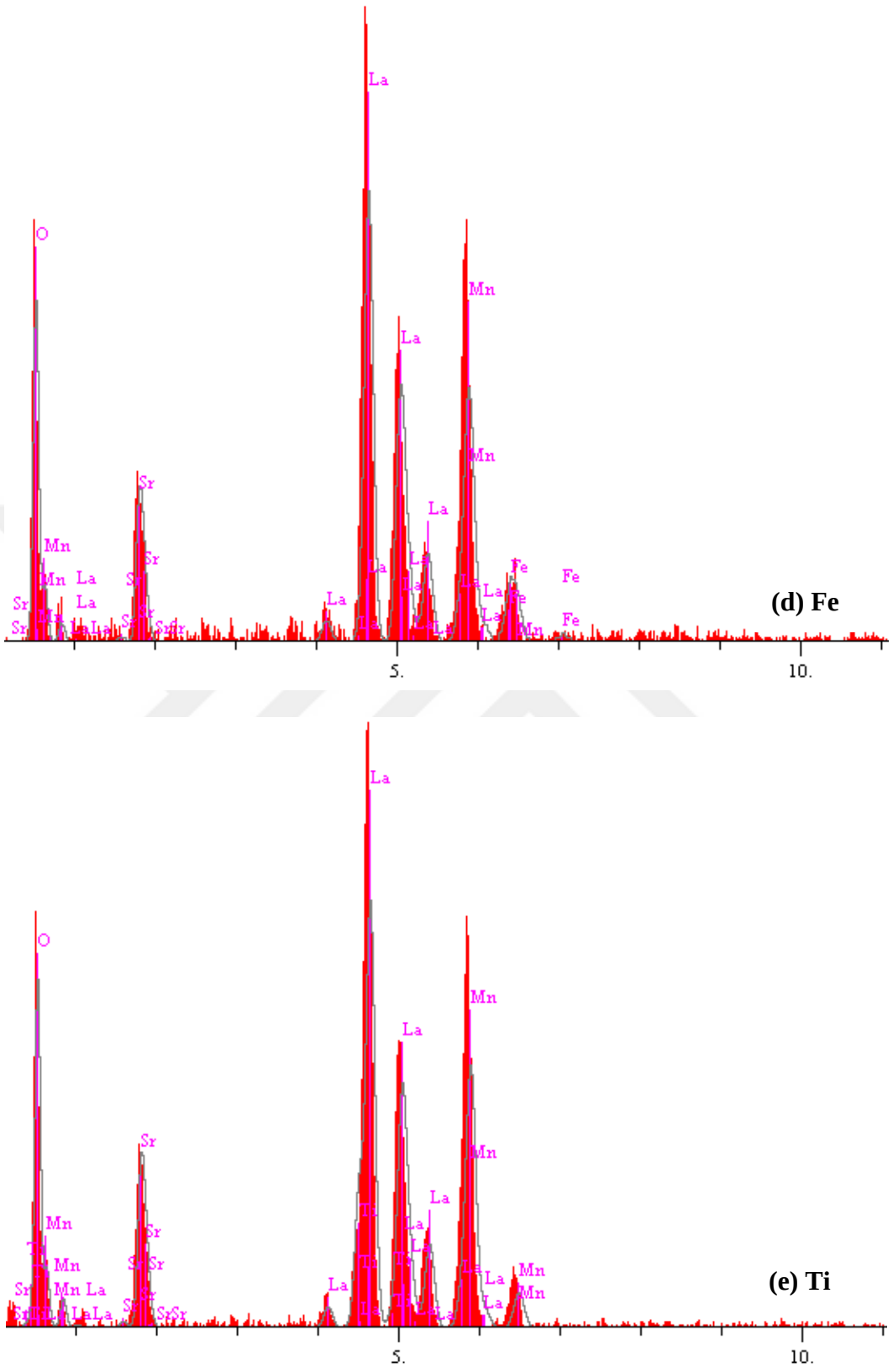

Figure 4.18. *EDX* image of distribution of the elements in $La_{0.8}Sr_{0.2}Mn_{1-x}B_xO_{3\pm\delta}$ compounds with *B:* ***(a) S 0*** *x=0.0,* ***(b) Cu*** *(x=0.1),* ***(c) Co*** *(x=0.1),* ***(d) Fe*** *(x=0.1) and* ***(e) Ti*** *(x=0.1).*

Table 4.2. Concentrations of the elements in $La_{0.8}Sr_{0.2}Mn_{1-x}B_xO_{3\pm\delta}$ compounds with *B:* ***(a) S 0*** *x=0.0,* ***(b) Cu*** *(x=0.1),* ***(c) Co*** *(x=0.1),* ***(d) Fe*** *(x=0.1) and* ***(e) Ti*** *(x=0.1).*

Element	Line	Concentration (wt.%)				
		B_x: S 0	**Cu**	**Co**	**Fe**	**Ti**
O	K_α	20.945	22.982	20.422	20.259	22.470
Mn	K_α	13.241	12.668	12.481	11.644	11.701
B_x	K_α	0	1.126	1.614	2.629	3.697
Sr	L_α	11.651	11.474	10.521	10.323	10.965
La	L_α	54.163	51.750	54.962	55.145	51.168
Total		**100**	**100**	**100**	**100**	**100**

4.1.4 Magneto-Electrical Properties

The magnetization of the unsubstituted *LSMO* sample as regards the temperature curve is plotted in Fig. 4.19. The measurement is done while warming the sample in the absence (zero-field-cooled, *ZFC*) and in the existence (field-cooled, *FC*) of *H=150 Oe* magnetic field. It is obvious from Fig. 4.19 (a) that the *LSMO* sample shows bifurcation between the *ZFC* and *FC M-T* measurements which is characteristic behavior for lanthanum-based manganites (172). We observed a sharp change in the magnetization that refers the transformation of ferromagnetic to paramagnetic state. This *F-P* transformation temperature is called as the Curie temperature, T_C. All prepared manganite systems for this series undergo a *F-P* transition phase at the transition temperature. To find the value of Curie temperature T_C, we applied a method: The obtaining of inflection point of the transition by using the numerical derivation as shown in the inset of Fig. 4.19. The minimum point of the derivative *dM/dT* gives the Curie temperature which are found *321 K* for ***S 0***, *294 K* for ***Cu***, *118 K* for ***Co***, *279 K* for ***Fe***, *219 K* for ***Ti*** and tabulated in Table 4.3. The corresponding parameters are calculated from the magnetization versus temperature plots (Fig. 4.19) and tabulated in Table 4.3. The *TM* substitution caused to drop both the magnetization and Curie temperature (31). It is considered that *TM* substitution decreases the *LSMO* ferromagnetic ratio. Moreover, the *DE* mechanism is

contributed by Mn^{3+} and Mn^{4+} ions (77) (78). By *TM* substituting, Mn^{3+} ions were partially replaced by *TM* atoms which caused the weak *DE* interaction (76).

In addition; the value of the full width at half maximum of the *dM/dT* peaks (see the inset of the Fig. 4.19) is known as transition widths ΔT_C (31). These values show the sharp phase tansition as a function of temperature are listed in Table 4.3.

Table 4.3. Magnetic and electrical-transport parameters evaluated from *M(T), ρ(T), MR %* and *TCR %* graphs for $La_{0.8}Sr_{0.2}MnO_3$, $La_{0.8}Sr_{0.2}Mn_{0.9}Cu_{0.1}O_3$, $La_{0.8}Sr_{0.2}Mn_{0.9}Co_{0.1}O_3$, $La_{0.8}Sr_{0.2}Mn_{0.9}Fe_{0.1}O_3$, and $La_{0.8}Sr_{0.2}Mn_{0.9}Ti_{0.1}O_3$ compounds.

Parameters	**S0**	**Cu**	**Co**	**Fe**	**Ti**
T_{MI} (K)	338	304	97	233	209
T_C (K)	321	294	118	279	219
ΔT_C	7.06	8.80	12.86	8.97	14.68
MR_{max} %	15	23	47	48	24
TCR_{max} %	2.17	2.64	5.10	8.23	0.90

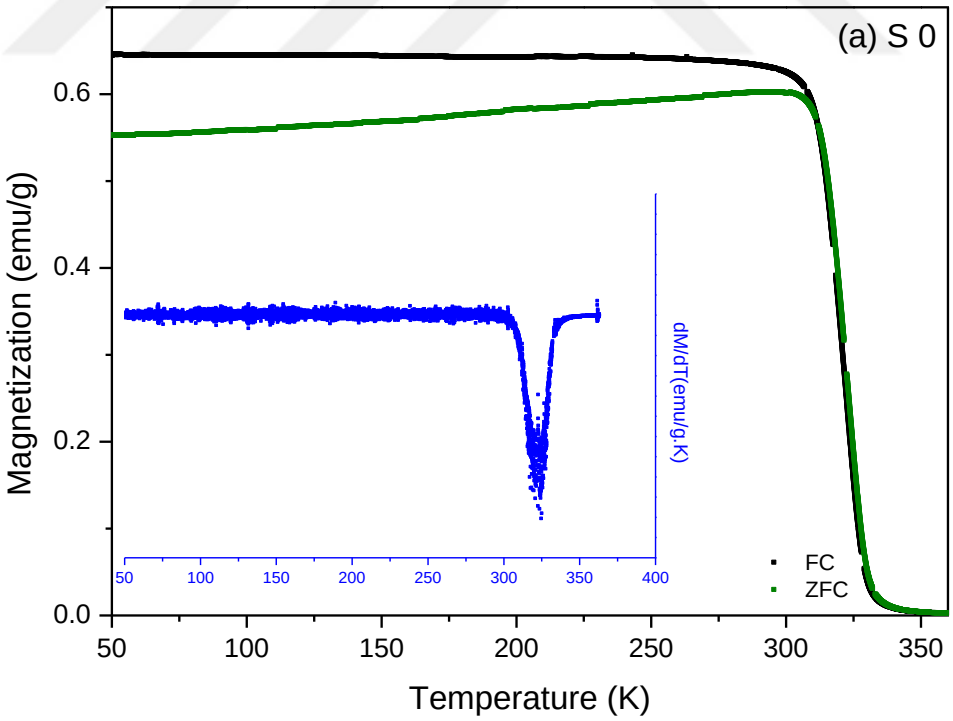

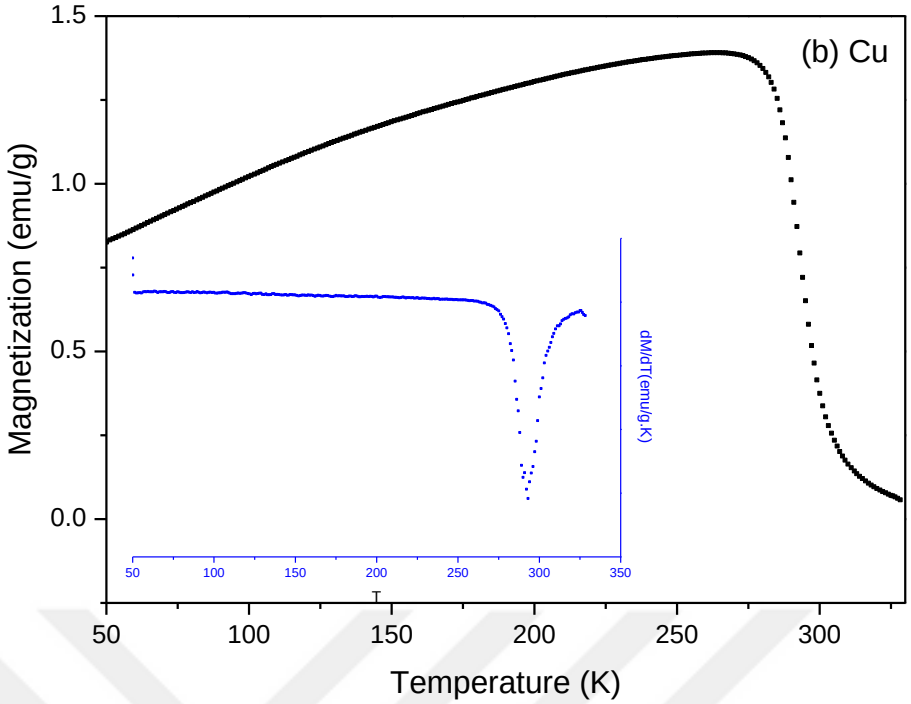
(b) Cu
Magnetization (emu/g)
Temperature (K)
dM/dT(emu/g.K)
T

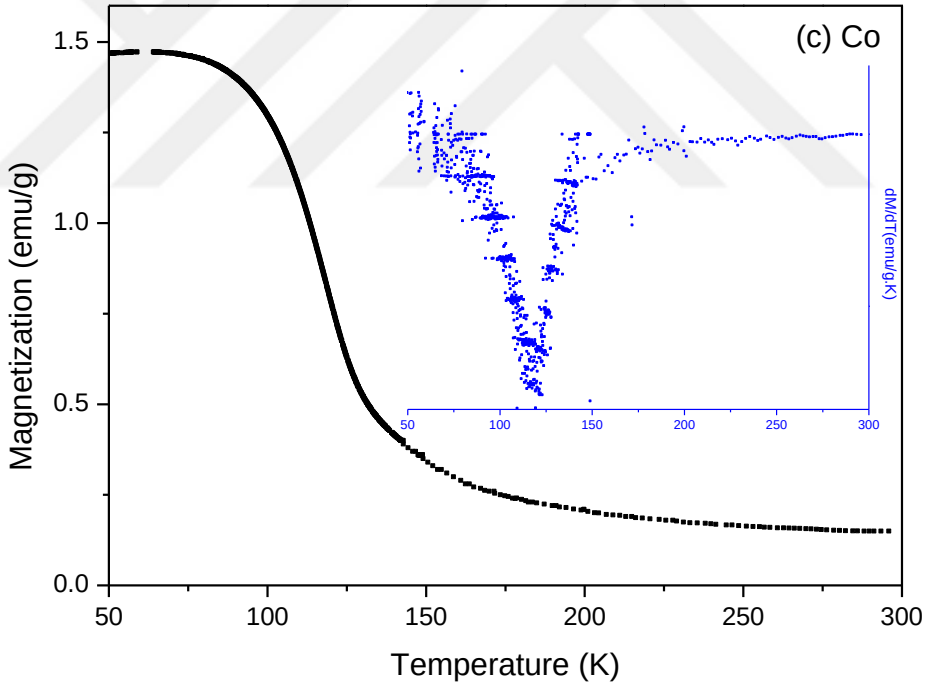
(c) Co
Magnetization (emu/g)
Temperature (K)
dM/dT(emu/g.K)

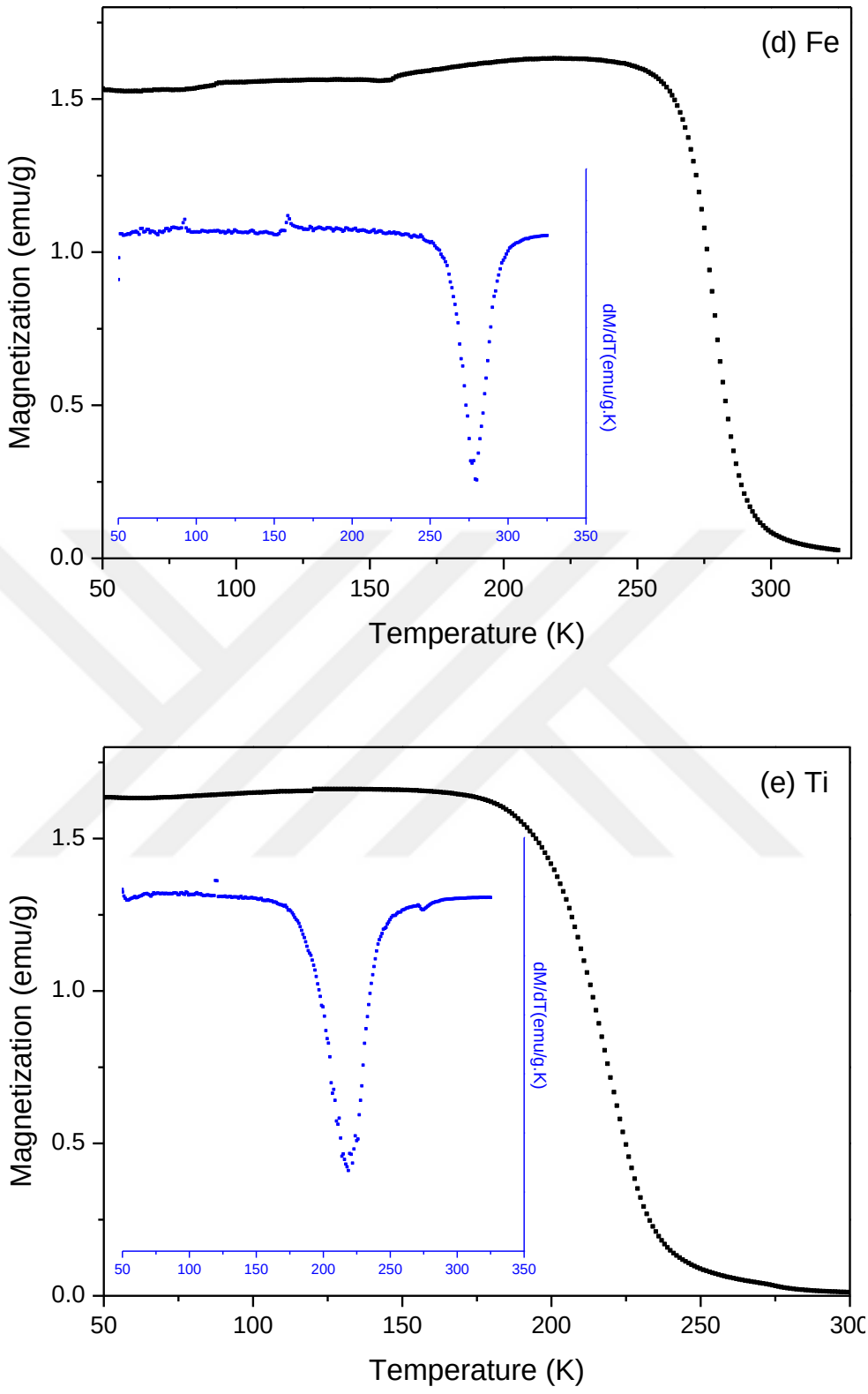

Figure 4.19. Magnetization versus the temperature for $La_{0.8}Sr_{0.2}Mn_{1-x}B_xO_{3\pm\delta}$ compounds with *B:* ***(a) S 0*** *x=0.0,* ***(b) Cu*** *(x=0.1),* ***(c) Co*** *(x=0.1),* ***(d) Fe*** *(x=0.1) and* ***(e) Ti*** *(x=0.1).* The inset shows the F-P phase transition temperature, T_C.

The temperature *(T)*-dependent resistivity *(ρ)* graphs for $La_{0.8}Sr_{0.2}Mn_{1-x}B_xO_{3\pm\delta}$ compounds with B_xO: *x=0, CuO, CoO,* Fe_2O_3, and TiO_2 under magnetic fields *H=0* and *1 T* were plotted in Fig. 4.20. The effect of *TM* substitution on the electrical resistivity was investigated. The transition temperature T_{MI} in which the ferromagnetic-metal to the paramagnetic-insulator phase transition of the samples are also shown in Fig. 4.20. The T_{MI} values are found *338 K* for ***S 0***, *304 K* for ***Cu***, *97 K* for ***Co***, *233 K* for ***Fe***, and *209 K* for ***Ti***. It is clear that all samples show the *FM-PI* phase transition. For $T<T_{MI}$ region, a metallic phase is observed since the resistance of the material increase with increasing temperature. After observing significant hump-corresponds to T_{MI} values a decrease in resistance with increasing temperature is obtained which shows the insulating phase ($T_{MI}<T$ region). Moreover, the existence of a magnetic field decreases resistivity. This could be basically because of the magnetic-domain-based mechanism coupled with either spin scattering at grain boundaries (173) or spin-polarized inter-grain tunnelling (174). The observed decrease in resistivity with the presence of magnetic field can be due to the reduction in correlation length which favors hopping amplitude of charge carriers to move from Mn^{3+} and Mn^{4+}(175). In comparison to the T_{MI} value of ***S 0*** *one by one,* the characteristic temperature decreased by substituting *TM*. It is expected that the substituting *TM* ions perturb the Mn^{3+}-*O*-Mn^{4+} interaction which can minimize the available states for hopping. This perturbation reduced the interaction in the network and, this leads to a decrease in conductivity and the value of T_{MI} (176) (177).

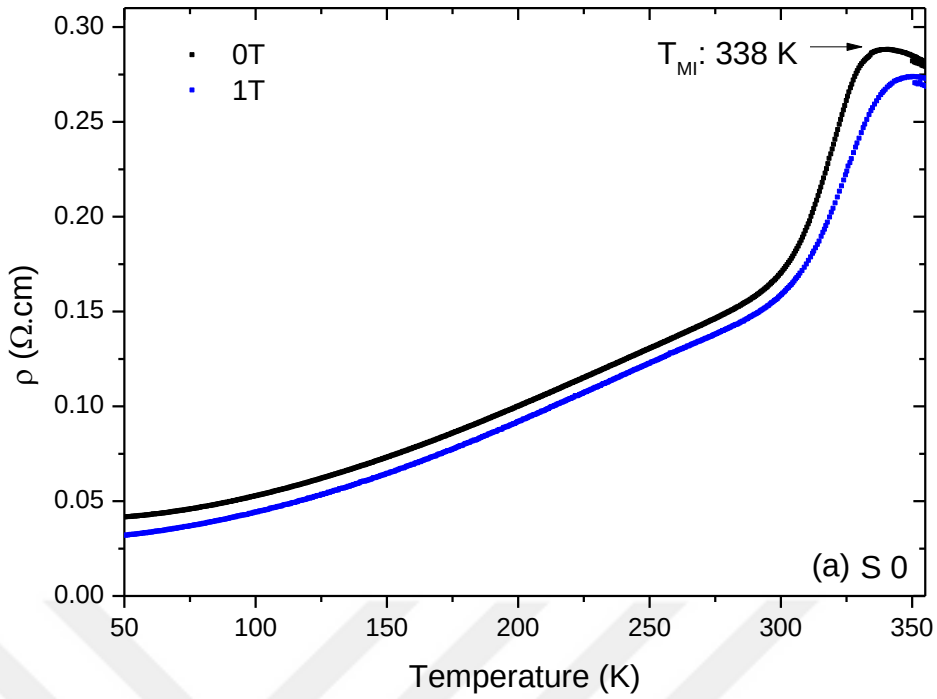
0.30
0.25
0.20
0.15
0.10
0.05
0.00
ρ (Ω.cm)
0T
1T
T$_{MI}$: 338 K
(a) S 0
50
100
150
200
250
300
350
Temperature (K)

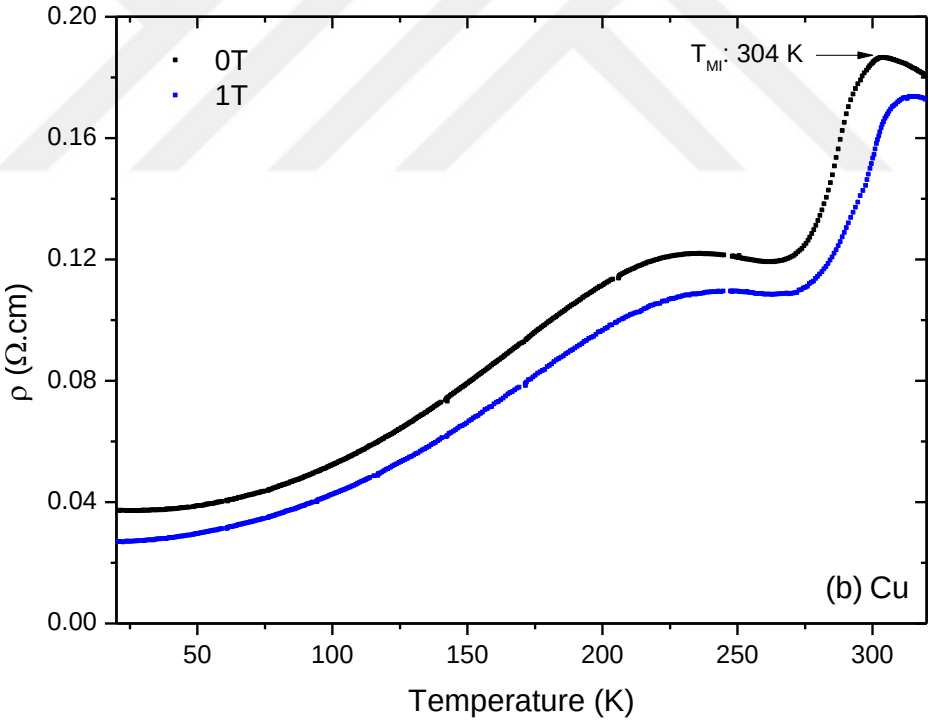
0.20
0.16
0.12
0.08
0.04
0.00
ρ (Ω.cm)
0T
1T
T$_{MI}$: 304 K
(b) Cu
50
100
150
200
250
300
Temperature (K)

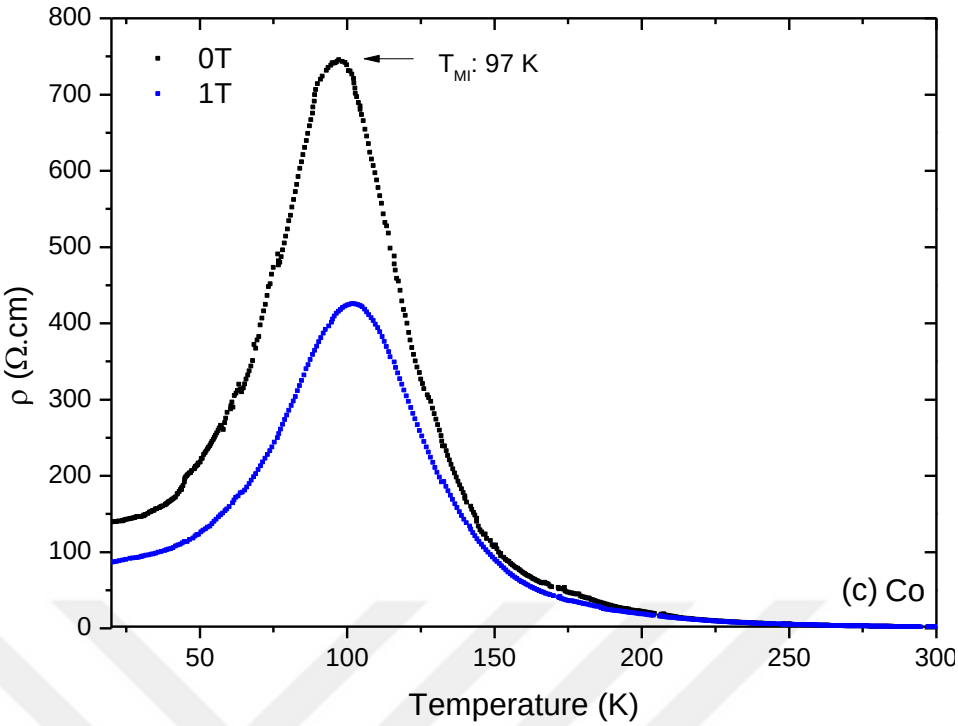
0T
1T
T_{MI}: 97 K
ρ (Ω.cm)
Temperature (K)
(c) Co

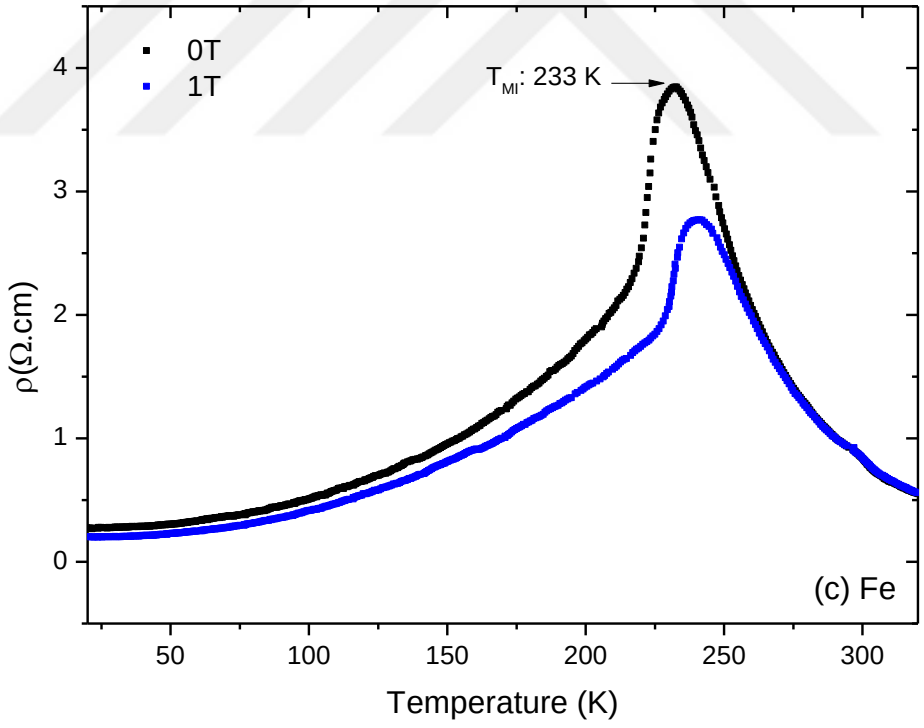
0T
1T
T_{MI}: 233 K
ρ(Ω.cm)
Temperature (K)
(c) Fe

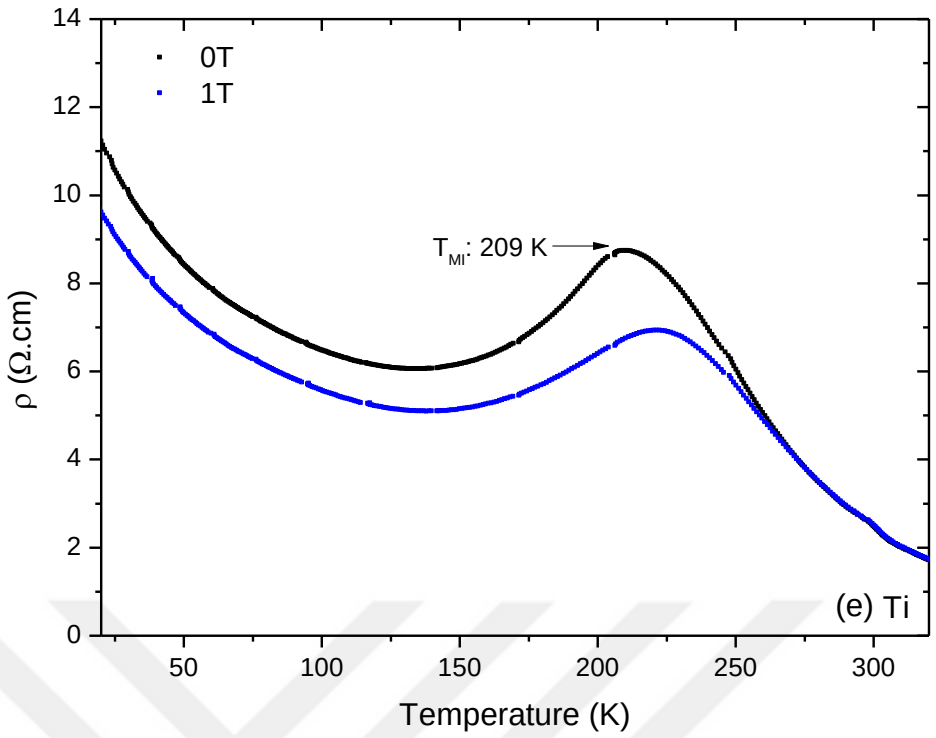

Figure 4.20. Temperature dependence of resistivity in zero field and under magnetic field *1 T* for $La_{0.8}Sr_{0.2}Mn_{1-x}B_xO_{3\pm\delta}$ compounds with *B:* ***(a) S 0*** *x=0.0,* ***(b) Cu*** *(x=0.1),* ***(c) Co*** *(x=0.1),* ***(d) Fe*** *(x=0.1) and* ***(e) Ti*** *(x=0.1).*

Furthermore; Fig. 4.22 shows temperature dependence of temperature coefficient resistance *(TCR).* The *TCR* value is highlighted as a major parameter for examining the sensitivity of uncooled infrared bolometers which is defined as;

$$TCR(\%) = [\left(\frac{1}{\rho}\right) x \left({d\rho}/{dT}\right)]x100\% \quad (23)$$

where ρ is the sample resistivity and *T* is the temperature. Many significant factors can influence the peak value of *TCR*, including sintering time and temperature, ionic radius, preparation method, and resistivity of the samples (178). The high *TCR* values of *LSMO* can possibly effect their efficiency in photoelectric (uncooled bolometers or infrared detectors) at room-temperature. The peak values of *TCR* for all samples are given in Table 4.3. According to the results, the greatest *TCR* value is obtained with *8.23 % K^{-1}* for ***Fe*** substituted sample.

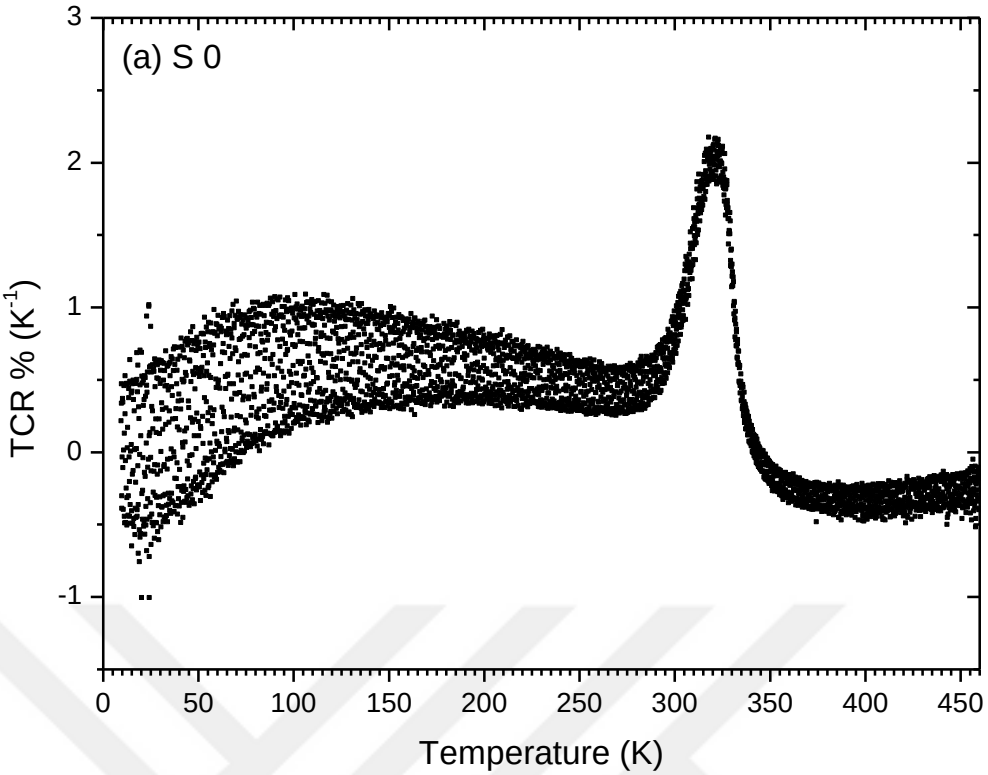
(a) S 0
TCR % (K-1)
Temperature (K)
3
2
1
0
-1
0
50
100
150
200
250
300
350
400
450

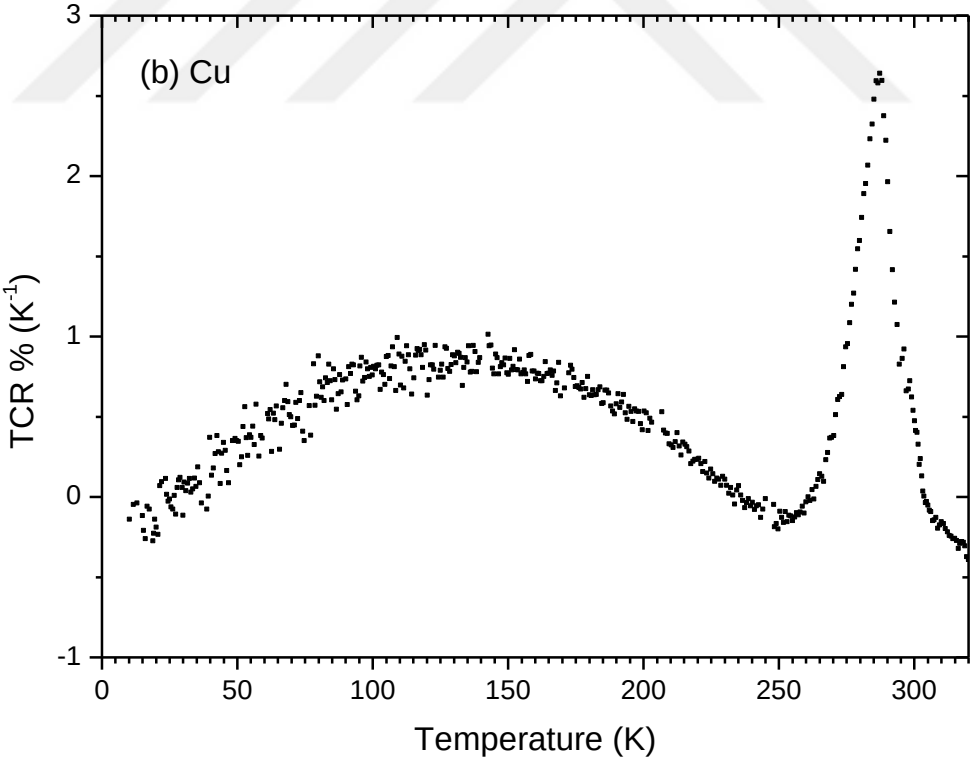
(b) Cu
TCR % (K-1)
Temperature (K)
3
2
1
0
-1
0
50
100
150
200
250
300

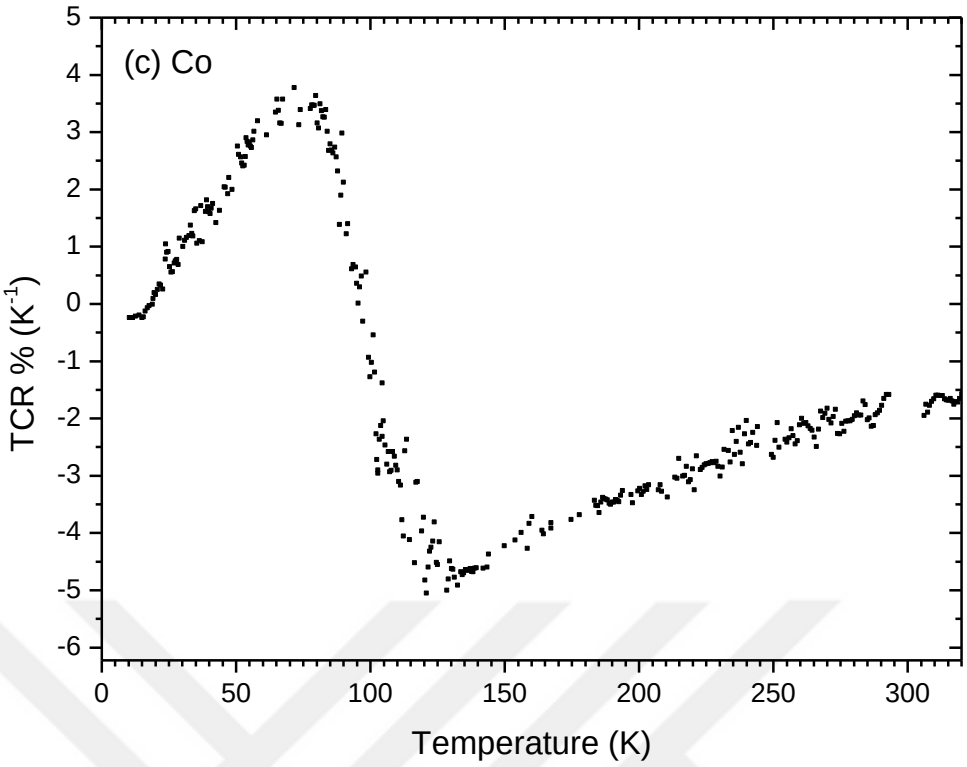
(c) Co
TCR % (K-1)
Temperature (K)
5
4
3
2
1
0
-1
-2
-3
-4
-5
-6
0
50
100
150
200
250
300

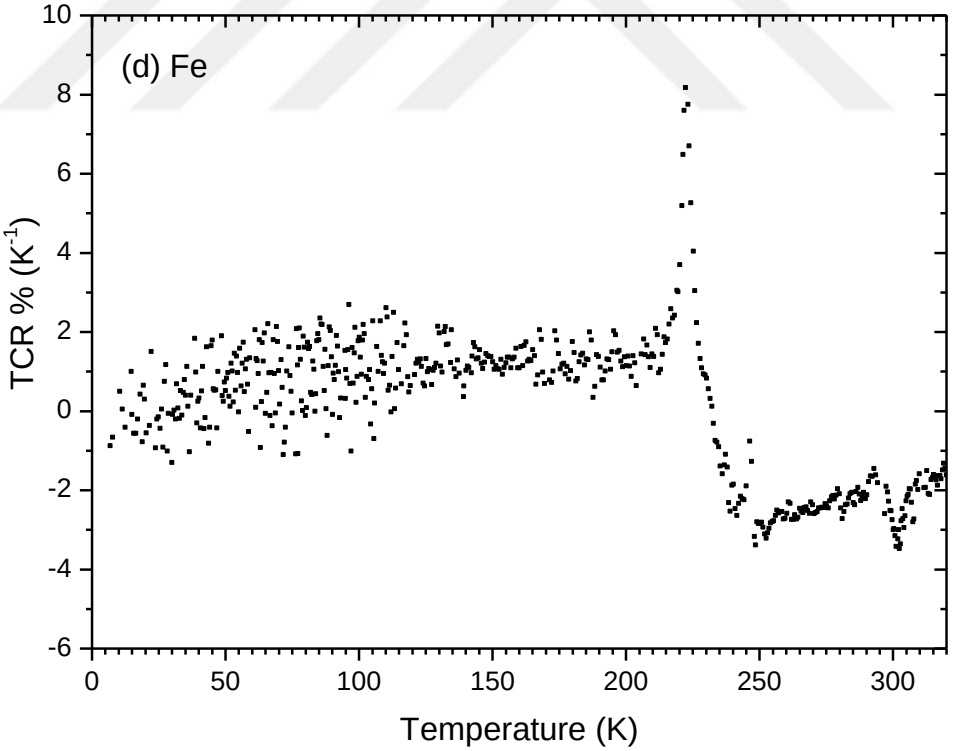
(d) Fe
TCR % (K-1)
Temperature (K)
10
8
6
4
2
0
-2
-4
-6
0
50
100
150
200
250
300

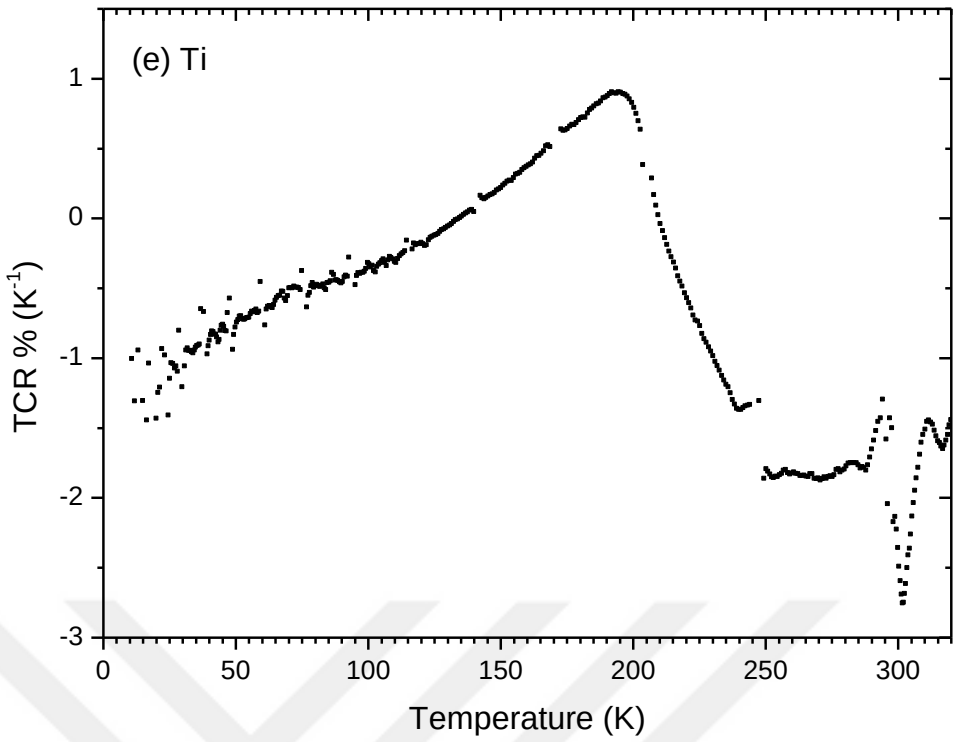

Figure 4.21. Temperature coefficient of resistance *(TCR)* with respect to temperature curves of $La_{0.8}Sr_{0.2}Mn_{1-x}B_xO_{3\pm\delta}$ compounds with *B:* ***(a) S 0*** *x=0.0,* ***(b) Cu*** *(x=0.1),* ***(c) Co*** *(x=0.1),* ***(d) Fe*** *(x=0.1) and* ***(e) Ti*** *(x=0.1).*

The magnetoresistance *(MR)* ratio is defined as;

$$MR\ \% = \frac{(\rho_H - \rho_0)}{\rho_0} x100 \qquad (24)$$

where ρ_0 and ρ_H are the resistivity in zero and applied magnetic field of *1 T*, respectively. The greatest *MR %* values are intended for the technological applications which illustrate a strong response of the sample resistivity to the applied magnetic field (179) (180). According to our results, the *MR* percentage is negative for all samples which indicates that the sample resistivity decreases with the external magnetic field. All *MR* percentage values were tabulated in Table 4.3. The largest *MR* percentage value of *48 %* was calculated in the ***Fe*** substituted sample at about *230 K.*

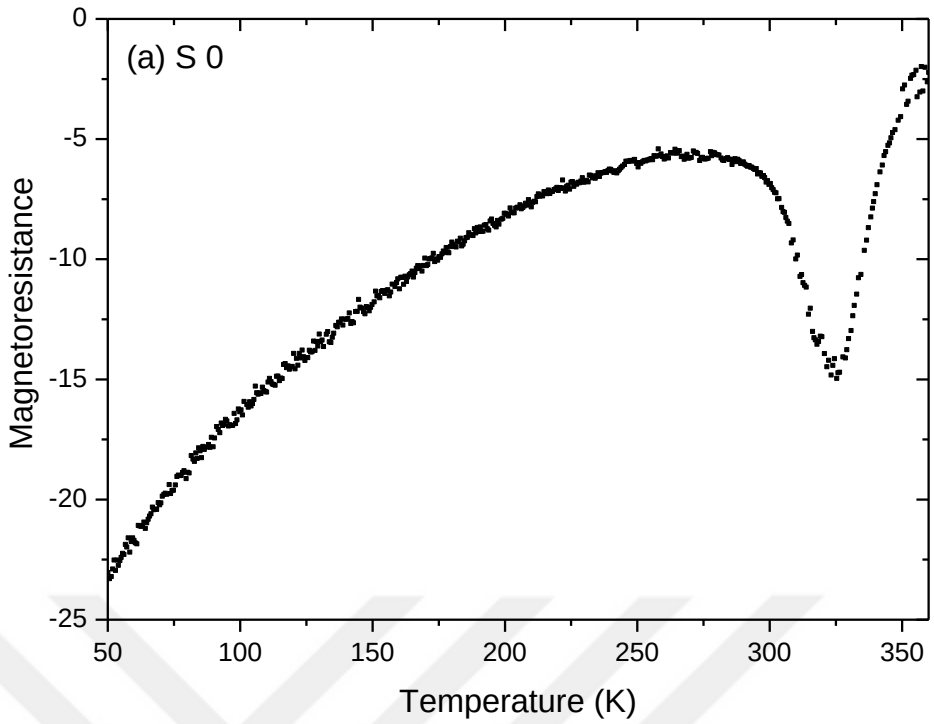
(a) S 0
Magnetoresistance
0
-5
-10
-15
-20
-25
50
100
150
200
250
300
350
Temperature (K)

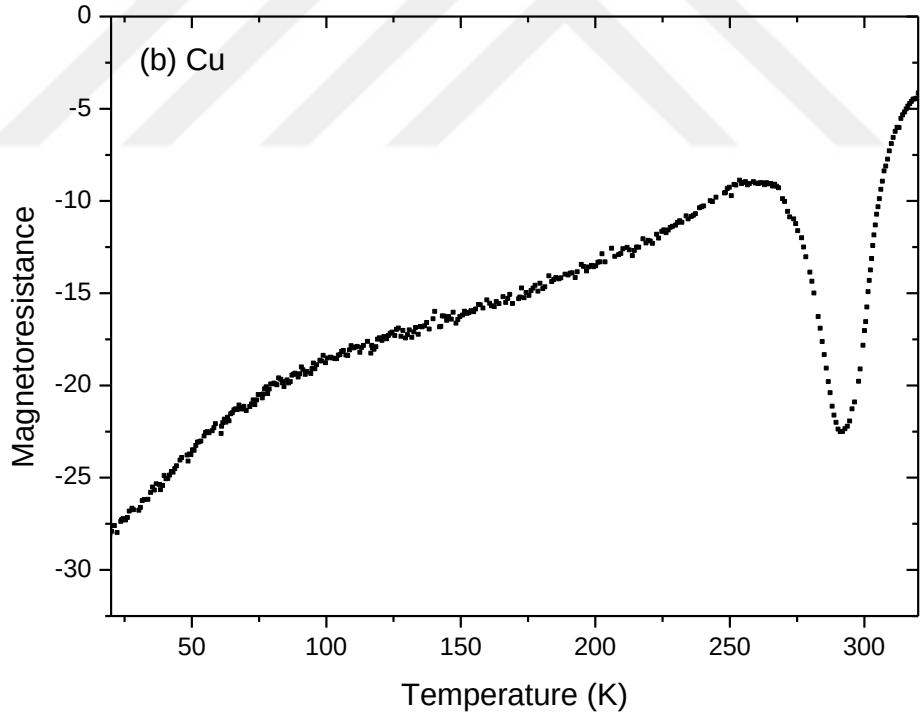
(b) Cu
Magnetoresistance
0
-5
-10
-15
-20
-25
-30
50
100
150
200
250
300
Temperature (K)

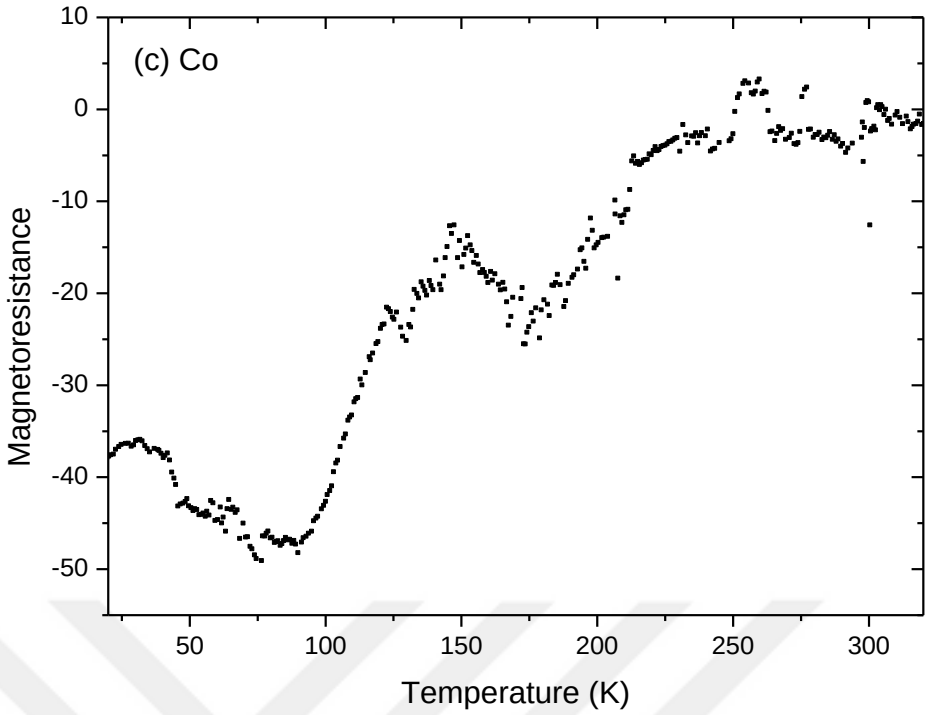
(c) Co
Magnetoresistance
Temperature (K)
10
0
-10
-20
-30
-40
-50
50
100
150
200
250
300

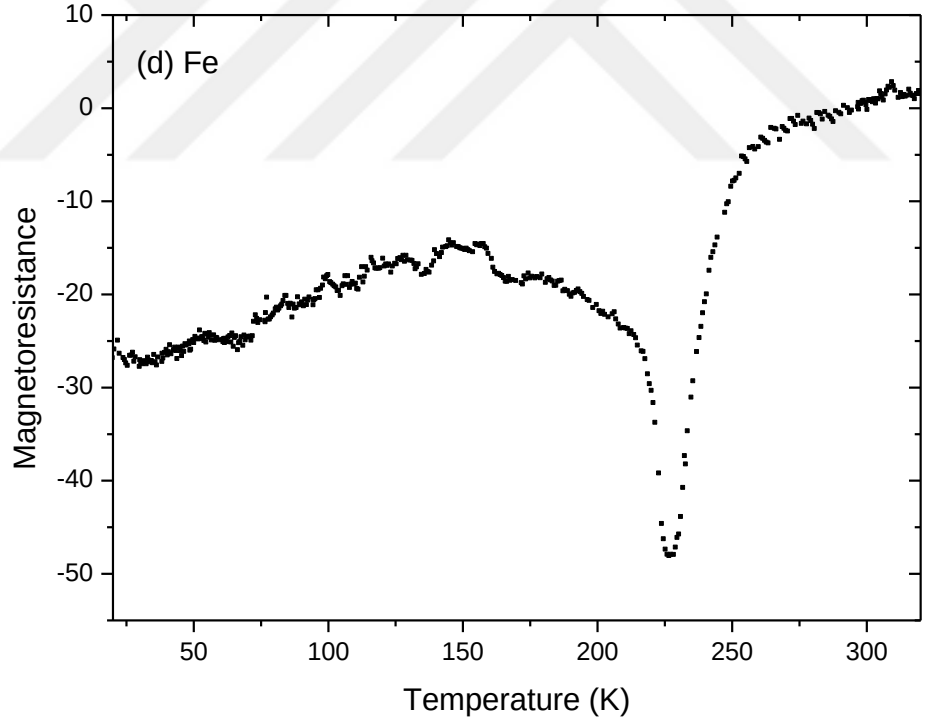
(d) Fe
Magnetoresistance
Temperature (K)
10
0
-10
-20
-30
-40
-50
50
100
150
200
250
300

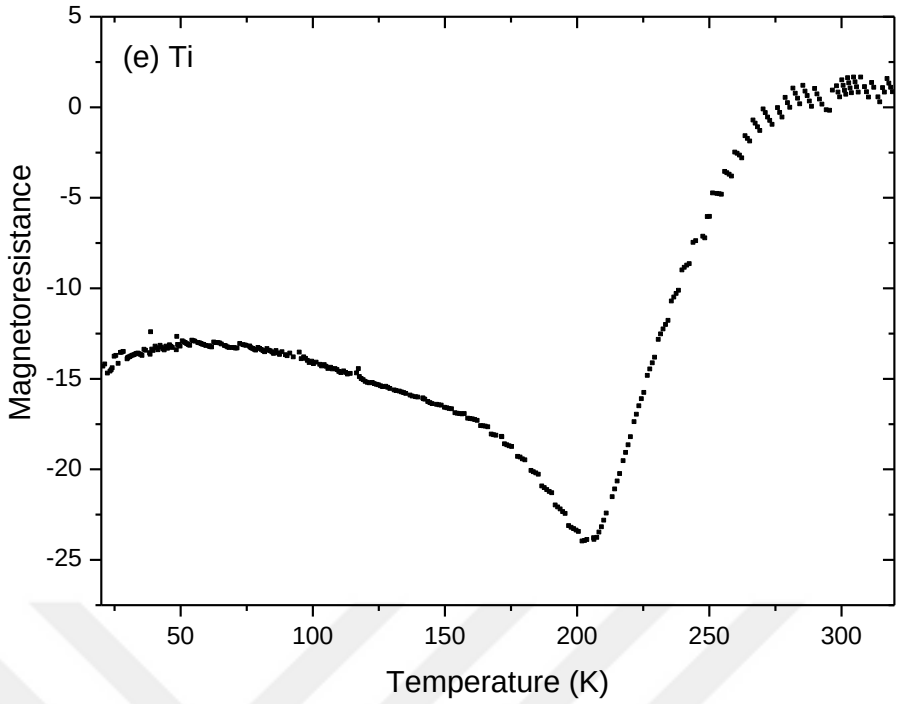

Figure 4.22. Magnetoresistance versus temperature curves of $La_{0.8}Sr_{0.2}Mn_{1-x}B_xO_{3\pm\delta}$ compounds with *B:* ***(a) S 0*** *x=0.0,* ***(b) Cu*** *(x=0.1),* ***(c) Co*** *(x=0.1),* ***(d) Fe*** *(x=0.1) and* ***(e) Ti*** *(x=0.1)* computed with *H=1 T* applied magnetic field.

4.1.5 Conduction Mechanism Analyses

Electrical transport is one of the most important physical properties of manganites. In order to analyze the conduction system for all samples, so many fitting models are applied in the Origin Proggramme.

First of all, the whole temperature range is analized in two sections to understand magneto-conductive transport. The range of the first section is below T_{MI}. It is called as ferromagnetic-metallic region *(FM)* and the range of second one is the paramagnetic insulating region *(PI)* above T_{MI}.

Many models have tried to find out the effect of transition metals on the electrical transport mechanism of *LSMO* compounds. In order to understand the electrical conduction mechanism at low-temperature region $(T<T_{MI})$ (both the case of applied and unapplied magnetic field), the electrical resistivity data are fitted using the following equations:

- Residual weak electron-electron scattering equation:

$$\rho = \rho_0 - \rho_{0.5}T^{0.5} + \rho_2 T^2 \quad (17)$$

- Residual weak electron-electron and electron-phonon scattering equation:

$$\rho = \rho_0 - \rho_{0.5}T^{0.5} + \rho_2 T^2 + \rho_5 T^5 \quad (18)$$

where ρ_0 is the residual resistivity due to domain or grain boundaries, $\rho_{0.5}T^{0.5}$ is represented to the weak localization because of the electron-electron *(e-e)* interaction scattering from static in-homogeneity in *3D* (181), the term of $\rho_2 T^2$ gives the resistivity due to the electron-electron scattering duration in ferromagnetic-metallic *(FM)* state (182), the term of $\rho_5 T^5$ is shows to the electron-phonon *(e-p)* inteference in *FM* state (183). The well-fitted graphs are given in Fig. 4.23 and the obtained coefficients are given in Table 4.4. In order to deeply analysing of which models intervene in the conduction mechanism, the square values of lineer correlation coefficient *(R^2)* are chosen for the well-defined fit. If R^2 value is nearly ≈1, the chosen model is applicable.

When our fitting data were compared, a decrease in the corresponding coefficients by applying *1 T* magnetic field was noticed. That also shows us the decrease of the resistivity values.

Several fitting models were used to examine the alteration of the electrical resistivity in the range of above T_{MI} for manganites. In this thesis, the electrical resistivity data at high-temperature region *($T>T_{MI}$)* (both the case of applied and unapplied magnetic field) was ideally explained by two different models:

- Adiabatic Small Polaron Hopping *(ASPH)* (184)

$$\rho = \rho_a T \exp(\frac{E_a}{k_B T}) \quad (13)$$

Also, the value of E_a was calculated by multiplying the Boltzmann constant with the experimental data of coefficient *A* which is obtained from the fitting data as seen below;

$$A = \frac{E_a}{k_B} \quad (14)$$

- Mott's 3D-Variable Range Hopping *(3D-VRH)*

$$\rho = \rho_0 \exp(\frac{T_0}{T})^{\frac{1}{4}} \quad (10)$$

where ρ_a, ρ_0 is residual resistivity, T_0 characteristic temperature, k_B is Boltzmann constant, E_a is activation energy for hopping conduction, and T is absolute temperature. Furthermore, Mott characteristic temperature T_0 can be expressed as;

$$T^0 = \frac{18}{k_B N(E_F) a^3} \quad (11)$$

where k_B is the Boltzmann's constant, $N(E_F)$ is the density of states and a is the localization length. By using the Eq. 26, the values of $N(E_F)$ were computed and given in Table 4.4.

According to the literature (185) (35), Variable Range Hopping *(VRH)* model is used for $T_{MI}<T<\theta_D/2$; and Adiabatic Small Polaron Hopping *(ASPH)* is used for $T>\theta_D/2$. Based on the values of R^2 coefficient, both adiabatic *ASPH* and *3D-VRH* models are well-fitted for our results. Also, we calculated the Debye temperature for only the ***Co*** sample to determine the high-temperature range. The graph of $ln(\rho /T)$ versus $(1/T)$ gives us the Debye temperature (θ_D). It is seen in the inset of Fig. 4.23 (c). The high-temperature range starts at the value of $\theta_D/2$. Fig. 4.23 shows the well-fitted curves and Table 4.5 gives the corresponing coefficient for high temperature region.

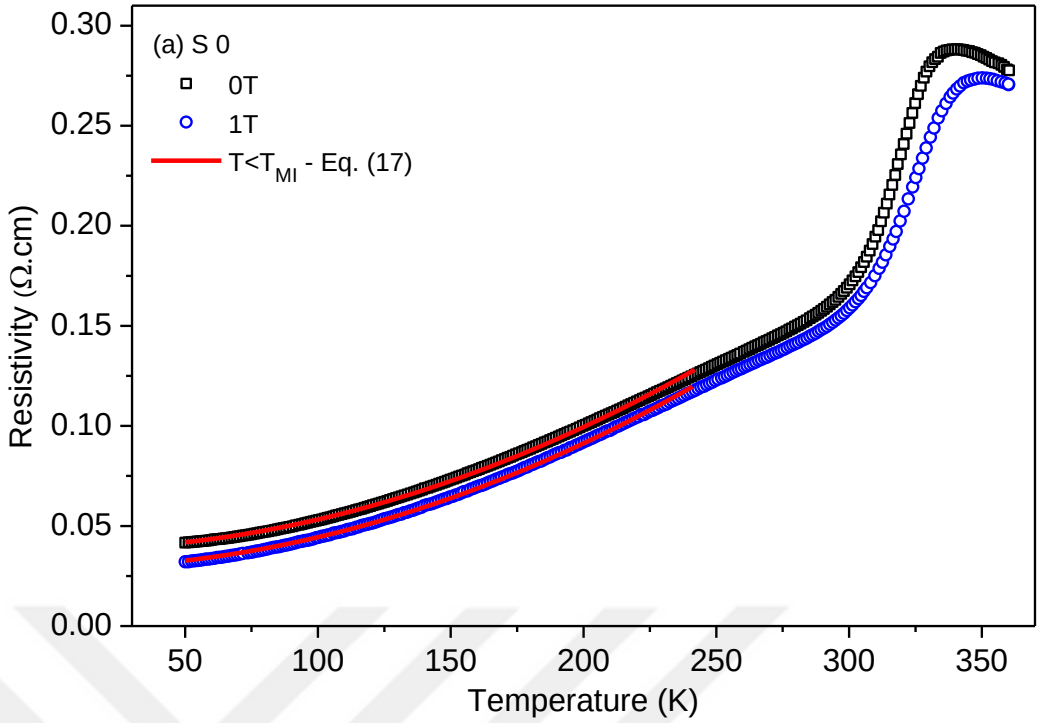
(a) S 0
0T
1T
T<T_MI - Eq. (17)
Resistivity (Ω.cm)
Temperature (K)
0.00
0.05
0.10
0.15
0.20
0.25
0.30
50
100
150
200
250
300
350

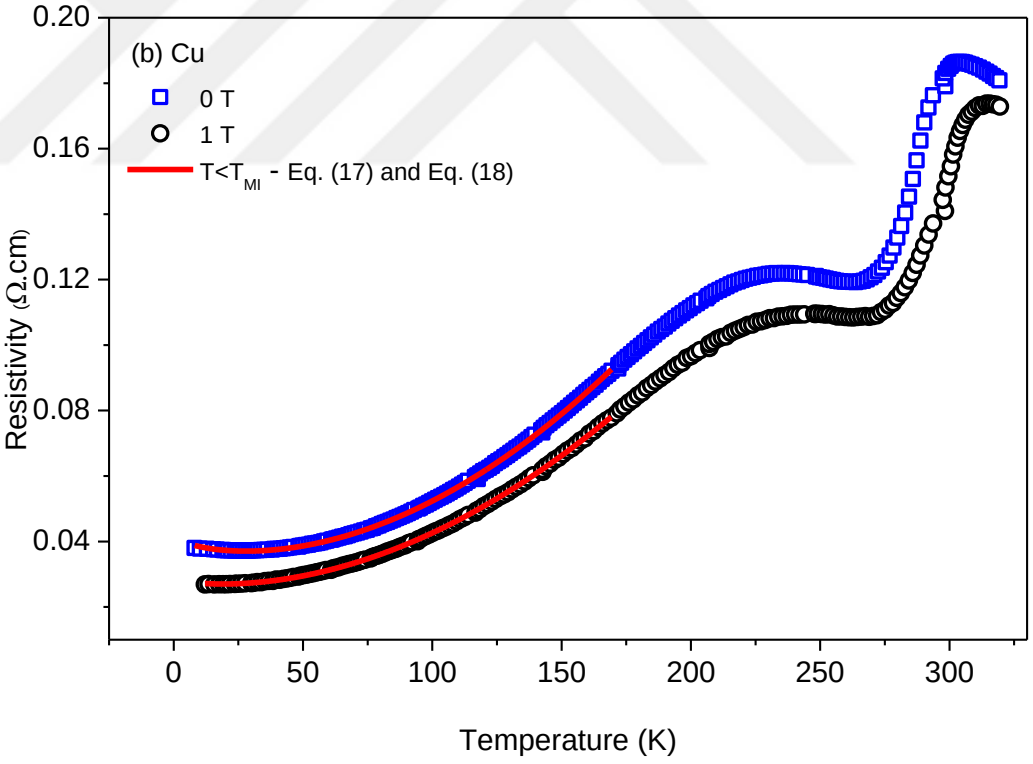
(b) Cu
0 T
1 T
T<T_MI - Eq. (17) and Eq. (18)
Resistivity (Ω.cm)
Temperature (K)
0.04
0.08
0.12
0.16
0.20
0
50
100
150
200
250
300

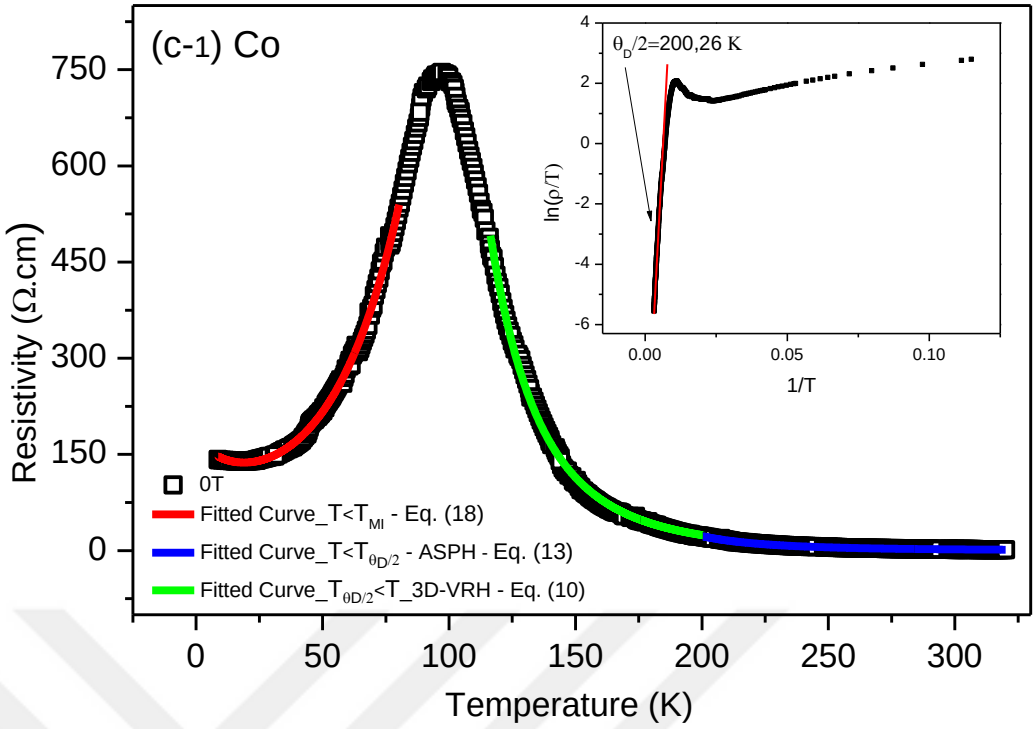
(c-1) Co
Resistivity (Ω.cm)
Temperature (K)
0T
Fitted Curve_T<T_MI - Eq. (18)
Fitted Curve_T<T_θD/2 - ASPH - Eq. (13)
Fitted Curve_T_θD/2<T_3D-VRH - Eq. (10)
θD/2=200,26 K
ln(ρ/T)
1/T

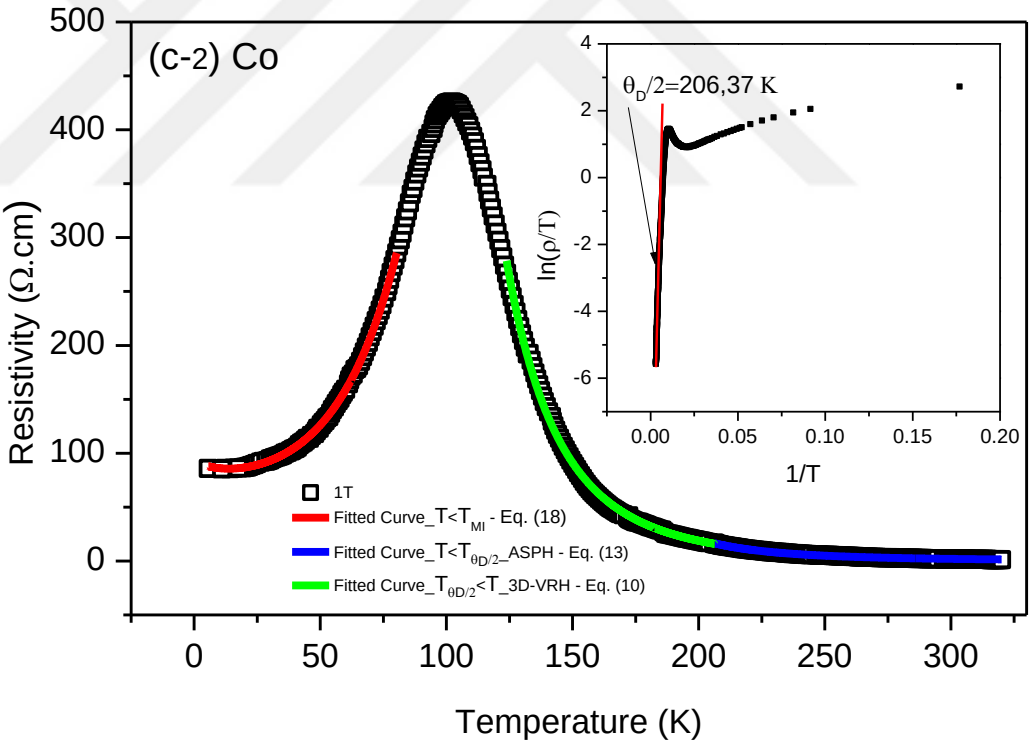
(c-2) Co
Resistivity (Ω.cm)
Temperature (K)
1T
Fitted Curve_T<T_MI - Eq. (18)
Fitted Curve_T<T_θD/2_ASPH - Eq. (13)
Fitted Curve_T_θD/2<T_3D-VRH - Eq. (10)
θD/2=206,37 K
ln(ρ/T)
1/T

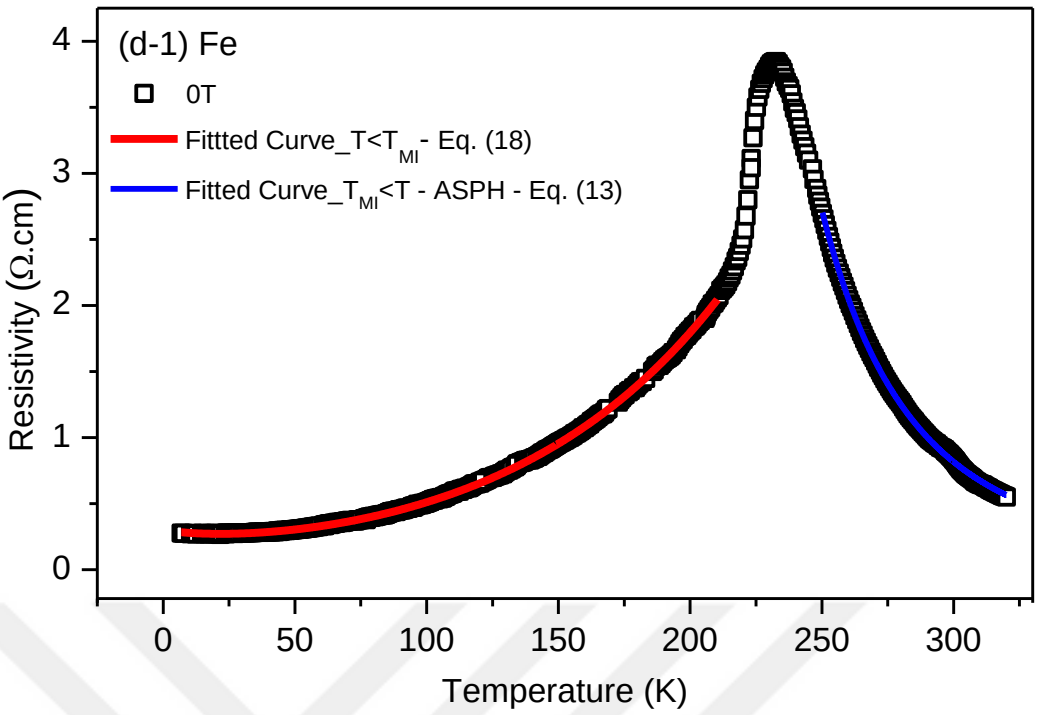
(d-1) Fe
0T
Fittted Curve_T<T_MI - Eq. (18)
Fitted Curve_T_MI<T - ASPH - Eq. (13)
Resistivity (Ω.cm)
Temperature (K)
0
1
2
3
4
0
50
100
150
200
250
300

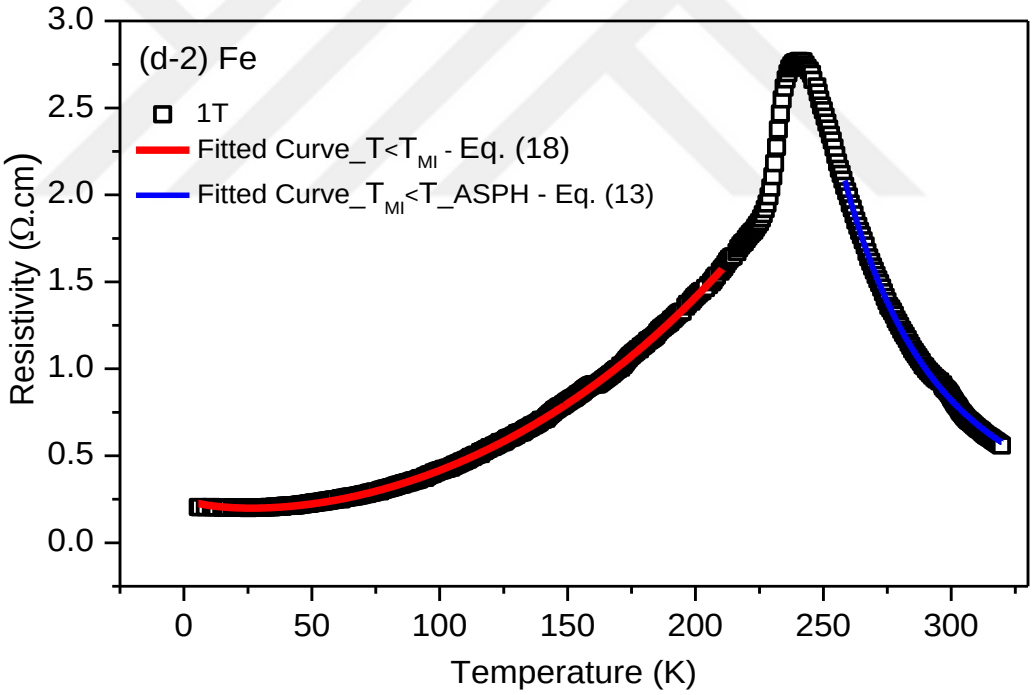
(d-2) Fe
1T
Fitted Curve_T<T_MI - Eq. (18)
Fitted Curve_T_MI<T_ASPH - Eq. (13)
Resistivity (Ω.cm)
Temperature (K)
0.0
0.5
1.0
1.5
2.0
2.5
3.0
0
50
100
150
200
250
300

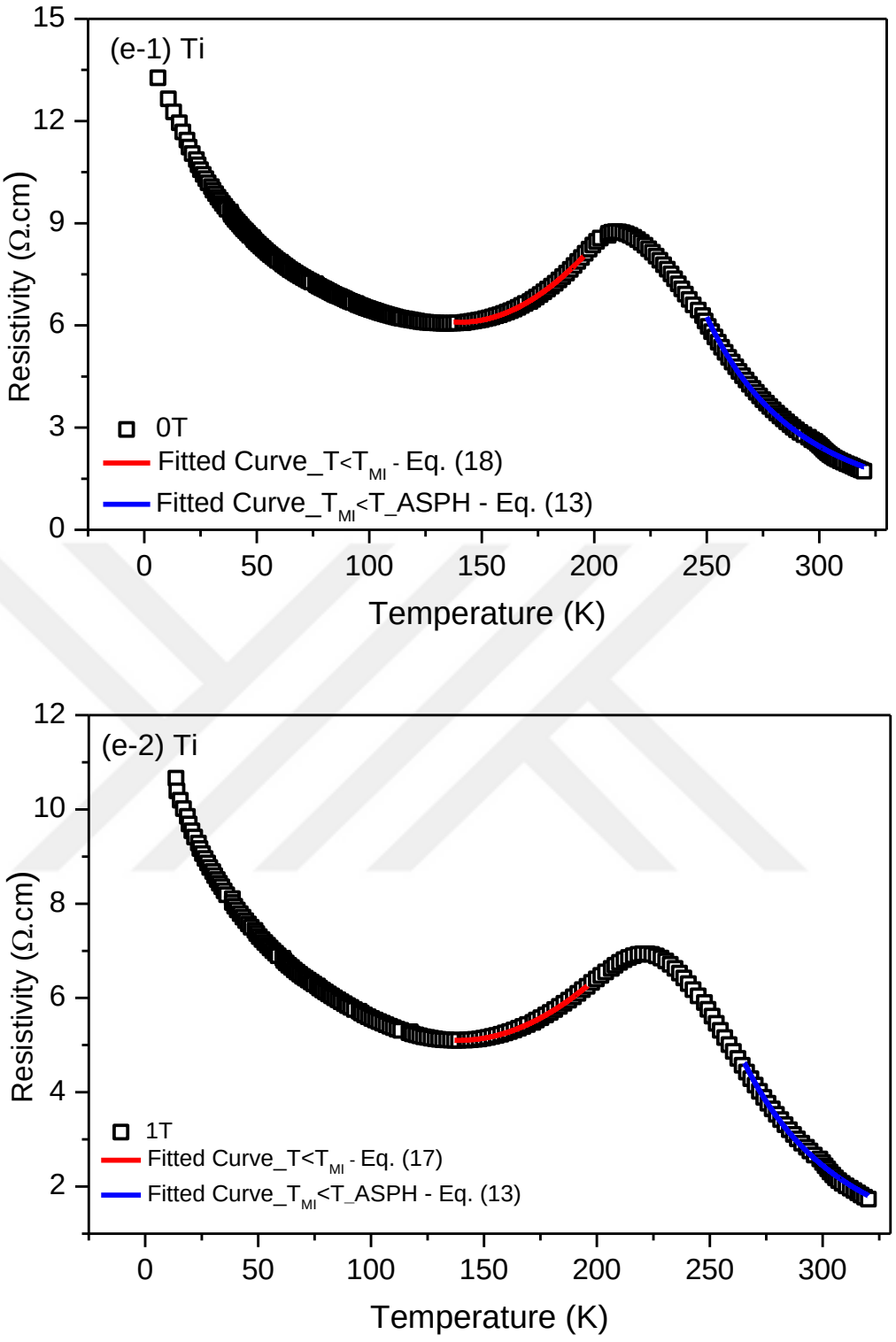

Figure 4.23. Temperature dependence of the electrical resistivity for $La_{0.8}Sr_{0.2}Mn_{1-x}B_xO_{3\pm\delta}$ compounds with *B:* ***(a) S 0*** *x=0.0,* ***(b) Cu*** *(x=0.1),* ***(c) Co*** *(x=0.1),* ***(d) Fe*** *(x=0.1) and* ***(e) Ti*** *(x=0.1).* The colorful lines indicate the best fit for theoretical models.

Table 4.4. Parameters used to fit the experimental data of $La_{0.8}Sr_{0.2}Mn_{1-x}B_xO_{3\pm\delta}$ compounds with *B:* ***(a) S 0*** *x=0.0,* ***(b) Cu*** *(x=0.1),* ***(c) Co*** *(x=0.1),* ***(d) Fe*** *(x=0.1) and* ***(e) Ti*** *(x=0.1)* for low *T (T<T_{MI})* using Eqs. (17) and (18).

$La_{0.8}Sr_{0.2}Mn_{1-x}B_xO_{3\pm\delta}$			
		0 T	**1 T**
S 0	ρ_0 *(Ω cm)*	0.3855	0.0289
	$\rho_{0.5}$ *(Ω cm* $K^{-0.5}$*)*	8.2086×10^{-5}	1.7481×10^{-5}
	ρ_2 *(Ω cm* K^{-2}*)*	1.5516×10^{-6}	1.5657×10^{-6}
	R^2	**0.999**	**0.999**
Cu	ρ_0 *(Ω cm)*	0.0426	0.0292
	$\rho_{0.5}$ *(Ω cm* $K^{-0.5}$*)*	14.100×10^{-4}	6.715×10^{-4}
	ρ_2 *(Ω cm* K^{-2}*)*	2.382×10^{-6}	2.012×10^{-6}
	R^2	**0.999**	**0.999**
Co	ρ_0 *(Ω cm)*	193.659	96.626
	$\rho_{0.5}$ *(Ω cm* $K^{-0.5}$*)*	17.213	3.928
	ρ_2 *(Ω cm* K^{-2}*)*	0.051	0.019
	ρ_5 *(Ω cm* K^{-5}*)*	5.052×10^{-8}	3.036×10^{-8}
	R^2	**0.997**	**0.999**
Fe	ρ_0 *(Ω cm)*	0.315	0.266
	$\rho_{0.5}$ *(Ω cm* $K^{-0.5}$*)*	0.122	0.017
	ρ_2 *(Ω cm* K^{-2}*)*	3.057×10^{-5}	3.207×10^{-5}
	ρ_5 *(Ω cm* K^{-5}*)*	1.351×10^{-12}	3.399×10^{-13}
	R^2	**0.999**	**0.999**
	ρ_0 *(Ω cm)*	32.997	19.759
Ti	$\rho_{0.5}$ *(Ω cm* $K^{-0.5}$*)*	3.026	1.657
	ρ_2 *(Ω cm* K^{-2}*)*	4.536×10^{-4}	2.528×10^{-4}
	R^2	**0.999**	**0.999**

Table 4.5. Parameters used to fit the experimental data of $La_{0.8}Sr_{0.2}Mn_{1-x}B_xO_{3\pm\delta}$ compounds with *B:* ***(a) S 0*** *x=0.0,* ***(b) Cu*** *(x=0.1),* ***(c) Co*** *(x=0.1),* ***(d) Fe*** *(x=0.1) and* ***(e) Ti*** *(x=0.1)* for high *T (T>T_{MI})* using Eqs. (10), (11) and (13).

$La_{0.8}Sr_{0.2}Mn_{1-x}B_xO_{3\pm\delta}$				
			0 T	**1 T**
Co	**ASPH**	$\theta_D/2$ *(K)*	200.26	206.37
		ρ_a *(Ω cm)*	2.191×10^{-5}	2.854×10^{-5}
		E_a *(meV)*	147.340	141.01
		R²	**0.998**	**0.997**
	3D-VRH	ρ_0 *(Ω cm)*	2.357×10^{-8}	1.199×10^{-8}
		T_0 *(K)*	3.710×10^{7}	4.020×10^{7}
		$N(E_F)$ *(eV^{-1} cm^{-3})*	1.967×10^{19}	1.816×10^{19}
		R²	**0.996**	**0.997**
Fe	**ASPH**	ρ_a *(Ω cm)*	2.661×10^{-6}	3.298×10^{-6}
		E_a *(meV)*	179.146	173.707
		R²	**0.999**	**0.998**
Ti	**ASPH**	ρ_a *(Ω cm)*	3.051×10^{-5}	2.416×10^{-5}
		E_a *(meV)*	144.533	150.481
		R²	**0.995**	**0.994**

4.2 Effect of Iron Substitution in *LSMO* System

In this part, the influence of iron content on the structural, microstructural, magnetic, and electrical-transport features of the ceramic perovskite manganites of the form $La_{0.8}Sr_{0.2}Mn_{1-x}Fe_xO_3$ (*x=0.0, 0.05, 0.1,* and *0.2)* was examined. Iron and manganese possess almost the same ionic radii (*0.645 Å* and *0.64 Å* for Fe^{3+} and Mn^{3+}, respectively). Therefore, there is no expected structural deformation in the system due to the doping *Fe* at *Mn* site. Moreover, iron ions are (non-Jahn-Teller) magnetic cations and they do not contribute to the double exchange *(DE)* interaction (37) (38) (44). One should note here that *CMR* in manganites are originated from the Jahn-Teller effects and *DE* interaction. Therefore, iron substitution at *Mn* site serve an interesting subject for the understanding *CMR* mechanism in *B*-site doped manganites. Along this line, in the current work, we systematically present the structural and magneto-electrical characterization of the manganite ceramics with $La_{0.8}Sr_{0.2}Mn_{1-x}Fe_xO_3$ (*x=0.0, 0.05, 0.1,* and *0.2*).

In particular, Ref. (40) has focused on electro-transport properties of the *LSMO* system with a tiny amount of iron substitution (up to *7%*). In this study, the magnetic properties are not explored deeply. On the other hand, a large amount of iron substitution (up to *70%*) in such systems have been performed in Ref. (43)

demonstrating insulating behavior. Refs. (186) (38) primarily focus on the hole-doped manganites $La_{1-x}Ca_xMn_{1-y}Fe_yO_3$ (with $x=0.25$ and 0.30) and investigate the role of iron doping on the magnetic and electrical features. The replacement of Fe^{3+} ions with Mn^{3+} ions are found not to participate any kind of ferromagnetic interaction in the Fe^{3+}–Mn^{4+} double exchange.

4.2.1 X-Ray Diffraction *(XRD)* Refinement Analyses

Phase characterization and structural analysis were performed by *X*-ray diffraction *(XRD)* technique with CuK_α radiation at different temperatures to decide the most ideal temperature and find the qualified phase. As seen in Fig. 4.24, it was observed that the final temperature was determined at *1250 ºC* because of obtaining an excellent perovskite structure. And, no unreacted peaks (such as Mn_3O_4) were observed.

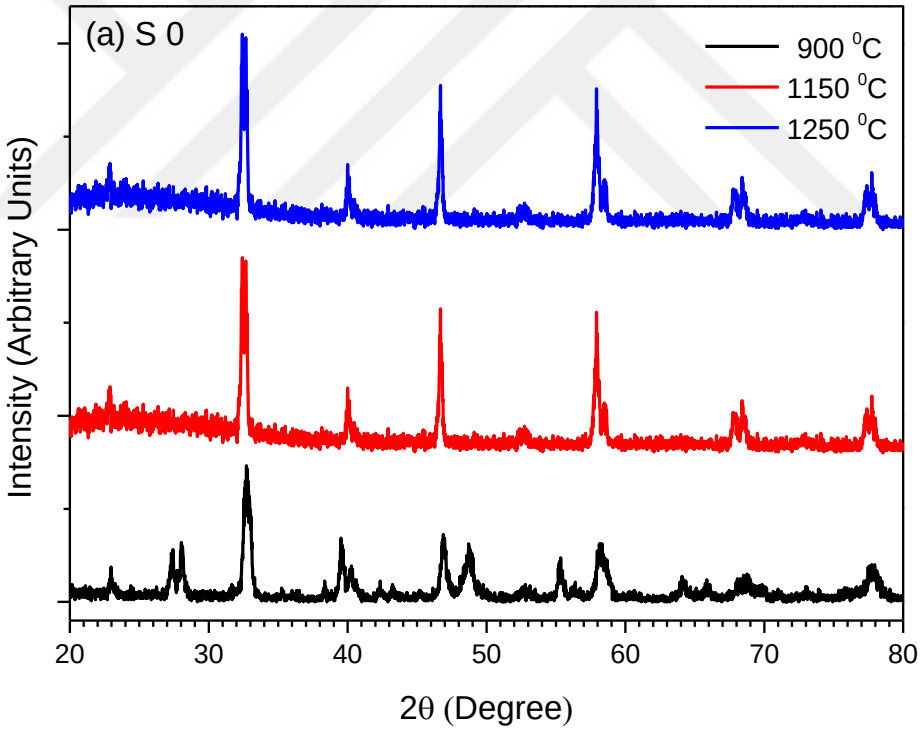

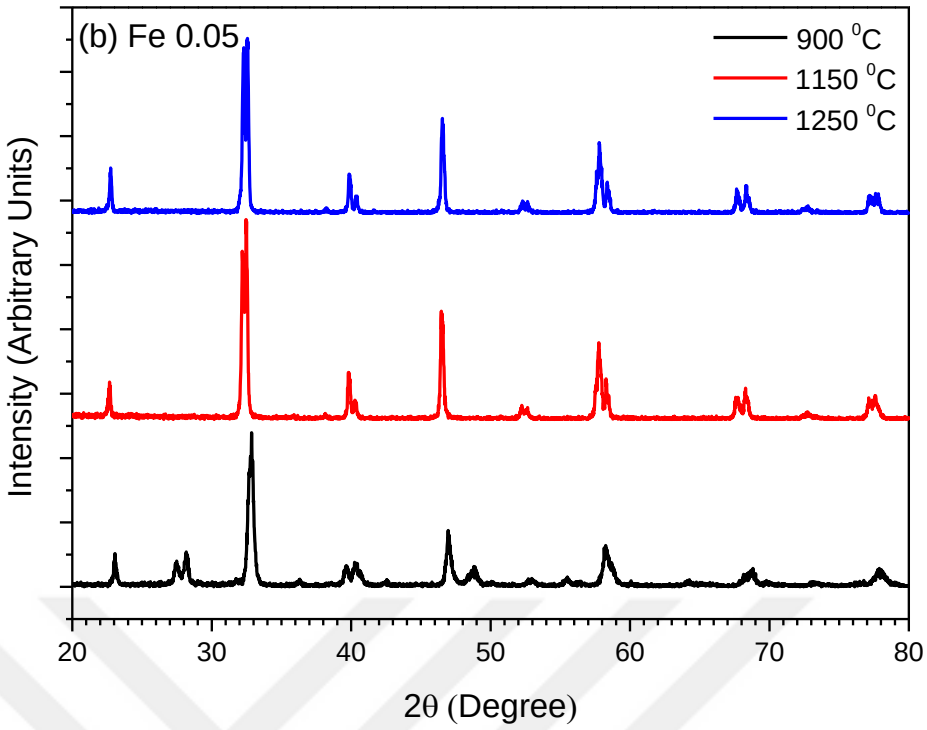
(b) Fe 0.05
900 °C
1150 °C
1250 °C
Intensity (Arbitrary Units)
20
30
40
50
60
70
80
2θ (Degree)

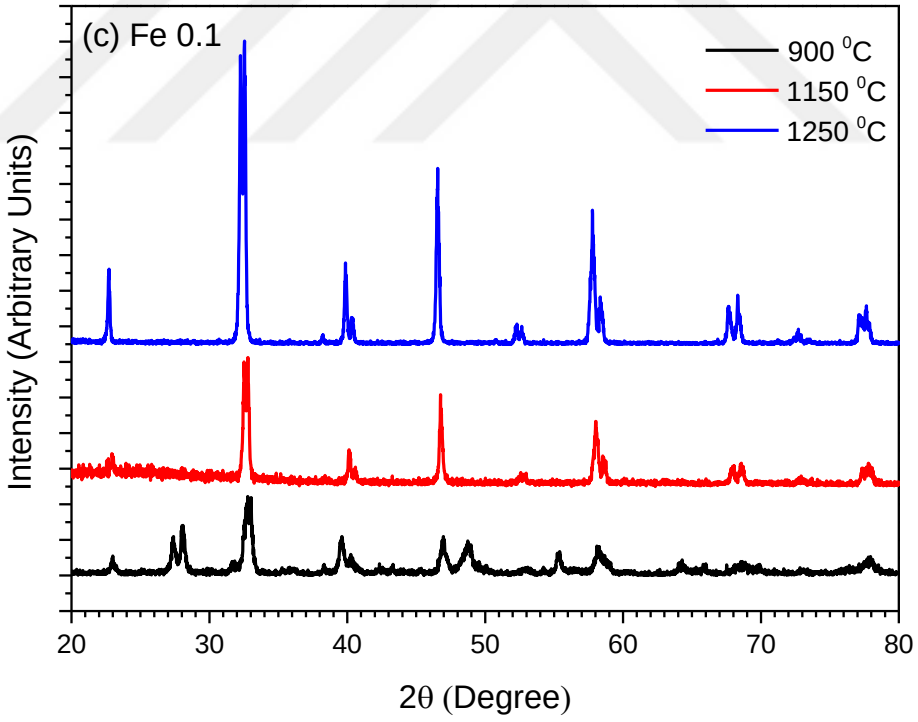
(c) Fe 0.1
900 °C
1150 °C
1250 °C
Intensity (Arbitrary Units)
20
30
40
50
60
70
80
2θ (Degree)

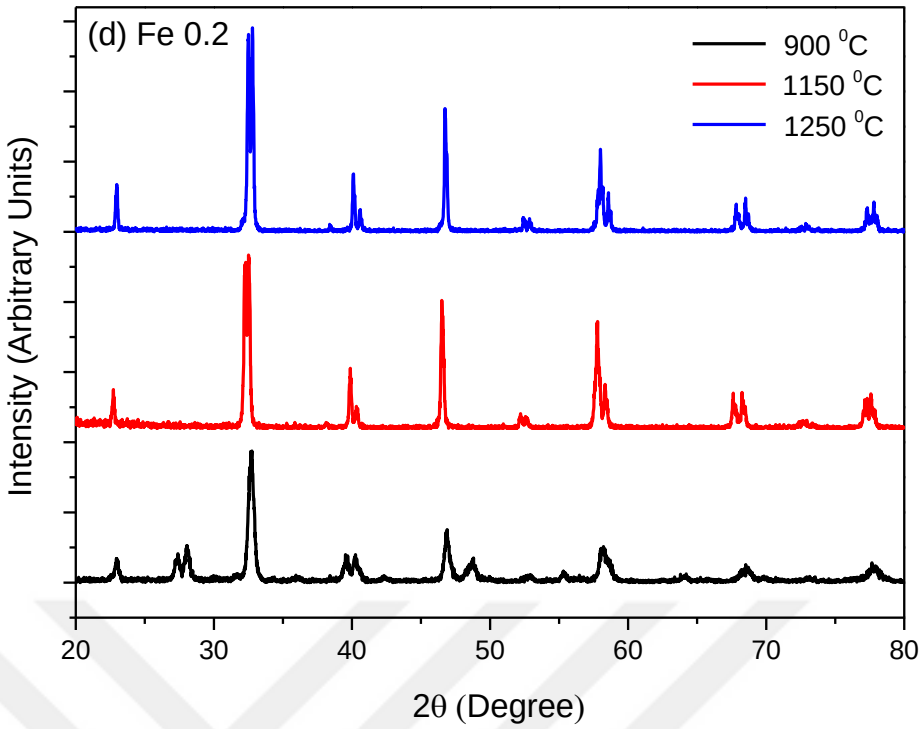

Figure 4.24. *X*-ray diffraction pattern for $La_{0.8}Sr_{0.2}Mn_{1-x}Fe_xO_3$ compounds with ***(a) S 0*** *x=0,00* ***(b)*** *x=0.05,* ***(c)*** *x=0.10* and ***(d)*** *x=0.20* after each annealing process.

The phase purity and crystal structure of the samples were researched by using *X*-ray diffraction *(XRD)* technique with CuK_α radiation at room temperature. Fig. 4.24 shows the experimental data obtained with the powder *XRD* measurements for all samples. We also make a zoom-in of the strongest diffraction peak - $(2\bar{1}0)$ and (104) planes - for higher visibility which is shown in the inset of the same figure. From the figure, it is found that the ceramic samples have a single phase without impurities in each sample that has been substituted with iron which shows that there is no structural transition in the entire sample made with substitution. In other words, no secondary phases corresponding to unreacted ***Fe***, any oxide of ***Fe,*** or manganese dioxide were detected from the *XRD*. The change in the cell volume can be also directly seen from the *XRD* spectra by checking the shift of the diffraction peaks (see insets of Fig. 4.25). The shift in the lower angles at the strongest peak with the ***Fe*** amount is an indication of the increase in the structural parameters (103).

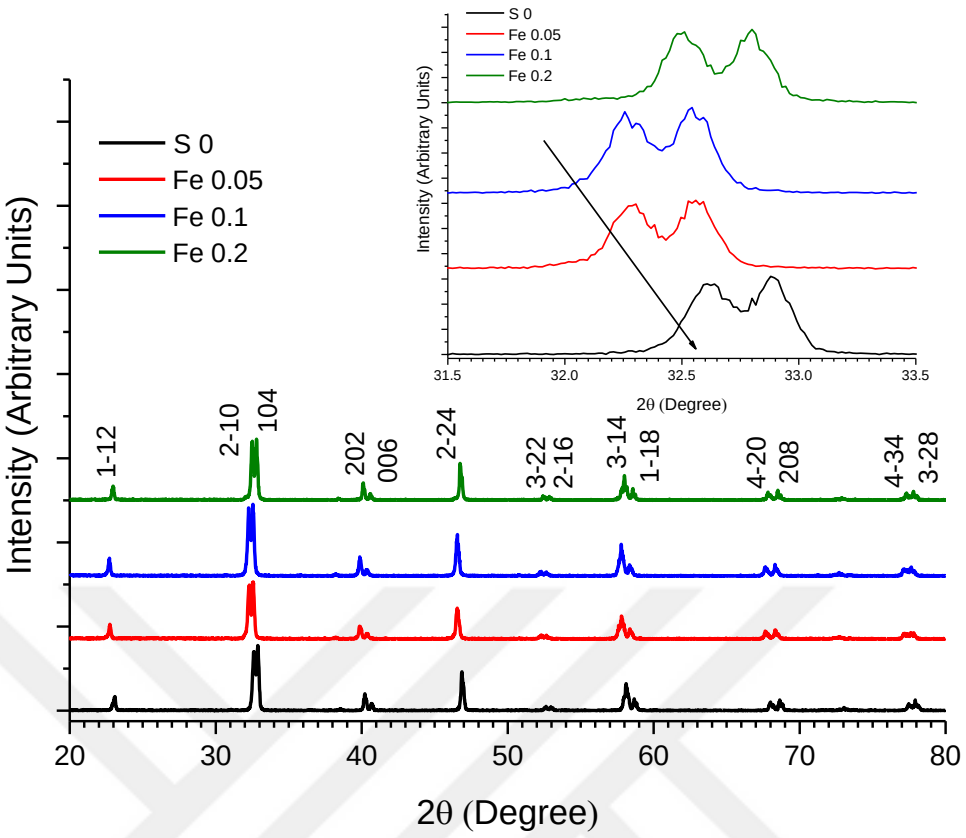

Figure 4.25. X-ray powder diffraction patterns for $La_{0.8}Sr_{0.2}Mn_{1-x}Fe_xO_3$ with *x=0.0, 0.05, 0.1,* and 0.2 samples. The inset shows the magnified spectrum of the strongest diffraction peak which shifts with variation in the ***Fe*** content.

The results of the powder *XRD* data were also fitted by the Jana refinement method using Jana 2006 program (25) to obtain the lattice parameters which is shown in Fig. 4.26. The refinement analysis confirmed the single-phase nature of the perovskite structure which is indexed in a rhombohedral-distorted structure with $(R\bar{3}c)$ space group for all ceramic samples (13, 36). The unit-cell parameters and refinement quality factors are tabulated in Table 4.6. The result of the refinement indicates that the experimental data and the calculated one match quite well, and all obtained peaks have been suitably indexed. This result confirms that both the pristine *LSMO* and iron substituted samples are monophasic and have been successfully synthesized. All refinement quality factors *(Rp, W_{RP},* and *GOF*) were used as a numerical standard for the quality of the refinement of experimental and fitted diffraction data. From the data obtained with the refinement, it is found that the lattice parameters ($a = b$, and c) and unit cell volume increase with the increase in iron content. Similar structural changes with

Fe substitution were also reported earlier (187). The lattice parameters were varied with substitution because of the B-site ionic radius *(<r_B>)* mismatch between the ***Fe*** and *Mn* ions. Many works reported that the charge concentration of ***Fe*** ions can be in the high-spin Fe^{2+}, high-spin Fe^{3+}, and Fe^{4+} states (40) (188) (41). The *B*-site cations for 6 coordination number, Fe^{4+} *((<r_{Fe4+}>=0.585 Å)* is larger than Mn^{4+} *(((<r_{Mn4+}>=0.53 Å).* The high spin state ionic radius of Fe^{3+} *((<r_{Fe3+}>=0.645 Å)* is the same with Mn^{3+} *((<r_{Mn3+}>=0.645 Å)* and larger than Mn^{4+}. Also, Fe^{2+} *((<r_{Fe2+}>=0.78 Å)* is larger than both Mn^{3+} and Mn^{4+} (103). Moreover, for the charge neutrality, one may conclude that Fe^{4+} ions substitute Mn^{4+} ions and Fe^{3+} ions substitute Mn^{3+} ions. For our case, the ionic state of Fe^{4+} is thought to be dominant in the perovskite ceramics and the overall iron substitution causes a change in the relative cation fractions of the mixed-valence states of the manganese ions, which causes an increase the number of Mn^{4+} cations whereby the structural parameters on the nature of unit cell volume increase. The unit cell volume increase can be also justified from the diffraction peaks in the inset of Fig.4.25. The shift in the lower 2θ values at the strongest peak with the Fe amount is an indication of the increase in the structural parameters (189).

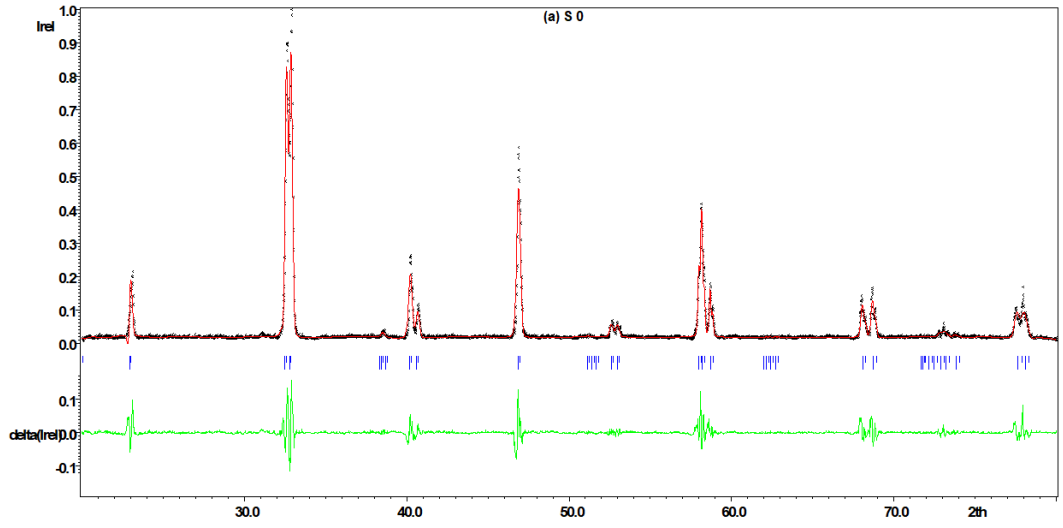

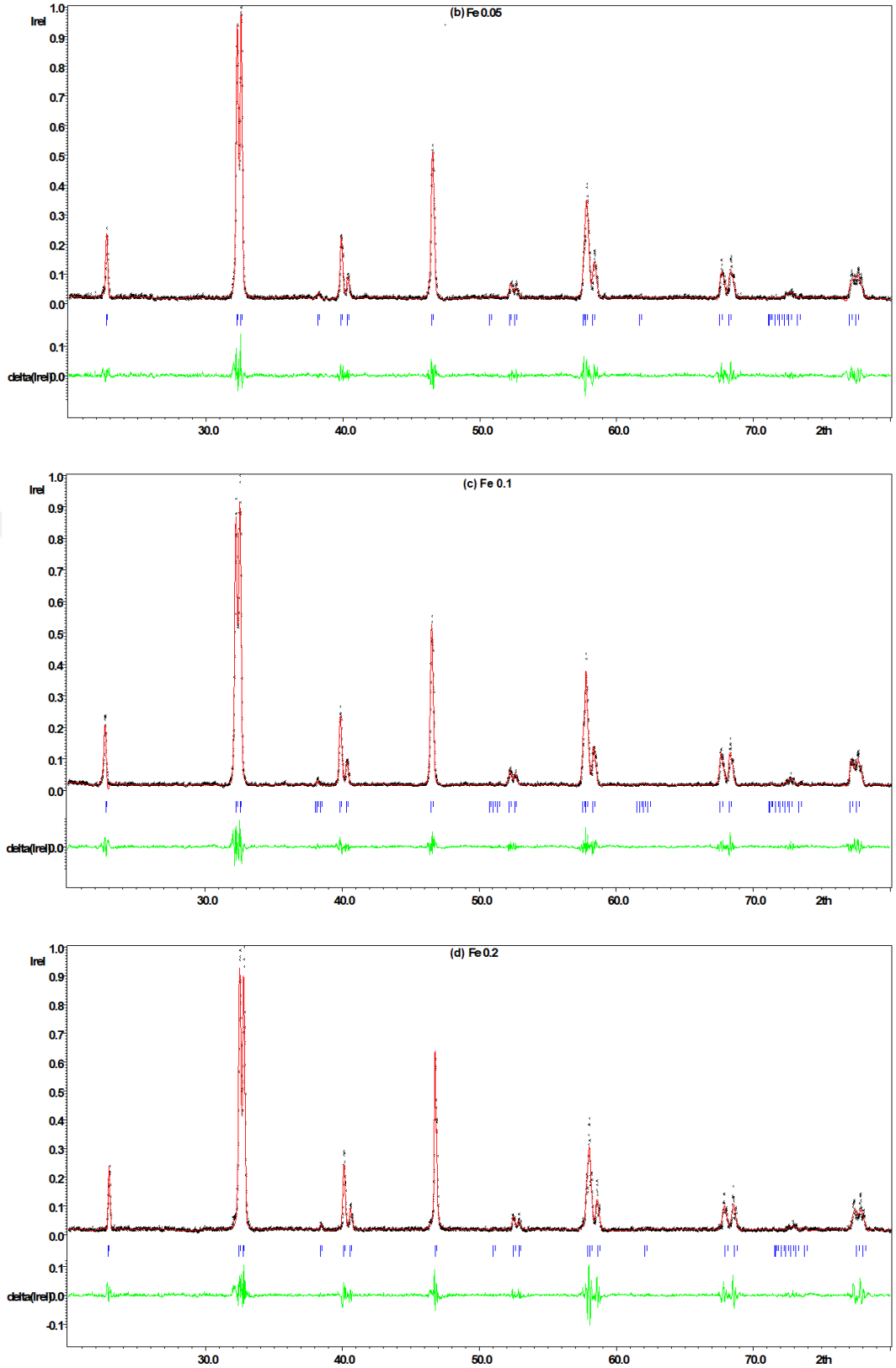

Figure 4.26. Results of Jana refinement of powder *XRD* spectra of $La_{0.8}Sr_{0.2}Mn_{1-x}Fe_xO_3$ compounds with ***(a) S 0*** *x=0,00* ***(b)*** *x=0.05*, ***(c)*** *x=0.10* and ***(d)*** *x=0.20* at room temperature. Black cross lines correspond to experimental data and the red solid lines are calculated fits. Blue vertical bars represent the Bragg reflections for

the space group *($R\bar{3}c$).* The difference pattern between the experimental and calculated data is shown at the bottom with the green line.

Furthermore, Debby Sherer equation is used to calculate the average crystal size. It is given below (169);

$$d_{max} = \frac{0.9\lambda}{\beta \cos\theta} \tag{22}$$

where *D* is the crystallites size (nm), λ is the wavelength (nm), β is the full width at half maxima *(FWHM)* and θ is the Bragg's diffraction angle. The calculated values of d_{max} for all samples are given in Table 4.7.

Table 4.6. The structural parameters of for $La_{0.8}Sr_{0.2}Mn_{1-x}Fe_xO_3$ compounds with ***(a) S 0*** *x=0,00* ***(b)*** *x=0.05,* ***(c)*** *x=0.10* and ***(d)*** *x=0.20*.

Sample	**S 0**	**Fe 0.05**	**Fe 0.1**	**Fe 0.2**
Space group	**R-3c**	**R-3c**	**R-3c**	**R-3c**
a (Å)	5.503	5.540	5.544	5.513
c (Å)	13.318	13.398	13.409	13.329
V (Å)^3	349.360	356.190	356.972	350.870
GOF	**0.93**	**0.61**	**0.72**	**0.82**
Rp	12.92	8.14	10.72	11.98
W_{RP}	17.89	11.12	14.47	16.51
D (nm)	33.68	41.18	37.60	39.51
Grain Size (μm)	2.45	2.77	3.27	4.24

4.2.2 Scanning Electron Microscopy *(SEM)* Analyses

The experimental data obtained with the use of scanning electron microscopy images for ***S 0, Fe 0.05, Fe 0.1*** and ***Fe 0.2*** are presented in Fig. 4.27, 4.29, 4.31 and 4.33, respectively at the same magnification *(x3000).* All micrographs represent the typical results of the perovskite ceramics. Histograms of each *SEM* micrographs display the size distribution of the particles which are shown in the insets. The microscopic images obviously show that all the manganite samples are formed of polycrystalline microstructure and most of the grains are almost spherical in shape with non-uniform size distribution. The

average particle size of the ceramic samples is obtained by using Gaussian fitting method (170) which increases from *2.45 μm* for pristine sample to *4.24 μm* for *20 %* iron substituted sample. The particle size distribution graphs of ***S 0, Fe 0.05, Fe 0.1*** and ***Fe 0.2*** are given in Fig. 4.28, 4.30, 4.32 and 4.34, respectively. In general case, the Fe^{4+} ions are larger than the Mn^{4+} ions. Hence, this can result to lattice expansion as the ***Fe*** content.

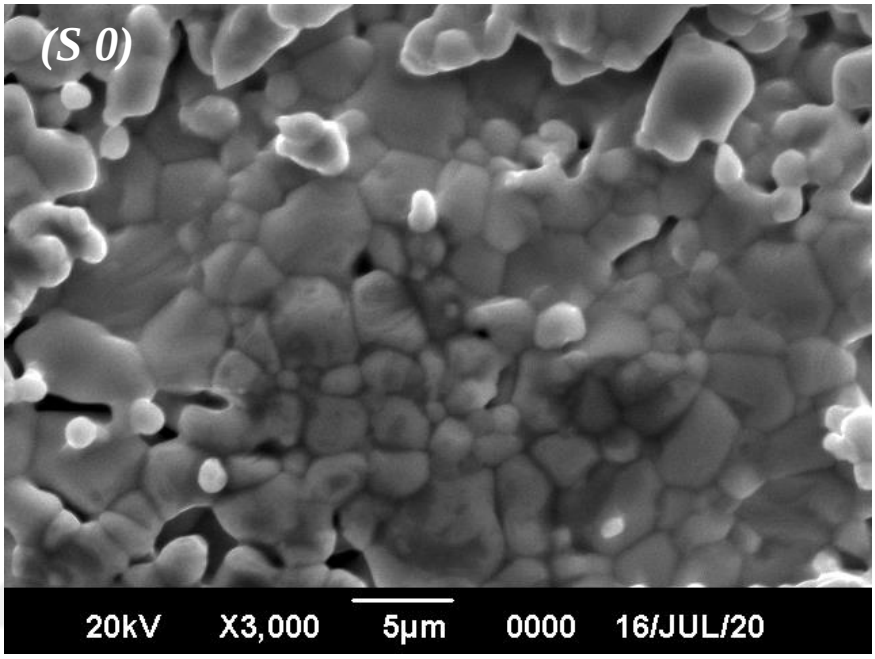

Figure 4.27. *SEM* view of the $La_{0.8}Sr_{0.2}MnO_3$.

As for particle size distribution graphs according to the *SEM* images;

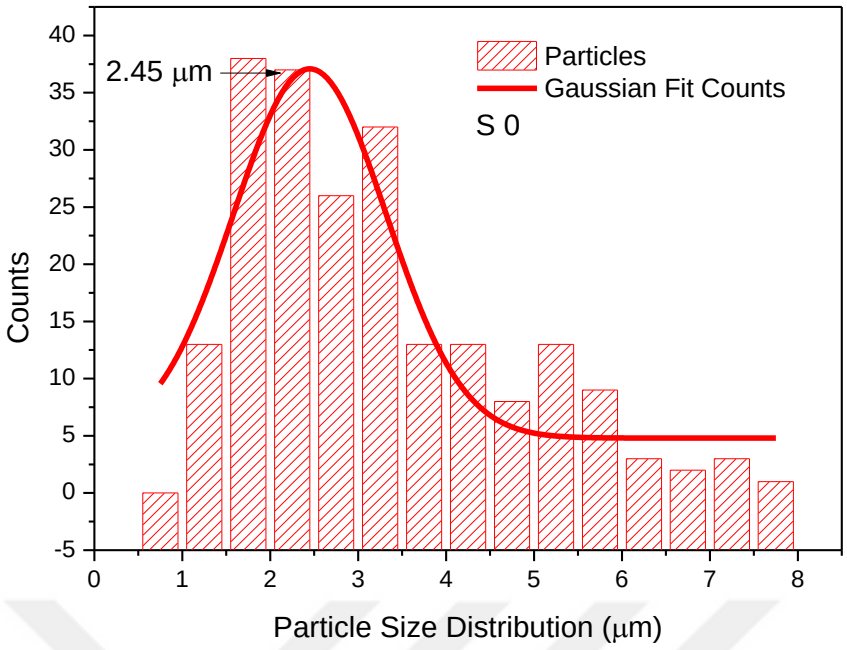

Figure 4.28. Average particle size distribution graph of the $La_{0.8}Sr_{0.2}MnO_3$.

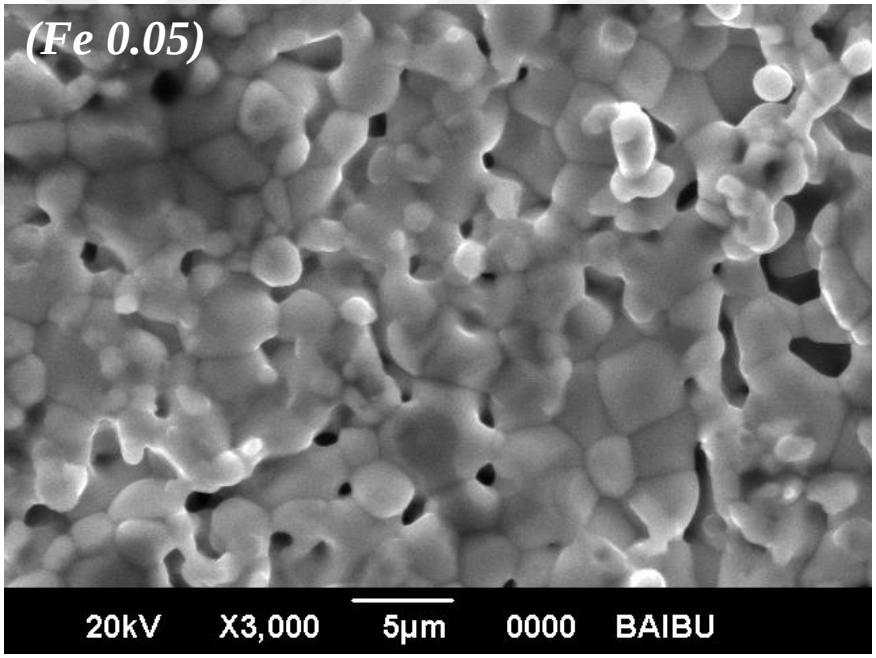

Figure 4.29. *SEM* view of the $La_{0.8}Sr_{0.2}Mn_{0.9}Fe_{0.05}O_3$

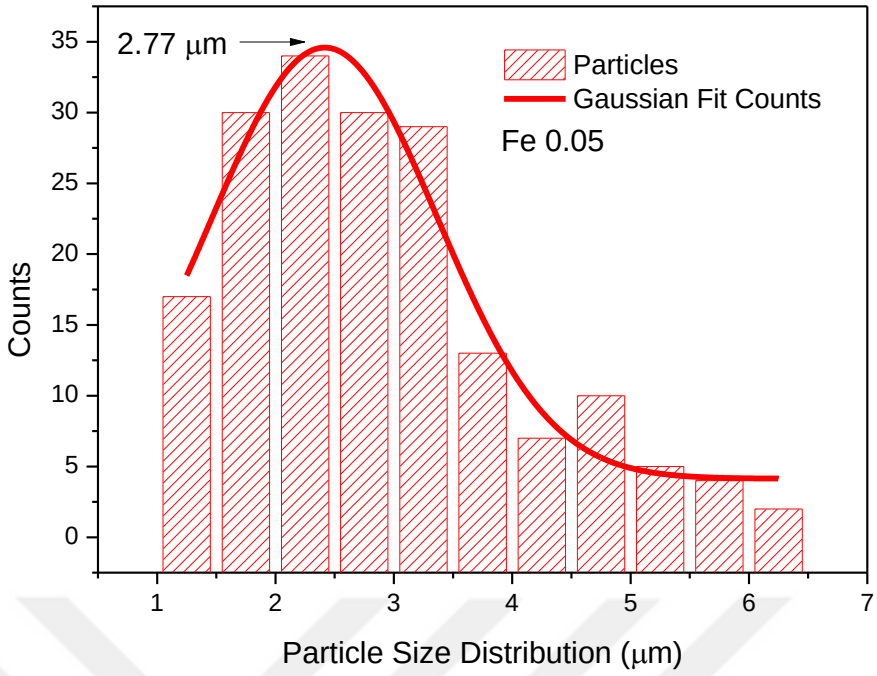

Figure 4.30. Average particle size distribution graph of the $La_{0.8}Sr_{0.2}Mn_{0.9}Fe_{0.05}O_3$.

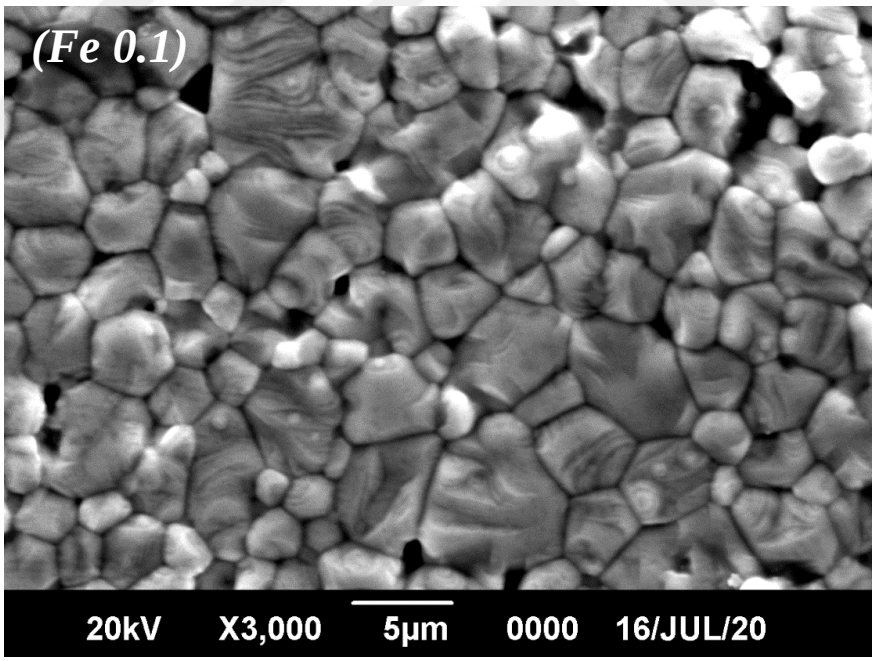

Figure 4.31. *SEM* view of the $La_{0.8}Sr_{0.2}Mn_{0.9}Fe_{0.1}O_3$

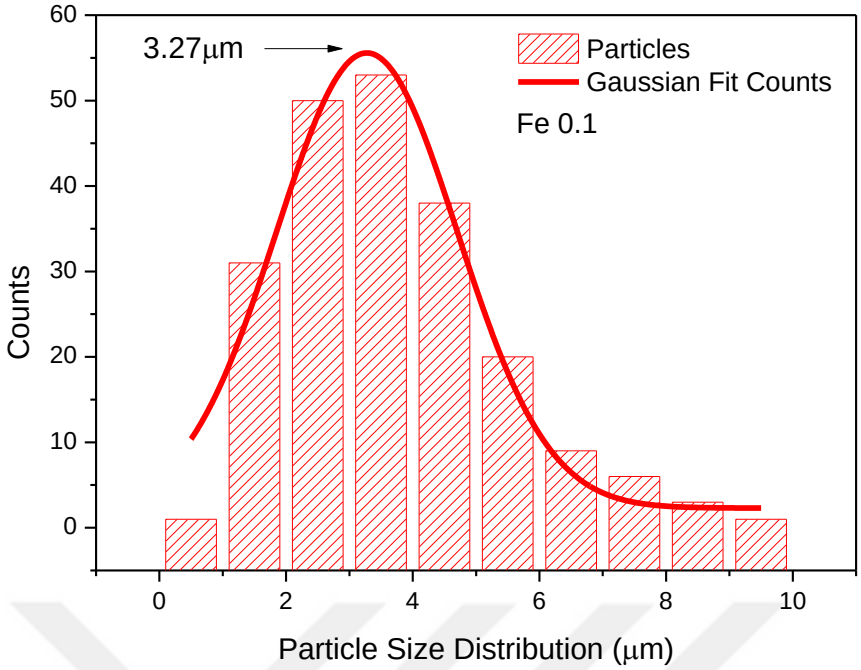

Figure 4.32. Average particle size distribution graph of the $La_{0.8}Sr_{0.2}Mn_{0.9}Fe_{0.1}O_3$.

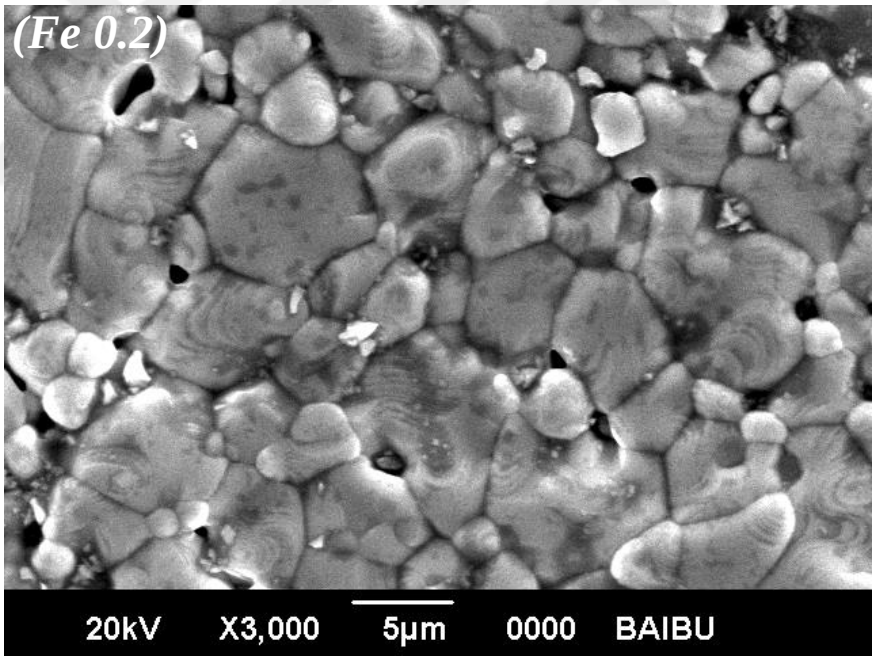

Figure 4.33. *SEM* view of the $La_{0.8}Sr_{0.2}Mn_{0.9}Fe_{0.2}O_3$

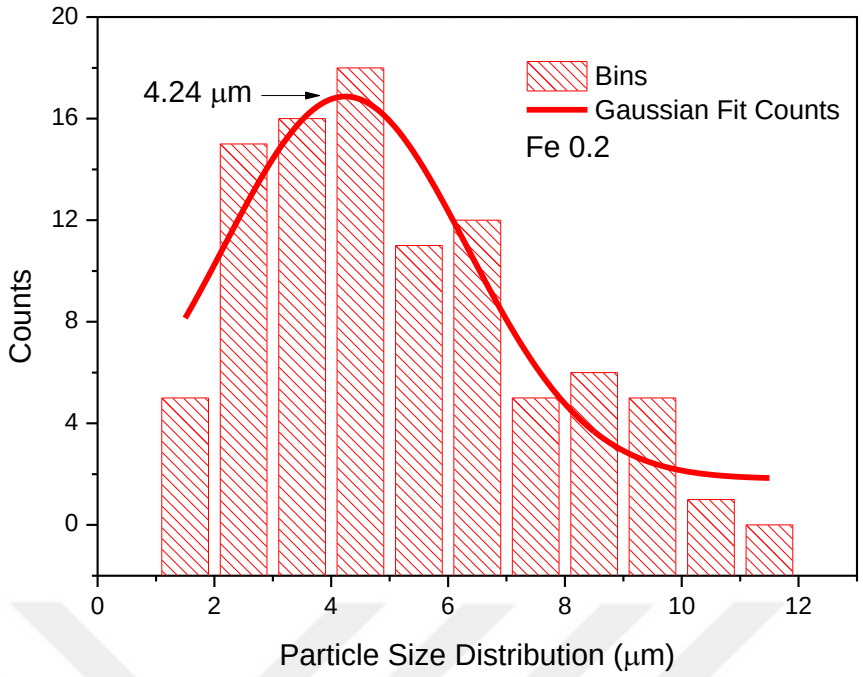

Figure 4.34. Average particle size distribution graph of the $La_{0.8}Sr_{0.2}Mn_{0.9}Fe_{0.2}O_3$.

4.2.3 Electron Dispersive X-Ray *(EDX)* Analyses

The *SEM* images were accompanied by an electron dispersive X-ray *(EDX)* system that was applied for elemental analysis to provide the elemental composition of the perovskite samples (190). *EDX* analysis signified the presence of considered elements an active perovskite layer. The overall chemical homogeneity of the prepared sample was determined by *EDX*. And, the *EDX* results of compounds confirmed the presence of *La, Sr, Fe, Mn* and *O* elements in the compound. It was seen that there was no undesirable peak. This showed us that the material was prepared homogeneously (191).

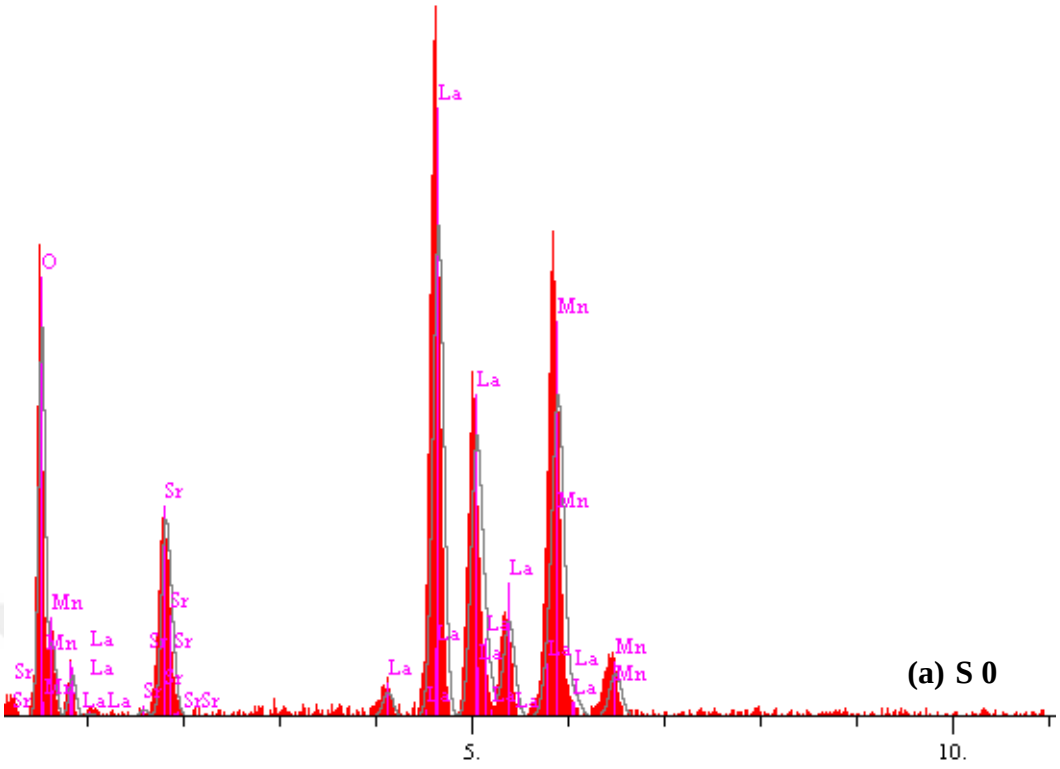

(a) S 0

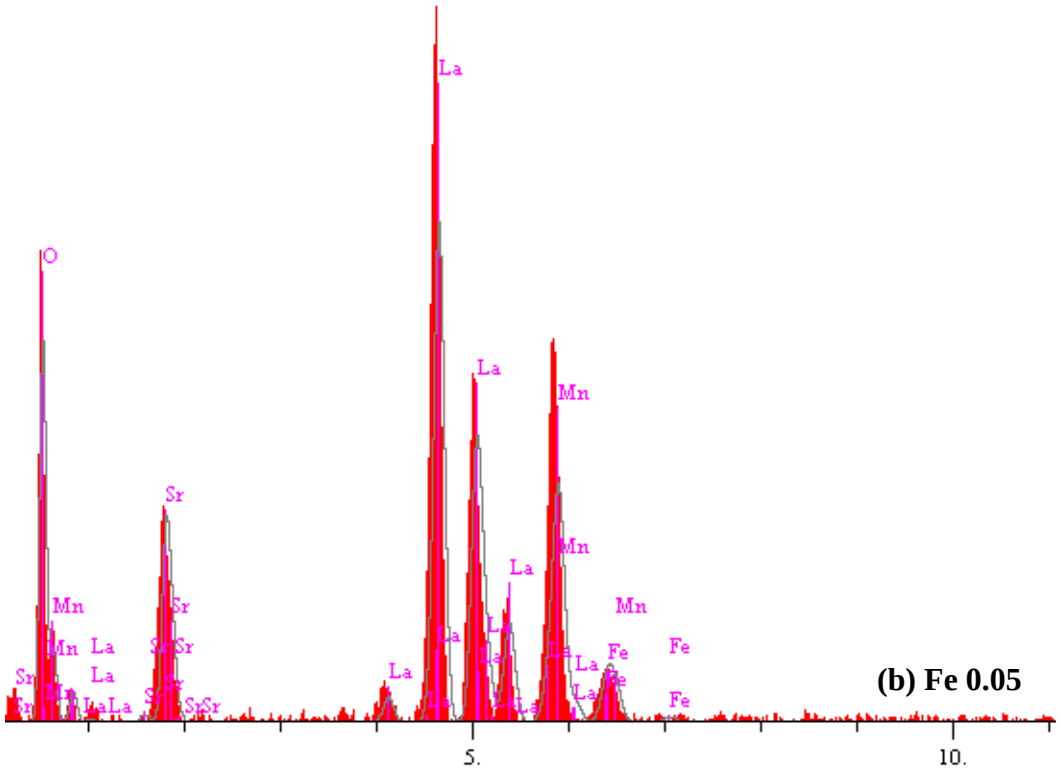

(b) Fe 0.05

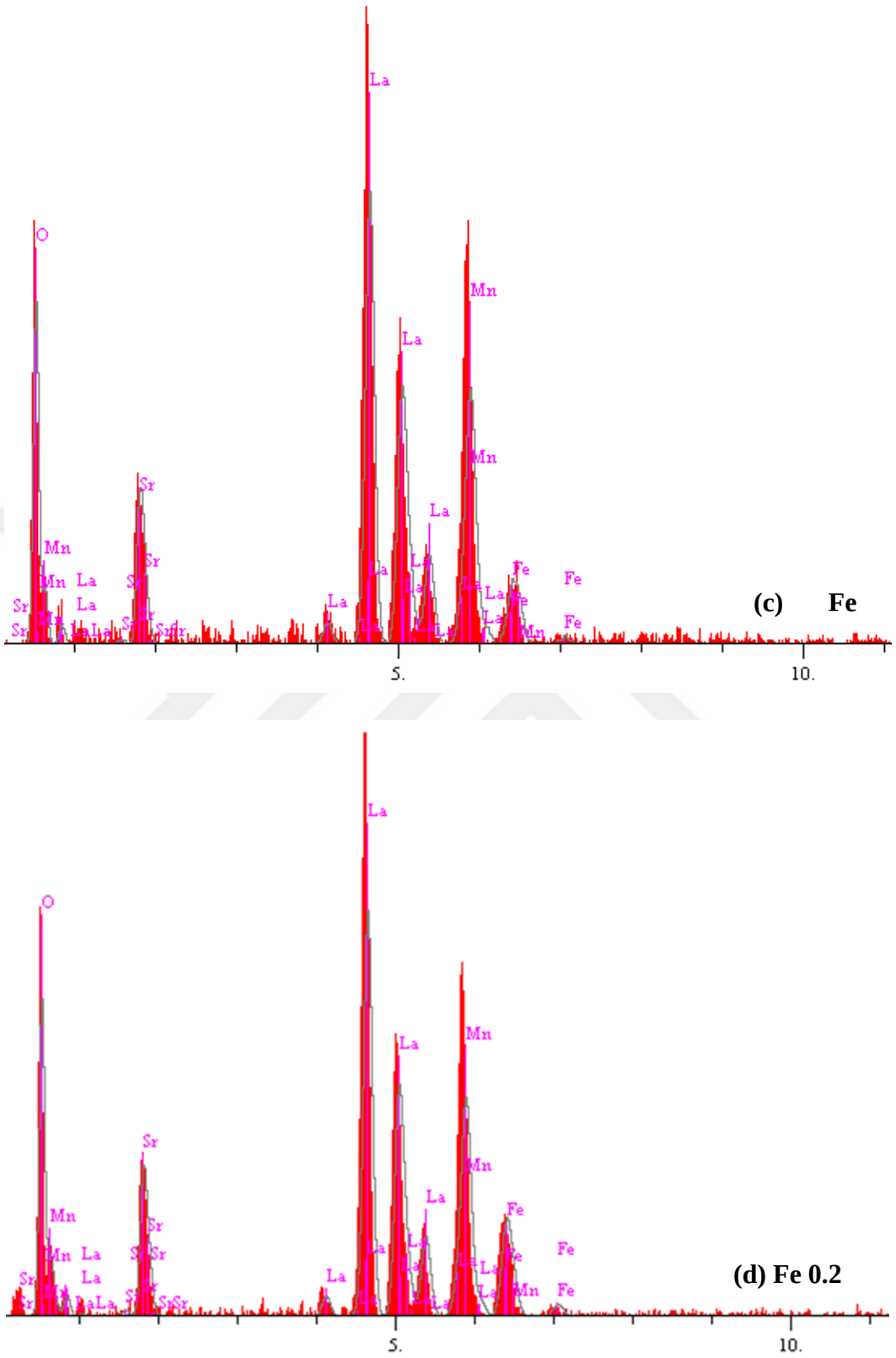

Figure 4.35. *EDX* image of distribution of the elements for $La_{0.8}Sr_{0.2}Mn_{1-x}Fe_xO_3$ compounds with ***(a) S 0*** *x=0,00* ***(b)*** *x=0.05,* ***(c)*** *x=0.10* and ***(d)*** *x=0.20.*

Table 4.7. Concentrations of the elements in $La_{0.8}Sr_{0.2}Mn_{1-x}Fe_xO_3$ compounds with ***(a) S 0*** *x=0,00* ***(b)*** *x=0.05*, ***(c)*** *x=0.10* and ***(d)*** *x=0.20.*

		Concentration (wt.%)			
Element	**Line**	**B_x: S 0**	**Fe 0.05**	**Fe 0.1**	**Fe 0.2**
O	K_α	20.945	20.526	20.259	20.406
Mn	K_α	13.241	9.700	11.644	10.793
B_x	K_α	0	2.004	2.629	4.928
Sr	L_α	11.651	12.044	10.323	10.754
La	L_α	54.163	55.726	55.145	53.120
Total		**100**	**100**	**100**	**100**

4.2.4 Magneto-Transport Features

In Fig. 4.36, the magnetization versus temperature plot for all samples is shown which has been undertaken by an applied magnetic field of *150 Oe* in the field-cooled *(FC)* mode. Samples with *x=0.0, 0.05*, and *0.1* exhibits a clear transition from ferromagnetic to paramagnetic state with increasing temperature. There are no detected anomalies that are attributed to impurity. This is also confirmed by *XRD* measurement analysis as mentioned in the structural features. The magnetic transition temperature, i.e., Curie temperature T_C, has been obtained by differentiating the temperature-dependent magnetization curves and corresponds to minimum temperature in the *dM/dT - T* plots (insets of Fig. 4.36). Corresponding T_C values as well as the transition widths ΔT_C, which are the value of the full width at half maximum of the *dM/dT* peaks, are listed in Table 4.8. It is clearly seen from the table that the iron substitution leads to a decrease both in the system magnetization and in the Curie temperature. This feature is also in agreement with the studies reported previously on *B*-site substitution of ***Fe*** (78) (12). The ratio of Mn^{3+}/Mn^{4+} change with replacing of Mn^{3+} with Fe^{3+}. Likewise, replacing the network of $Mn^{4+}–O^{2-}Mn^{3+}$ with $Mn^{4+}–O^{2}–Fe^{3+}$ leads the mechanism of the charge transfer become disordered (192). As a result, the *FM* interaction is weakened and the Mn^{4+}-O-Mn^{3+} bond angle is reduced, thus, the *DE* interaction is suppressed.

Table 4.8. Experimental parameters determined from *M(T)* and *ρ(T)* data for the samples of $La_{0.8}Sr_{0.2}Mn_{1-x}Fe_xO_3$ with ***(a) S 0*** *x=0,00* ***(b)*** *x=0.05*, and ***(c)*** *x=0.10*. All the parameters are explained in the text.

Parameters	**S0**	**Fe 0.05**	**Fe 0.1**
T_{MI}(K)	338	280	233
T_C (K)	327	320	279
ΔT_C	7.06	5.90	8.97
MR %	14.96	21.75	48.11
TCR %	2.16	1.55	8.23

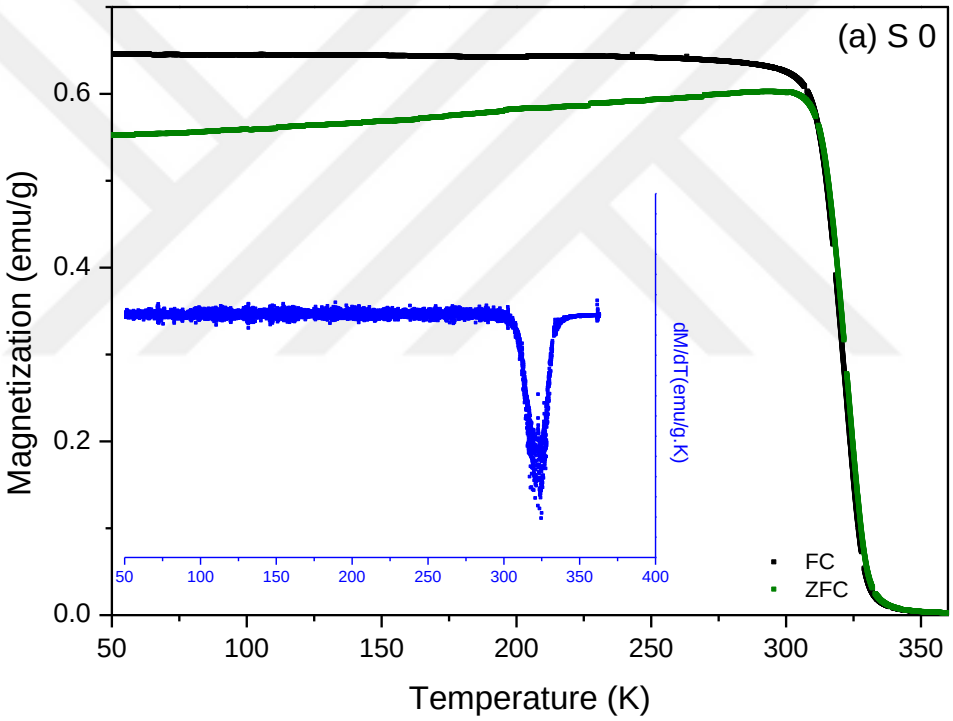

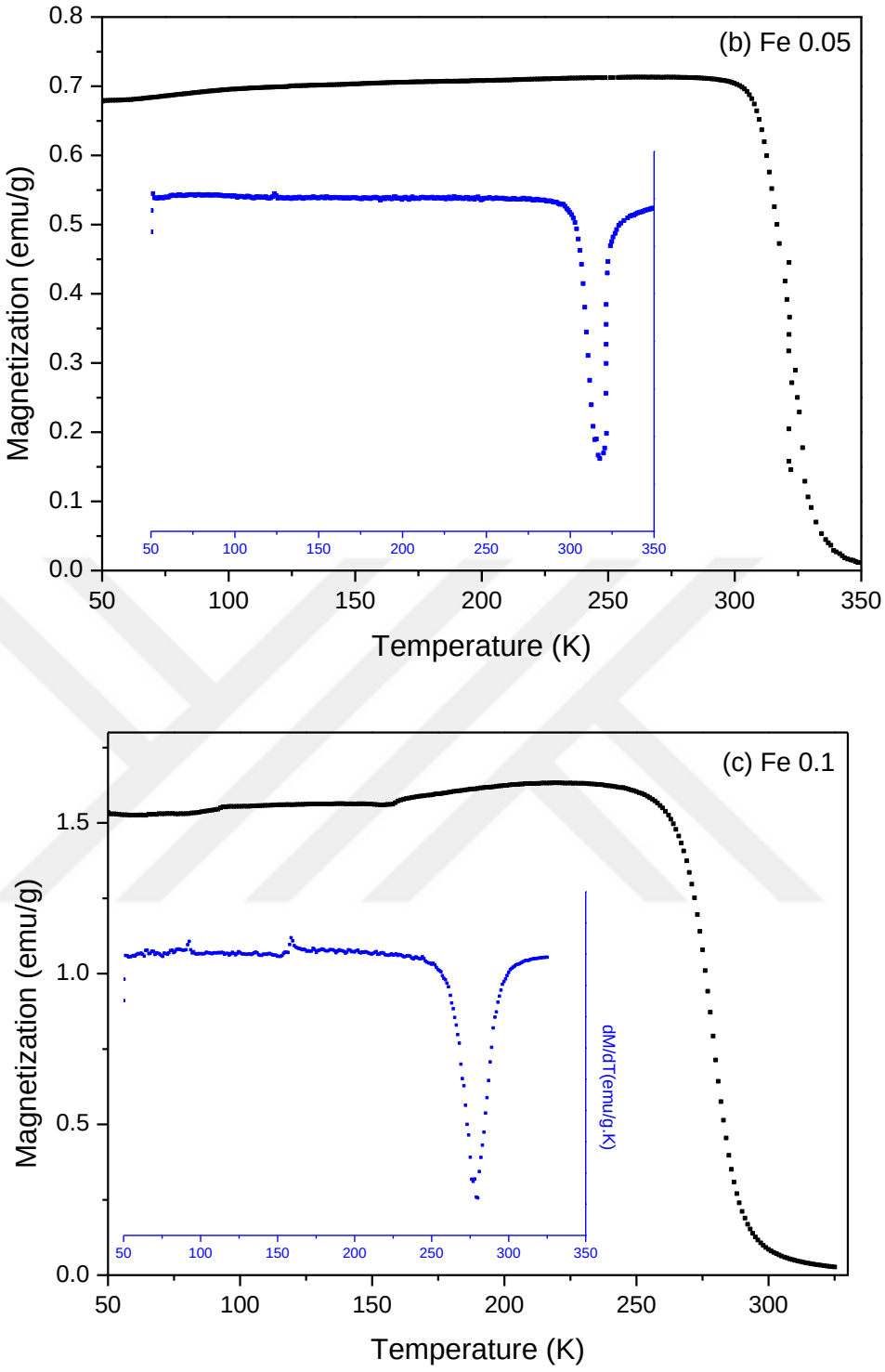

Figure 4.36. Temperature variation of magnetization for $La_{0.8}Sr_{0.2}Mn_{1-x}Fe_xO_3$ compounds with ***(a) S 0*** *x=0,00* ***(b)*** *x=0.05* and ***(c)*** *x=0.10*. The computed *dM/dT-T* curve to determine T_C is shown in the inset.

Moreover, it was investigated how the external magnetic field affects the resistivity for the samples with and without ***Fe*** substitution. Magneto-electrical transport features have been examined by the standard four-probe technique. In

Fig. 4.37, we depict the resistivity variation of temperature for the pristine and Fe-substituted ceramic materials within a long temperature range of *20-350 K*. When the measurement temperature is increased, ceramic samples with *x=0.0, 0.05,* and *0.1* showed a significant hump where corresponds to ferromagnetic-metal to paramagnetic-insulator transition at the maximum resistivity temperature *(T_{MI}).* However, no such transition is observed for the *20 %* ***Fe*** substituted sample in the studied temperature scale which exhibits semiconducting nature, $d\rho/dt<0$. For the pristine sample, *LSMO*, the metal–insulator transition temperature is observed at *338 K* corresponding well with earlier reports (40) (25) (170). It should also be noted here that, the insulator to the metal transition temperature, found by the peak resistivity temperature, is close to transition temperature found in temperature-dependent magnetization measurements. As the ***Fe*** content increased in the pristine sample, the transition temperature decreases monotonously with a general increase in the electrical resistivity. Iron substitution remarkably effect the electric transport features in *CMR* manganites which can be obviously seen by the significant shift of T_{MI} from *338 K* to *233 K* for *x=0.1* and also the ferromagnetic nature is destroyed with *20 %* ***Fe*** substitution.

These findings can be explained by the associated Jahn-Teller and *DE* mechanisms. For *x=0.0* sample, $La_{0.8}^{3+}Sr_{0.2}^{2+}Mn_{0.8}^{3+}Mn_{0.2}^{4+}O_3^{2-}$, all Mn^{3+} are Jahn-Teller active ions (193) and the amount of Mn^{3+} ions are directly related with both *Mn–O* distortion and polaron binding energy (194) (195). Thus, one may understand that the charge carriers get strongly localized with increasing the Mn^{3+} ion content and as a result, the hopping energy is increased. The Jahn-Teller distortion is reduced in *LSMO* system by substituting inactive Jahn-Teller Fe^{3+} ions in *LSMO* system. Moreover, in pristine sample *(x=0.0),* the networks of Mn^{3+} and Mn^{4+} spins interact strongly with *DE* mechanism. Iron substitution suppress this network and leads an enhancement in the system resistivity. For *x=0.2* sample, such a resistivity behavior with *Fe* substitution elucidates that *Fe* substitution significantly suppresses the contributions arises from the *DE* conduction since iron ions do not contribute to *DE* interaction (196).

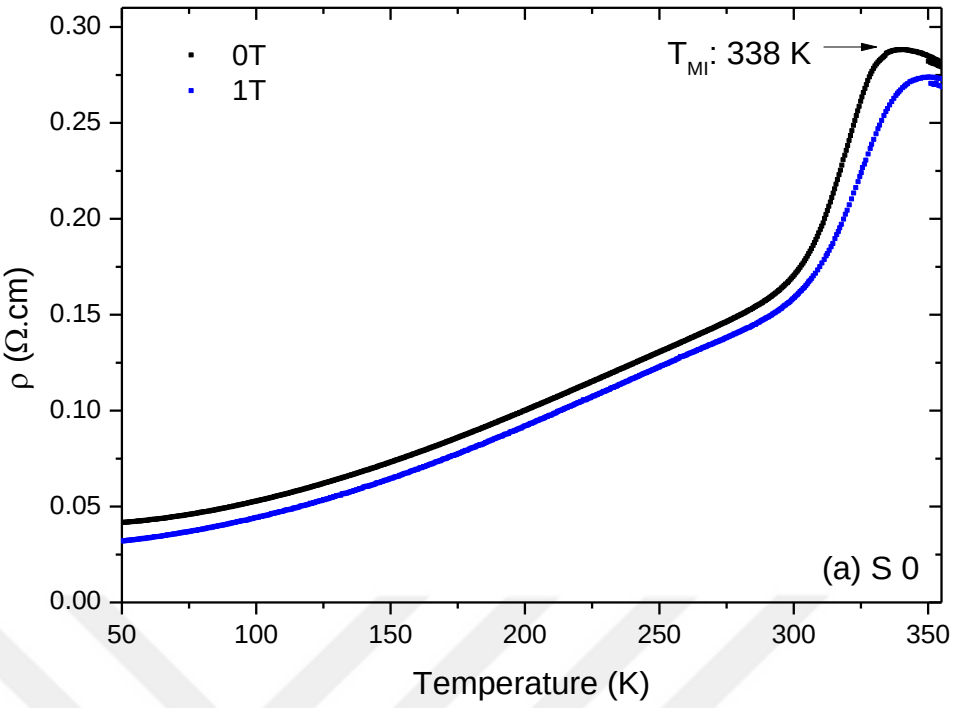
0T
1T
T_{MI}: 338 K
ρ (Ω.cm)
Temperature (K)
(a) S 0

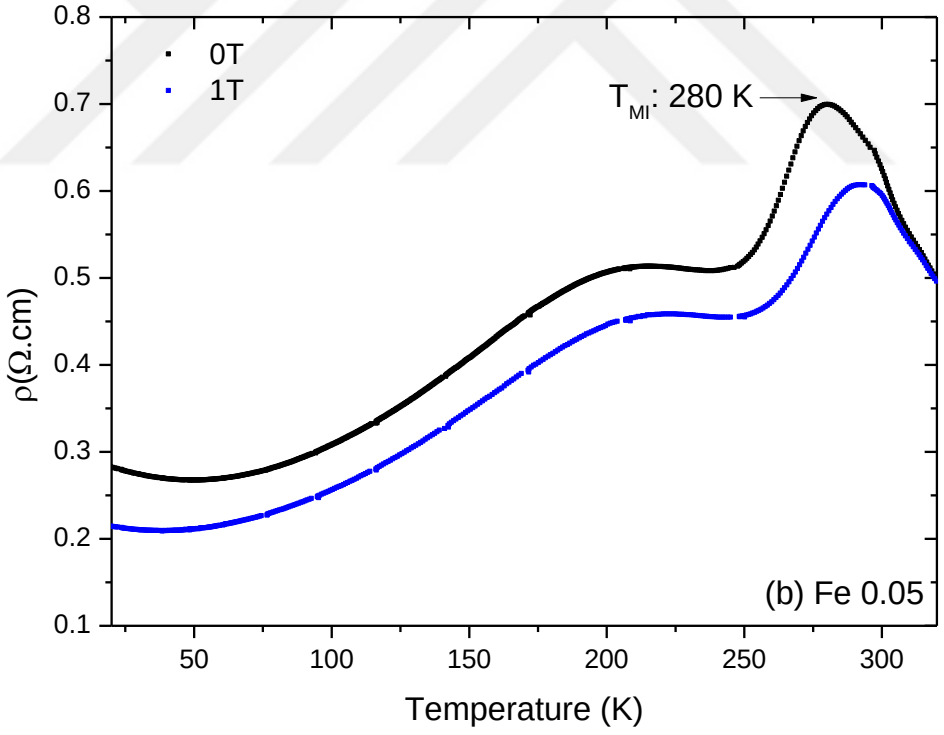
0T
1T
T_{MI}: 280 K
ρ(Ω.cm)
Temperature (K)
(b) Fe 0.05

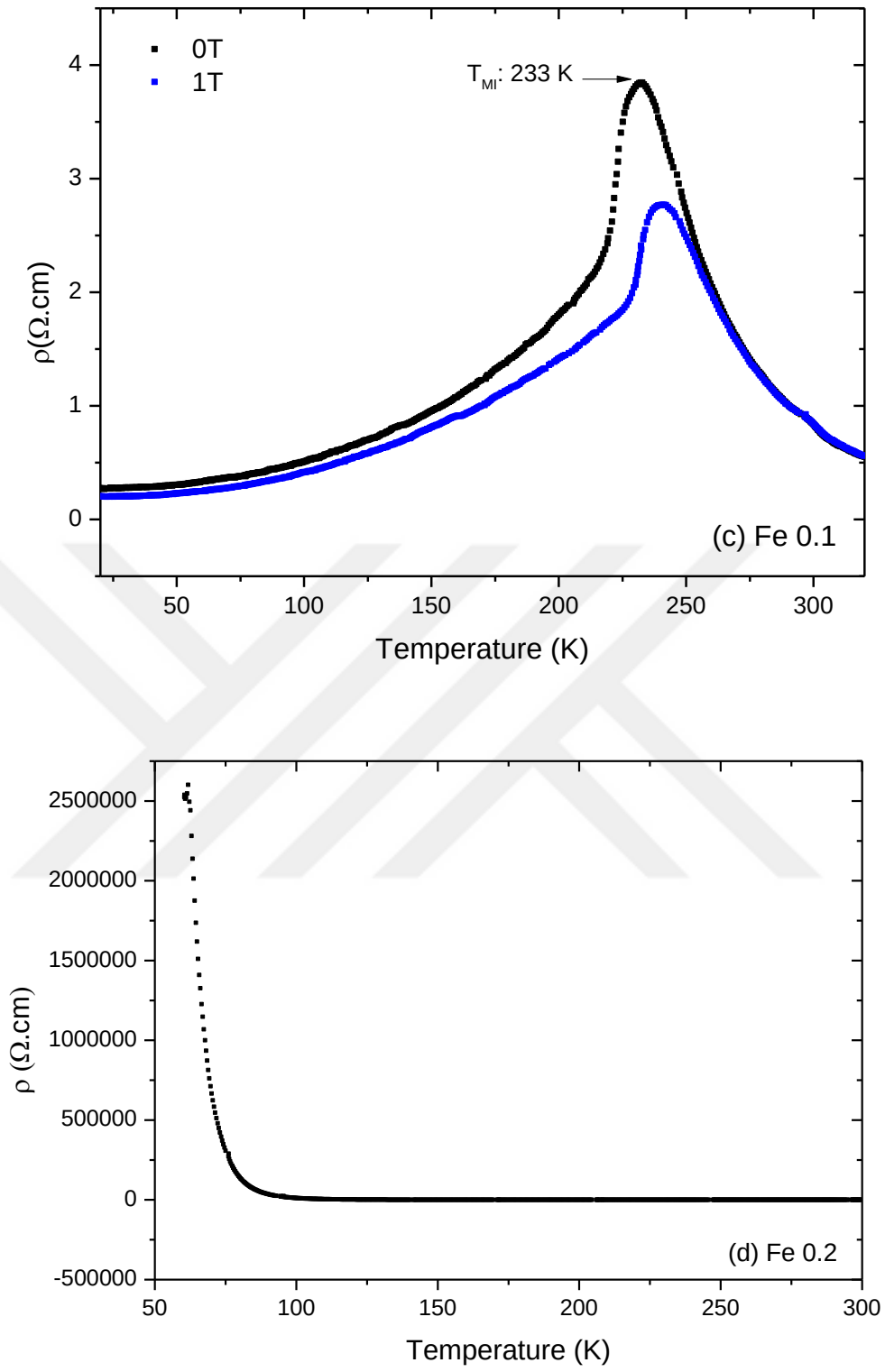

Figure 4.37. Temperature dependence of resistivity in zero field and under magnetic field *1 T* for $La_{0.8}Sr_{0.2}Mn_{1-x}Fe_xO_3$ compounds with ***(a) S 0*** *x=0,00* ***(b)*** *x=0.05*, ***(c)*** *x=0.10* and ***(d)*** *x=0.20.*

The sharpness of metal-insulator transition temperature is given by the temperature coefficient of resistance *(TCR)*. Fig. 4.38 shows the *TCR* values for considered ceramic compounds. The *TCR* is quantified by the equation:

$$\%\, TCR\ = \frac{1}{\rho}\,\frac{d\rho}{dt} \times 100\ \% \qquad (24)$$

where ρ and T are resistivity and temperature, respectively. For the pristine sample the *TCR %* value is $\sim 2.16\ \%\ K^{-1}$ and slightly decrease to $\sim 1.55\%\ K^{-1}$ with *5% Fe* substituted sample. As *x* rise to *0.1*, we obtain the maximum *TCR* value $(\sim 8.23\%\ K^{-1})$ for the corresponding series. Hence, the iron substitution at *Mn*-site leads a reduction of the charge exchange in the networks of *Mn – O* (196). Therefore, the increase in the system resistivity is obtained as mentioned above with lower polaron activation energy and higher *TCR* values. *TCR* value has a crucial role to enhance the sensitivity of uncooled infrared microbolometer. We can make a comparison attempt of the obtained *TCR%* values with those found recently. We can easily regard here that the *TCR* values obtained in the present study is remarkably higher than the previous reported values on *A*- and *B*-site doped manganites (197) (45) (198). Please note that high *TCR %* values are desirable for designing and building temperature sensing devices at room temperature. If we recall the *SEM* results of the *10%* ***Fe*** substituted sample, it is the sample with highest grain size among the rest of the samples that show metal-insulator transition. It is well known that the compounds having large grain size enhances the electrical-transport features of ceramic manganites, that results a sharpened metal-insulator phase transition. Therefore, the *TCR %* value is significantly influenced by the grain size and one should enhance this value by enhancing surface morphology of the samples.

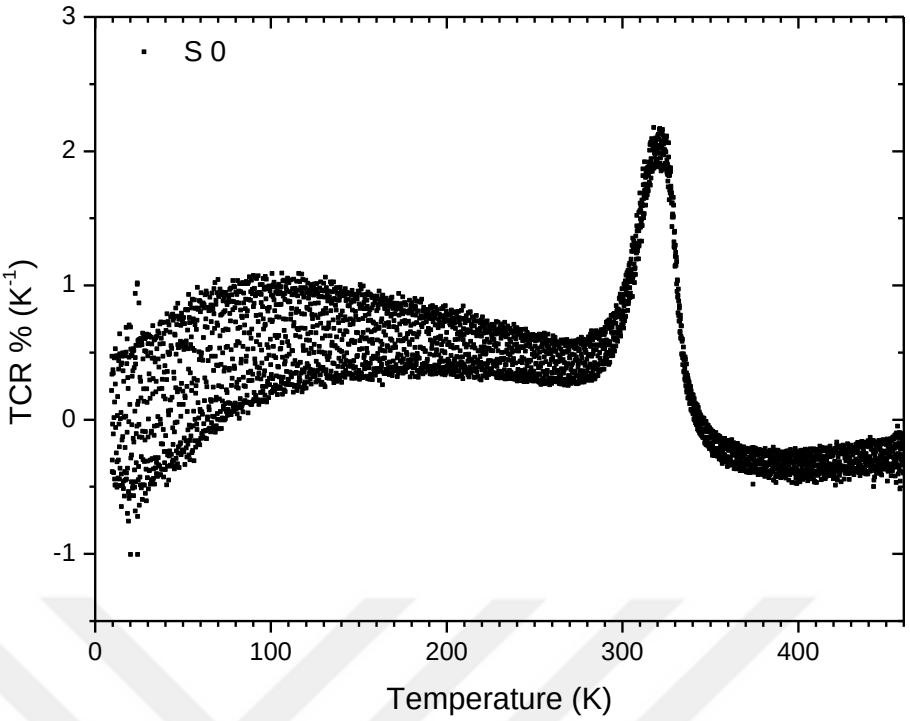
S 0
TCR % (K-1)
Temperature (K)
3
2
1
0
-1
0
100
200
300
400

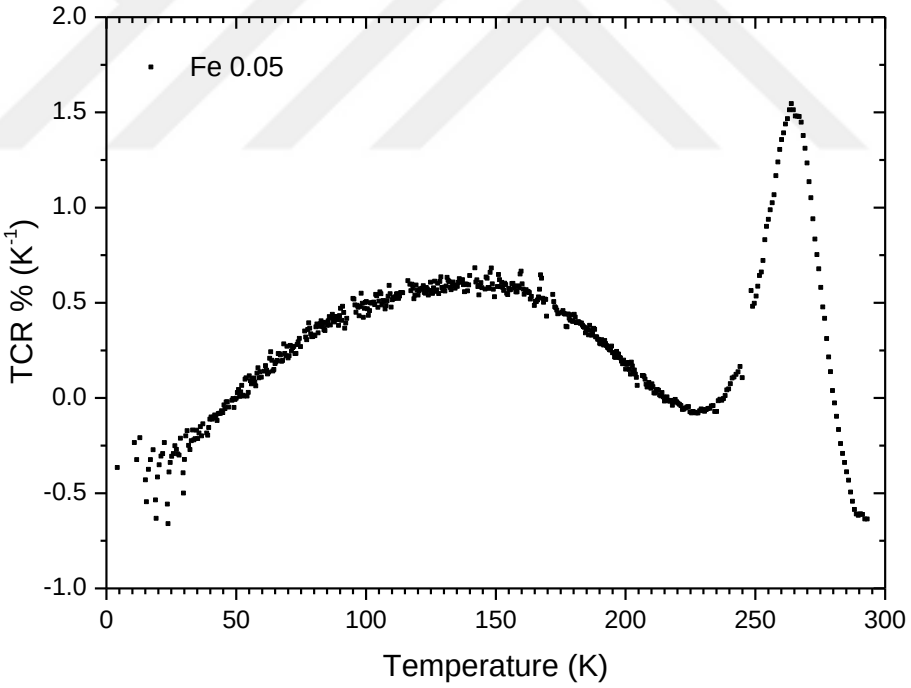
Fe 0.05
TCR % (K-1)
Temperature (K)
2.0
1.5
1.0
0.5
0.0
-0.5
-1.0
0
50
100
150
200
250
300

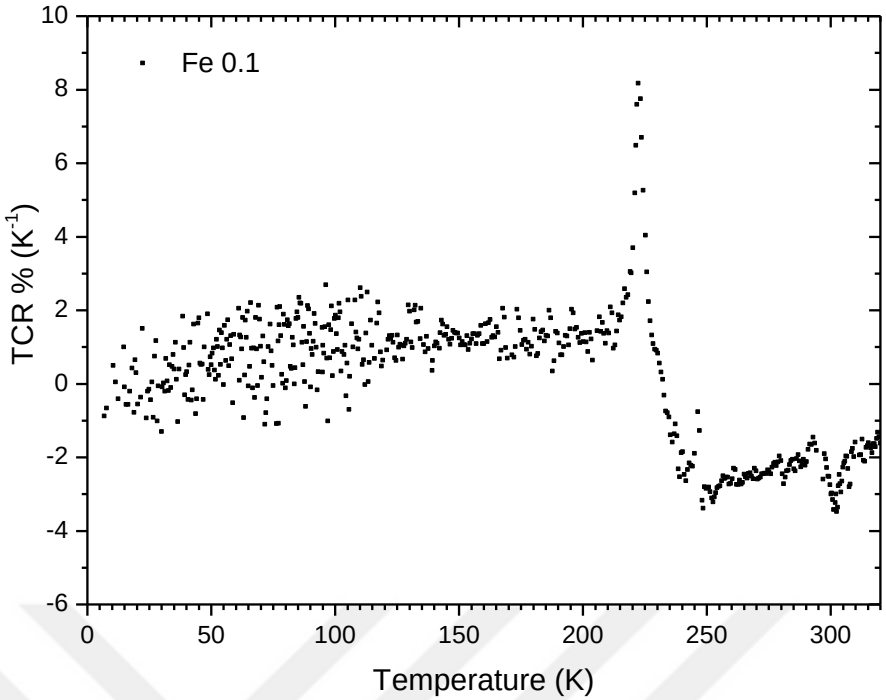

Figure 4.38. Temperature-dependent *TCR %* curves of $La_{0.8}Sr_{0.2}Mn_{1-x}Fe_xO_3$ compounds with ***(a) S 0*** *x=0,00* ***(b)*** *x=0.05* and ***(c)*** *x=0.10.*

To deeply investigate the influence of magnetic field on magnetoresistance *(MR)*, we calculated the *MR%* values and their temperature dependence are shown in the insets of Fig. 4.39. During the magnetization process, the resistivity of the sample can change substantially. The relative change with respect to the value under zero magnetic field can be characterized by the quantity so called *MR%*, and quantified by the following formula;

$$MR\ \% = \frac{(\rho_H - \rho_0)}{\rho_0} x100 \qquad (25)$$

where ρ_0 and ρ_H are the resistivities at the applied magnetic field of zero and *1 T*, respectively. The effect of temperature on magnetoresistance percentage values are plotted in the insets of Fig. 4.39. All the *MR* % vs *T* curves showed similar variation trend, and ***Fe*** content exhibits a significant impact on the magneto-transport features of *LSMO* system. As increasing ***Fe*** content, the maximum *MR%* value remarkably increased, and corresponding maximum *MR* temperatures gradually decreased. Noticeably, the *MR%* value increased from *14.9%* to *48.1%* and maximum *MR* temperature decreased from *320* to *230 K* (Table 4.8).

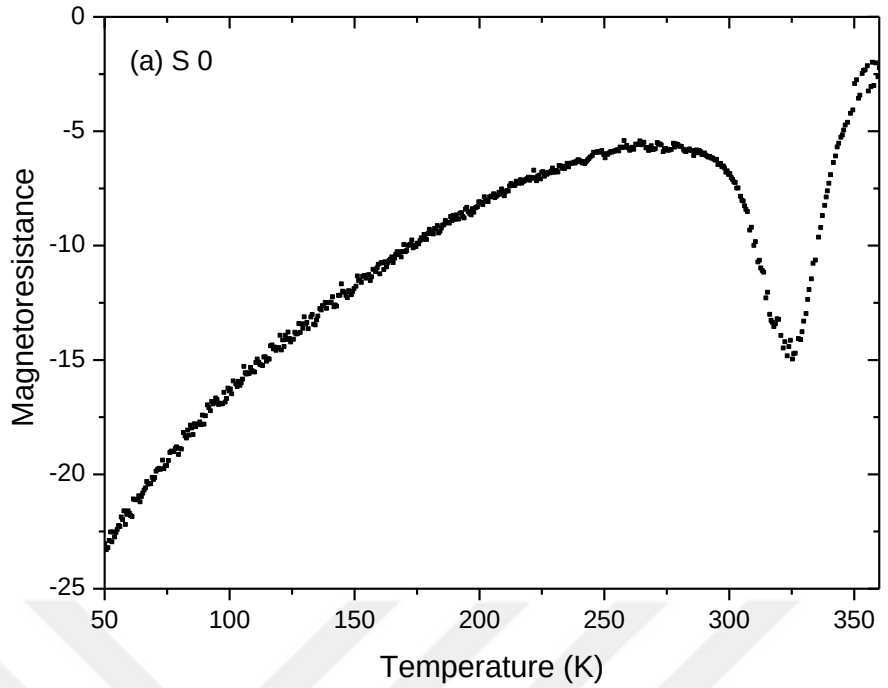
(a) S 0
Magnetoresistance
Temperature (K)
0
-5
-10
-15
-20
-25
50
100
150
200
250
300
350

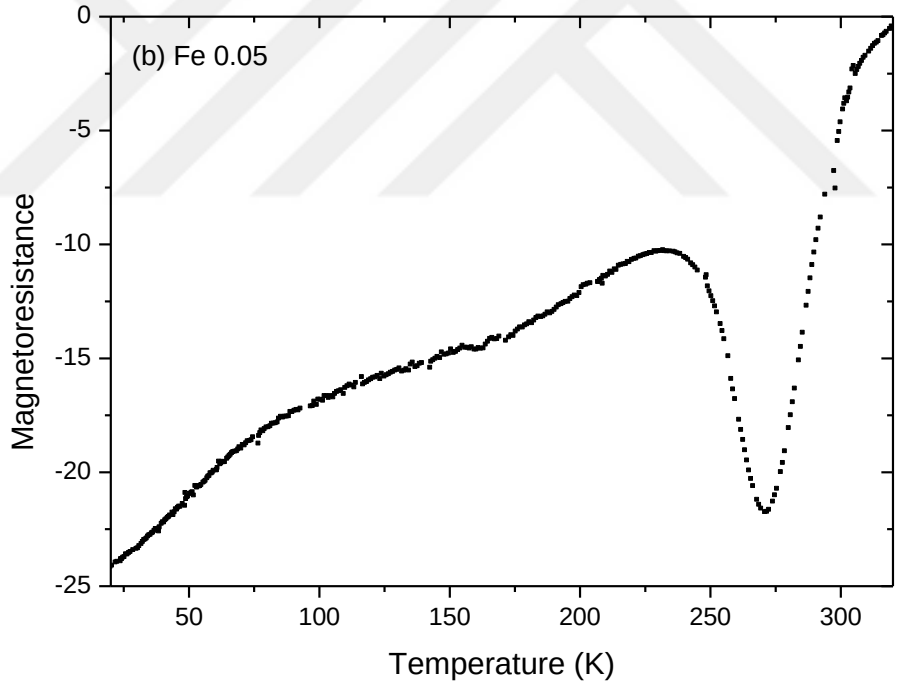
(b) Fe 0.05
Magnetoresistance
Temperature (K)
0
-5
-10
-15
-20
-25
50
100
150
200
250
300

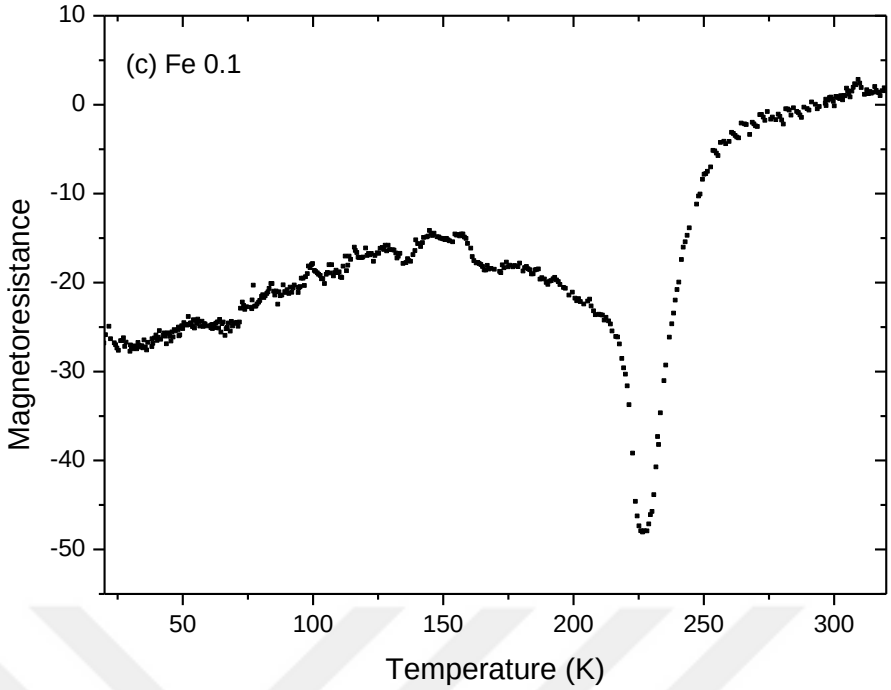

Figure 4.39. The temperature-dependent *MR %* values for $La_{0.8}Sr_{0.2}Mn_{1-x}Fe_xO_3$ compounds with ***(a) S 0*** *x=0,00* ***(b)*** *x=0.05,* ***(c)*** *x=0.10* computed with *H=1 T* applied magnetic field.

4.2.5 Conduction Mechanism Analysis

For a better explanation of electrical behavior and recognize the nature of conduction mechanism above and below T_{MI} regions, the resistivity data were analyzed with empirical equations and well-established models in each region.

4.2.5.1 Low Temperature Metallic Region $T<T_{MI}$

To understand the origin of the transport properties and nature of different scattering mechanisms responsible for the conduction below T_{MI} in the metallic region, the electrical resistivity has been investigated by taking into account several features, such as the weak localization, the electron-electron scattering and the electron-phonon interaction. The transport mechanism for ***Fe***-substituting samples *(x=0.00, 0.05, 0.10* and *0.2)* can be understood by fitting the electrical resistivity data through by an expression including several mechanisms of the scattering according to the following equations, which is generally used to fit the electrical resistivity data in the case of manganites:

$$\rho(T)=\rho_0-\rho_{0.5}T^{0.5}+\rho_2T^2 \qquad (17)$$

$$\rho(T) = \rho_0 - \rho_{0.5}T^{0.5} + \rho_2 T^2 + \rho_5 T^5 \quad (18)$$

where ρ_0 corresponds to the residual resistivity due to grain or domain boundaries (142) (199), term ρ_0 plays an important role in the conduction process due to the contribution of the grains to the grain boundaries in resistivity (199). $\rho_{0.5}T^{0.5}$ weak localization effects of electrons (arises due to contributions from the correlated electron-electron *(e-e)* interactions (200). The term $\rho_2 T^2$ describes the resistivity associated with *(e-e)* scattering (201). Finally, the term $\rho_5 T^5$ in Eq. (2) is indicates electron-phonon interactions *(e-p)* (202).

Fig. 4.40 *(a)* and *(b)* shows the fitting of the resistivity data with Eq. (21) for both ***x=0.00*** and ***x=0.05*** samples in the presence and absence of the magnetic field, while the ***x=0.10*** sample was fitted according to the Eq. (22) as shown in Fig. 1. (c). In general, the quality of these fittings of data is evaluated by comparing the square of linear correlation coefficient *(R^2)* obtained for each equation. Based on this, the R^2 values obtained for each sample was high *(≈99.9%)* which shows that our resistivity data at *0* and *1 T* fit well with the above equations used and confirms the applicability of the proposed scattering mechanisms in the metallic region. The corresponding fitting parameters are tabulated in Table 4.9. The observed parameters are found to decrease with applying *1 T* magnetic field, except on $\rho_{0.5}$ and ρ_2 in ***x=0.20*** sample. The ρ_0 value decreases with the application of the magnetic field due to the increase in the size of the magnetic domains and the decrease in the size of the domain boundary. The decrease in the value of contributing parameters with applying *1 T* magnetic field may be due to decrease in the electron spin fluctuations in the applied magnetic field (203). We find, from the fitting that the values of the residual resistivity are larger than those of the weak localization and electron-electron scattering in each sample ($\rho_0 > \rho_{0.5}T^{0.5} > \rho_2 T^2$), thus indicating that grain boundaries and electron–electron interactions play an important role in the conduction process of our compound.

4.2.5.2 High Temperature Range $T>T_{MI}$: Insulating Regime

The conduction mechanism for manganites at high temperatures in insulating region $T>T_{MI}$ was mainly due to the thermally activated small polarons

(formation of polaron) (142) (204) (205). In the adiabatic regime, the nearest neighboring hopping of small polarons leads to mobility with a thermally activated form, in which charge-carrier motion is faster than lattice vibrations.

In order to explain the ρ-T in $T>T_{MI}$ region for our samples, the conduction process was described by using adiabatic small polaron hopping model *(ASPH)* represented by the following expression (206):

$$\rho\,(T) = \rho_a T\ exp\ (\frac{E_a}{K_B T}) \tag{13}$$

where ρ_a is the residual resistivity or resistivity coefficient ($\rho_a = 2K_B/3ne^2a^2\upsilon$), E_a represents the activation energy for hopping conduction and K_B is Boltzmann's constant. *e* is the electronic charge, *n* is the density of charge carriers, *a* is the site-to-site hopping distance and υ is the longitudinal optical phonon frequency. *T* is the absolute temperature.

Fig. 4.40 *(b), (c)* and *(d)* at *0* and *1 T* shows the results of fitting the resistivity data in insulating region for ***x=0.05, 0.10*** and ***0.2*** samples, in which the straight lines are fits to the *ASPH* model. Our fitting gives the good R^2, this confirms that the transport properties are dominated by the Small Polaron Hopping mechanism in the studied regions. The corresponding fitting parameters for this model are presented in Table 4.10. It can be seen from the Table 4.10 that the ρ_a shows a complex correlation as a function of ***Fe***-content, first decreasing in ***x=0.10*** sample and then significant increase in ***x = 0.20*** sample. While, we find that the activation energy increases with ***Fe***-content for ***x=0.10***, may be due to the fact that increase in ***Fe*** concentration lowers the possibility of conduction electron to hop to the neighboring sites (203) (207) (208). Whereas, we found the opposite with a greater increase in the ***Fe*** concentration ***(x=0.2)***, which results in a decrease in the activation energy. This decrease in E_a may result from the localization of the e_g carriers due to increase in the available number of sites where the electron can move (35). In addition to this, activation energy values of all the compounds of the present investigation decrease in the present of magnetic field and this consistent with the observed electrical resistivity properties. This reduction in E_a may be attributed to that the values of charge localization decreases with application of external magnetic field.

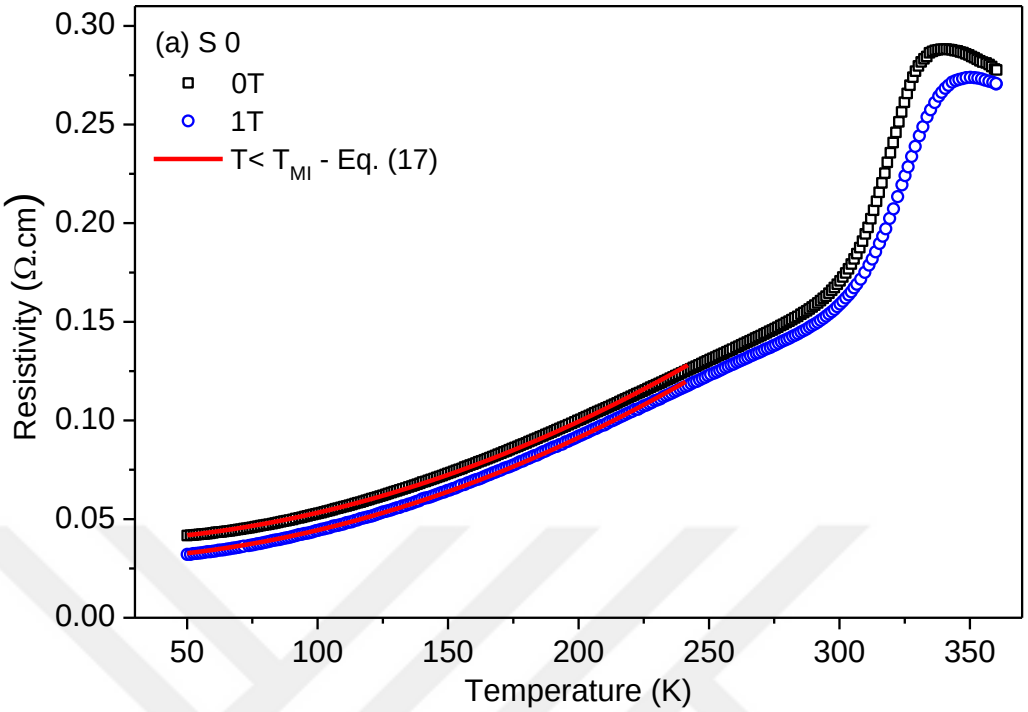
(a) S 0
0T
1T
T< T_MI - Eq. (17)
Resistivity (Ω.cm)
Temperature (K)
0.00
0.05
0.10
0.15
0.20
0.25
0.30
50
100
150
200
250
300
350

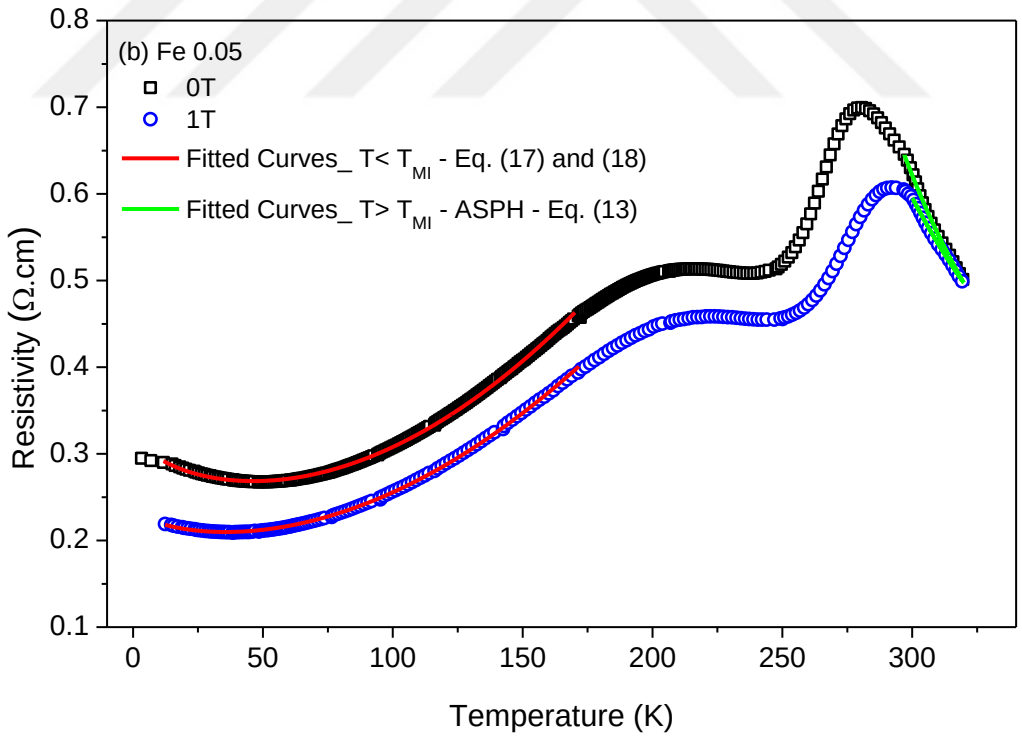
(b) Fe 0.05
0T
1T
Fitted Curves_ T< T_MI - Eq. (17) and (18)
Fitted Curves_ T> T_MI - ASPH - Eq. (13)
Resistivity (Ω.cm)
Temperature (K)
0.1
0.2
0.3
0.4
0.5
0.6
0.7
0.8
0
50
100
150
200
250
300

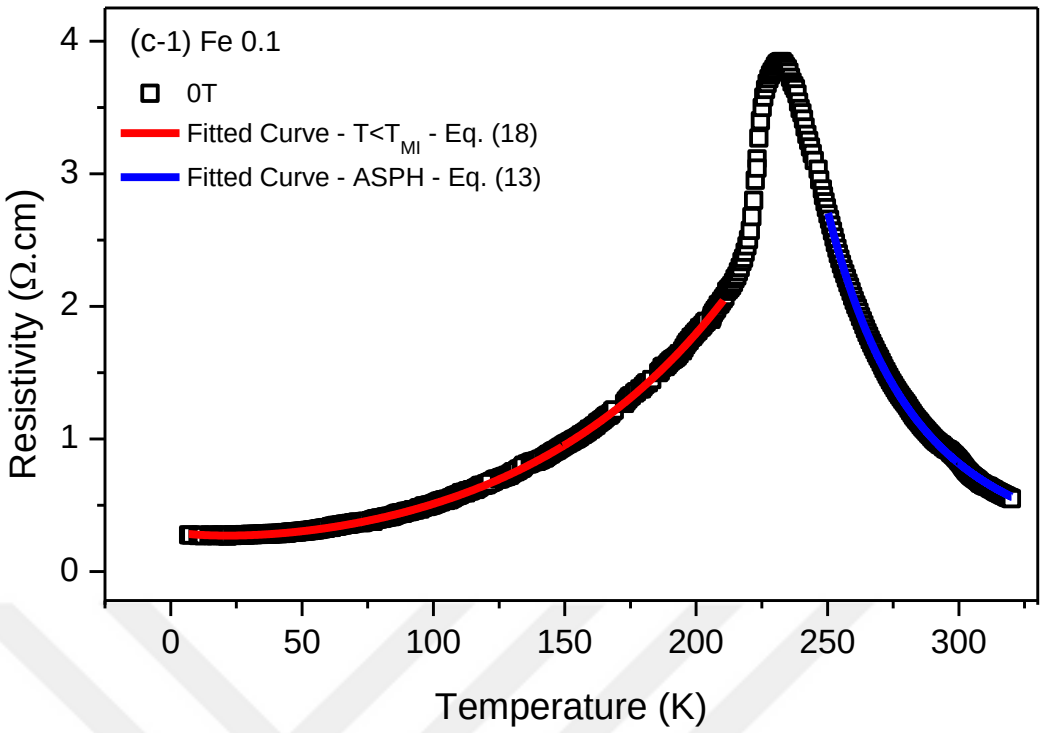
(c-1) Fe 0.1
0T
Fitted Curve - T<T$_{MI}$ - Eq. (18)
Fitted Curve - ASPH - Eq. (13)
Resistivity (Ω.cm)
Temperature (K)
0
1
2
3
4
0
50
100
150
200
250
300

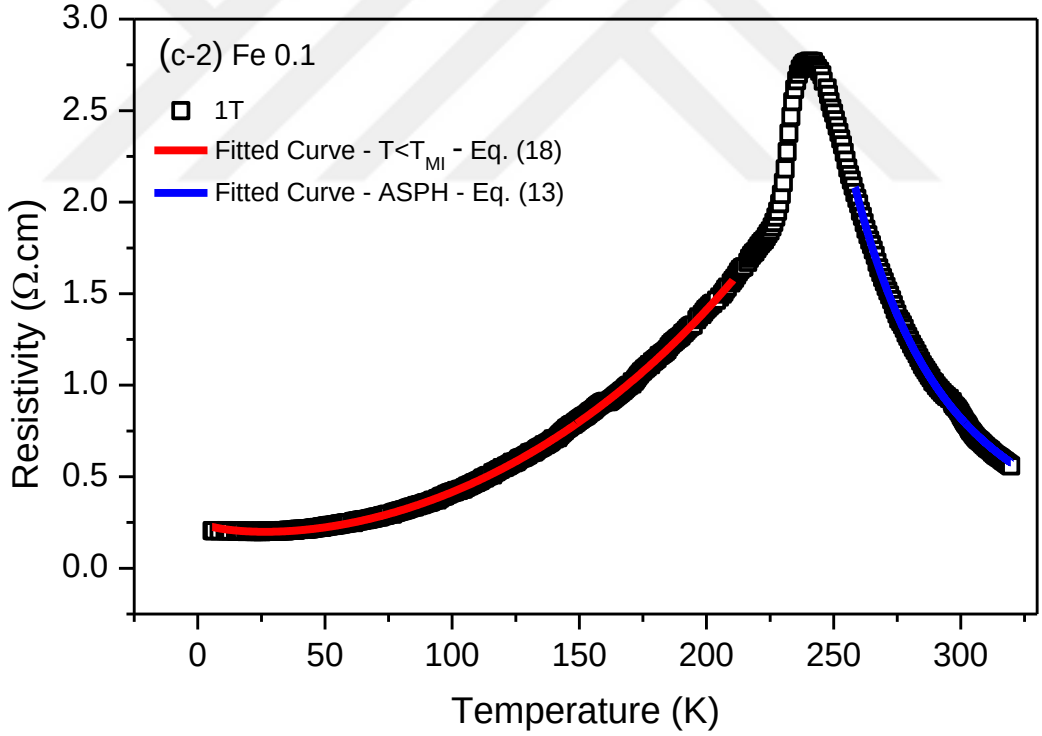
(c-2) Fe 0.1
1T
Fitted Curve - T<T$_{MI}$ - Eq. (18)
Fitted Curve - ASPH - Eq. (13)
Resistivity (Ω.cm)
Temperature (K)
0.0
0.5
1.0
1.5
2.0
2.5
3.0
0
50
100
150
200
250
300

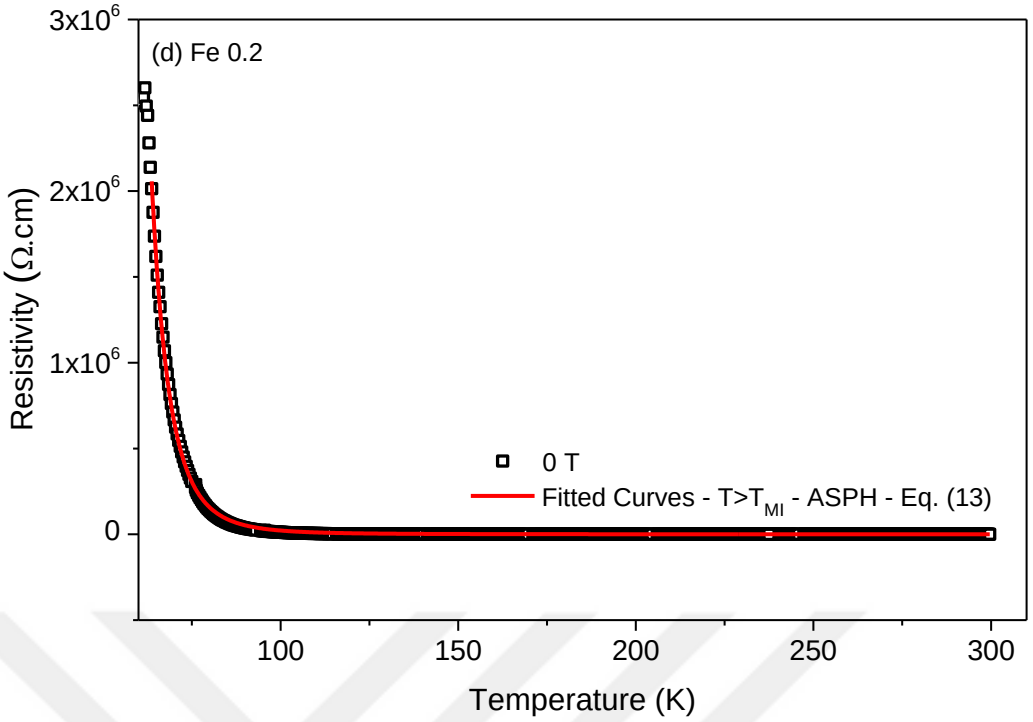

Figure 4.40. Temperature dependence of the electrical resistivity for $La_{0.8}Sr_{0.2}Mn_{1-x}B_xO_{3\pm\delta}$ compounds for $La_{0.8}Sr_{0.2}Mn_{1-x}Fe_xO_3$ compounds with *B:* ***(a)*** *x=0,00* ***(b)*** *x=0.05*, ***(c)*** *x=0.10* and ***(d)*** *x=0.20.* The colorful lines indicate the best fit for theoretical models.

Table 4.9. Parameters used to fit the experimental data of resistivity for $La_{0.8}Sr_{0.2}Mn_{1-x}B_xO_{3\pm\delta}$ compounds for $La_{0.8}Sr_{0.2}Mn_{1-x}Fe_xO_3$ compounds with *B:* ***(a)*** *x=0,00* ***(b)*** *x=0.05* and ***(c)*** *x=0.10* for low *T* ($T<T_{MI}$) using Eqs. (17) and (18).

$La_{0.8}Sr_{0.2}Mn_{1-x}B_xO_{3\pm\delta}$			
		0 T	**1 T**
S 0	ρ_0 **(Ω cm)**	0.0385	0.0289
	$\rho_{0.5}$ **(Ω cm $K^{-0.5}$)**	8.2086×10^{-5}	1.7481×10^{-5}
	ρ_2 **(Ω cm K^{-2})**	1.5516×10^{-7}	1.5657×10^{-6}
	R^2	**0.999**	**0.999**
Fe 0.05	ρ_0 **(Ω cm)**	0.3345	0.2426
	$\rho_{0.5}$ **(Ω cm $K^{-0.5}$)**	0.0129	0.0073×10^{-4}
	ρ_2 **(Ω cm K^{-2})**	1.0268×10^{-6}	8.6330×10^{-6}
	R^2	**0.999**	**0.999**
Fe 0.1	ρ_0 **(Ω cm)**	0.3149	0.2664
	$\rho_{0.5}$ **(Ω cm $K^{-0.5}$)**	0.01223	0.0174
	ρ_2 **(Ω cm K^{-2})**	3.057×10^{-5}	3.2069×10^{-5}
	ρ_5 **(Ω cm K^{-5})**	1.3508×10^{-12}	3.3991×10^{-13}
	R^2	**0.999**	**0.999**

Table 4.10. Parameters used to fit the experimental data $La_{0.8}Sr_{0.2}Mn_{1-x}B_xO_{3\pm\delta}$ compounds for $La_{0.8}Sr_{0.2}Mn_{1-x}Fe_xO_3$ compounds with *B:* ***(a)*** *x=0,00* ***(b)*** *x=0.05* and ***(c)*** *x=0.10* for high *T* ($T>T_{MI}$) using Eqs. (10), (13) and (14).

$La_{0.8}Sr_{0.2}Mn_{1-x}B_xO_{3\pm\delta}$				
			0 T	**1 T**
Fe 0.05	**ASPH**	ρ_0 *(Ω cm)*	2.0193×10^{-5}	3.8666×10^{-5}
		E_a *(meV)*	119.7088	101.8243
		R^2	**0.995**	**0.999**
Fe 0.1	**ASPH**	ρ_a *(Ω cm)*	2.661×10^{-6}	3.2979×10^{-6}
		E_a *(meV)*	179.146	173.707
		R^2	**0.999**	**0.998**
Fe 0.2	**ASPH**	ρ_a *(Ω cm)*	0.03485	*
		E_a *(meV)*	75.438	*
		R^2	**0.999**	*

5. CONCLUSIONS AND RECOMMENDATIONS

In this thesis, we have examined two series of *LSMO* systems both produced by *B*-site substitution are examined. The first series includes the comparative investigation of *10%* transition metal substituting of the *Mn*-site in $La_{0.8}Sr_{0.2}Mn_{0.1}O_3$ system, i.e. $La_{0.8}Sr_{0.2}Mn_{0.9}Cu_{0.1}O_3$, $La_{0.8}Sr_{0.2}Mn_{0.9}Co_{0.1}O_3$, $La_{0.8}Sr_{0.2}Mn_{0.9}Fe_{0.1}O_3$, $La_{0.8}Sr_{0.2}Mn_{0.9}Ti_{0.1}O_3$. The structural, magnetic, and electrical-transport features were examined. In the second series, the influence of iron content on the structural, microstructural, magnetic, and electrical-transport features of the ceramic perovskite manganites of the $La_{0.8}Sr_{0.2}Mn_{1-x}Fe_xO_3$ *(x=0.0, 0.05, 0.1, and 0.2)* system was investigated.

In the first part, all ceramic manganites were produced using the standard solid-state reaction method. The crystal structure of the samples was fitted with the rhombohedral space group *($R\bar{3}c$) (No:167)* without detecting any impurity phase, as approved by Jana refinements. Moreover, the average particle sizes were calculated by using Gaussian fitting method which increases from *2.45 μm* for ***S0*** sample to the *4.77 μm* for ***Cu*** sample, *2.67 μm* for ***Co*** sample, *3.27 μm* for ***Fe*** sample except *2.21 μm* for ***Ti*** sample. The transition temperature T_{MI} in which the ferromagnetic-metal to the paramagnetic-insulator phase transition of the samples were found *338 K* for ***S 0***, *304 K* for ***Cu***, *97 K* for ***Co***, *233 K* for ***Fe***, and *209 K* for ***Ti***. The minimum point of the derivative *dM/dT* gives the Curie temperature which were found *321 K* for ***S 0***, *294 K* for ***Cu***, *118 K* for ***Co***, *279 K* for ***Fe***, *219 K* for ***Ti***. In regards to magnetization and electrical resistivity analysis showed that both T_C and T_{MI} values decrease with *TM* substitution which is attributed to the suppression of the *DE* interaction. Substituting inactive Jahn-Teller ions decrease the ratio of Mn^{3+}/Mn^{4+} which results to reduce the *FM* coupling between Mn^{3+}-O^{2-}-Mn^{4+} bonds. In addition; the greatest *TCR* value is obtained with *8.23 % K-1* for ***Fe*** substituted sample. And, the largest *MR* percentage value of *48 %* was calculated in the ***Fe*** substituted sample at about *230 K*. The greatest *TCR* and *MR* values obtained showed that we should study different moles of iron substitution in the second series.

In the second part of the thesis, all ceramic manganites were fabricated using the standard solid-state reaction method. *XRD* analysis gives that all samples crystallize in a rhombohedral structure with *($R\bar{3}c$) (No:167)* space group without detecting any impurity phase, as approved by Jana refinements. Besides, the *XRD* results denote a slight increase in the lattice parameters with the ***Fe*** substitution. According to the *SEM* images, we obtain the average grain sizes that decrease by the amount of ***Fe***-content from *2.45 μm* (*x=0.0*) to *4.24 μm* (*x=0.2)*. Also, magnetization and electrical resistivity study indicated that both T_C and T_{MI} values decrease with ***Fe*** substitution which is attributed to the suppression of the *DE* interaction. Substituting inactive Jahn-Teller Fe^{3+} ions decrease the ratio of Mn^{3+}/Mn^{4+} which results to reduce the *FM* coupling between Mn^{3+}-O^{2-}-Mn^{4+} bonds. The calculated low-field *(1 T) MR* is improved by substitution and reaches *48.1 %* for the *10 %* iron substituted sample. Also, for the same sample, the *TCR* value reached *8.23%* K^{-1}. These findings suggest that the synthesized ceramic materials can be used for a wide range of applications, including temperature sensing devices. Moreover, to understand the main reason for the conduction mechanism, we analyzed the *ρ-T* data with empirical equations and well-known models above and below T_{MI}. The results obtained in this dissertation will be used as a reference for future work, and the electrochemical analysis will be carried out to use them as cathode materials in intermediate and high temperature *SOFC*.

6. REFERENCES

"Vancouver citation system was used in this thesis."

1. Yu X, Jin S, Li H, Guan X, Gu X, Liu X. High room-temperature TCR and MR of La1-Sr MnO3 thin films for advanced uncooled infrared bolometers and magnetic sensors. Appl Surf Sci [Internet]. 2021 Dec;570:151221. Available from: https://linkinghub.elsevier.com/retrieve/pii/S0169433221022753
2. Moualhi Y, Rahmouni H, Gassoumi M, Khirouni K. Summerfield scaling model and conduction processes defining the transport properties of silver substituted half doped (La–Ca) MnO3 ceramic. Ceram Int [Internet]. 2020 Oct;46(15):24710–7. Available from: https://linkinghub.elsevier.com/retrieve/pii/S0272884220319210
3. Jin S, Gu X, Yu X, Guan X, Li H, Chu K, et al. Improved room-temperature TCR of La0.7Ag0.125K0.175MnO3 films by optimizing sintering temperatures. Appl Surf Sci [Internet]. 2021 Dec;570:151222. Available from: https://linkinghub.elsevier.com/retrieve/pii/S0169433221022765
4. Sfirloaga P, Poienar M, Malaescu I, Lungu A, Mihali CV, Vlazan P. Electrical conductivity of Ca-substituted lanthanum manganites. Ceram Int [Internet]. 2018 Apr;44(6):5823–8. Available from: https://linkinghub.elsevier.com/retrieve/pii/S0272884218300403
5. Jin S, Zhang S, Li H, Chu K, Yu X, Guan X, et al. A-site Na-doping to enhance room-temperature TCR of La1-Na MnO3 polycrystalline ceramics. Mater Today Commun [Internet]. 2021 Sep;28:102496. Available from: https://linkinghub.elsevier.com/retrieve/pii/S2352492821004888
6. Kumar Verma M, Dutt Sharma N, Sharma S, Choudhary N, Singh D. High magnetoresistance in La0.5Nd0.15Ca0.25A0.1MnO3 (A = Ca, Li, Na, K) CMR manganites: Correlation between their magnetic and electrical properties. Mater Res Bull [Internet]. 2020;125:110813. Available from: https://www.sciencedirect.com/science/article/pii/S0025540819322998
7. Zhong W, Au C-T, Du Y-W. Review of magnetocaloric effect in perovskite-type oxides. Chinese Phys B [Internet]. 2013 May;22(5):057501. Available from: https://iopscience.iop.org/article/10.1088/1674-1056/22/5/057501
8. Saha S, Bandyopadhyay S, Das I. Role of short-range magnetic interaction between core and surface spins in exchange bias and memory effect in nanocrystalline doped manganite. J Alloys Compd [Internet]. 2021 Jul;870:159465. Available from: https://linkinghub.elsevier.com/retrieve/pii/S0925838821008744
9. Ferreira MC, Pimentel B, Andrade V, Zverev V, Gimaev RR, Pomorov AS, et al. Understanding the Dependence of Nanoparticles Magnetothermal Properties on Their Size for Hyperthermia Applications: A Case Study for La-Sr Manganites. Nanomaterials [Internet]. 2021 Jul 14;11(7):1826. Available from: https://www.mdpi.com/2079-4991/11/7/1826
10. Wu L, Jiang Z, Wang S, Xia C. (La,Sr)MnO3–(Y,Bi)2O3 composite cathodes for intermediate-temperature solid oxide fuel cells. Int J Hydrogen Energy [Internet]. 2013 Feb;38(5):2398–406. Available from: https://linkinghub.elsevier.com/retrieve/pii/S0360319912026006
11. dos Santos-Gómez L, Zamudio-García J, Porras-Vázquez JM, Losilla ER, Marrero-López D. Highly efficient La0.8Sr0.2MnO3-δ - Ce0.9Gd0.1O1.95 nanocomposite cathodes for solid oxide fuel cells. Ceram Int [Internet]. 2018 Apr;44(5):4961–6. Available from: https://linkinghub.elsevier.com/retrieve/pii/S0272884217327967
12. Zener C. Interaction between the d-Shells in the Transition Metals. II. Ferromagnetic Compounds of Manganese with Perovskite Structure. Phys Rev [Internet]. 1951 May 1;82(3):403–5. Available from: https://link.aps.org/doi/10.1103/PhysRev.82.403

13. Anderson PW, Hasegawa H. Considerations on Double Exchange. Phys Rev [Internet]. 1955 Oct 15;100(2):675–81. Available from: https://link.aps.org/doi/10.1103/PhysRev.100.675

14. Goodenough JB. Theory of the Role of Covalence in the Perovskite-Type Manganite (La,M(II))MnO3. Phys Rev [Internet]. 1955 Oct 15;100(2):564–73. Available from: https://link.aps.org/doi/10.1103/PhysRev.100.564

15. Kurbakov AI, Ryzhov VA, Runov V V., Bykov EO, Larionov II, Deriglazov V V., et al. Study of phase separation phenomena in half-doped manganites with isovalent substitution of rare-earth cations on example of Sm0.32Pr0.18Sr0.5MnO3. Phys Rev B [Internet]. 2019 Nov 27;100(18):184424. Available from: https://link.aps.org/doi/10.1103/PhysRevB.100.184424

16. Shi JY, Zhang AM, Wang WX, Cui JY, Zhang WJ, Wu XS. Effects of A-site cation disordering on the transport properties of half-doping La0.5Ca0.5MnO3 manganites. Chem Phys Lett [Internet]. 2018 Aug;706:223–7. Available from: https://linkinghub.elsevier.com/retrieve/pii/S0009261418304688

17. Joshi L, Keshri S. Magneto-transport properties of Fe-doped LSMO manganites. Measurement [Internet]. 2011 Jun;44(5):938–45. Available from: https://linkinghub.elsevier.com/retrieve/pii/S0263224111000613

18. Lakhal E, Amira A, Chihoub R, Soylu N, Altintas SP, Varilci A, et al. Improved Magnetoresistance in Sm0.7-xCexSr0.3MnO3 Manganites Prepared by a Sol–Gel Route. J Low Temp Phys [Internet]. 2021 Jul 19;204(1–2):48–56. Available from: https://link.springer.com/10.1007/s10909-021-02598-4

19. Boufligha S, Mahamdioua N, Denbri F, Meriche F, Altintas SP, Terzioglu C. Synthesis and Experimental Study of Structure, Magnetotransport Properties and Temperature Coefficient of Resistance of La0.7Ca0.18Ba0.12Mn0.95Sn0.05O3 Manganite. J Low Temp Phys [Internet]. 2021 Nov 23; Available from: https://link.springer.com/10.1007/s10909-021-02645-0

20. Mohan C., Seeger M, Kronmüller H, Murugaraj P, Maier J. Critical behaviour near the ferromagnetic–paramagnetic phase transition in La0.8Sr0.2MnO3. J Magn Magn Mater [Internet]. 1998 Mar;183(3):348–55. Available from: https://linkinghub.elsevier.com/retrieve/pii/S0304885397010950

21. Grossin D, Noudem JG. Synthesis of fine La0.8Sr0.2MnO3 powder by different ways. Solid State Sci [Internet]. 2004 Sep;6(9):939–44. Available from: https://linkinghub.elsevier.com/retrieve/pii/S1293255804001591

22. Zhou Y, Zhu X, Li S. Effects of copper doping on the structure, electrical and low-field magnetoresistance properties of (1–x)La0.67Sr0.33MnO3/xCu (x=0–0.15) composite coatings. Ceram Int [Internet]. 2017 Sep;43(13):10026–31. Available from: https://linkinghub.elsevier.com/retrieve/pii/S0272884217308155

23. Mahamdioua N, Amira A, Altintas SP, Saoudel A, Boudjadja Y, Amirouche L, et al. Structural and Magneto-Transport Properties of Copper Doped Double Layered Manganites La1.4Ca1.6Mn2O7. J Supercond Nov Magn [Internet]. 2013 May 29;26(5):1441–4. Available from: http://link.springer.com/10.1007/s10948-012-2024-0

24. Ahsan MZ, Ahsan PMA, Islam MA, Asif FC. Structural and electrical properties of copper doped lanthanum manganite NPs. Results Phys [Internet]. 2019 Dec;15:102600. Available from: https://linkinghub.elsevier.com/retrieve/pii/S2211379719320777

25. Sudakshina B, Arun B, Chandrasekhar KD, Yang HD, Vasundhara M. Structural and magnetic properties of Nd 0.67 Ba 0.33 MnO 3 manganites with partial replacement of Fe and Cu at Mn-site. Phys B Condens Matter [Internet]. 2018 Jun;539:14–20. Available from: https://linkinghub.elsevier.com/retrieve/pii/S0921452618302606

26. Shang C, Xia ZC, Wei M, Jin Z, Chen BR, Shi LR, et al. Tuning of cu doping on phase transition and high-field phase diagram of Nd0.5Sr0.5Mn1−Cu O3. J Magn Magn Mater [Internet]. 2016 Oct;416:357–65. Available from: https://linkinghub.elsevier.com/retrieve/pii/S0304885316306710

27. Ngan LTT, Dang NT, Nam PH, Khan DT, Nguyen LH, Bau L V., et al. Prediction of Magnetocaloric Effects of La0.7Sr0.3Mn1-xCuxO3 Compounds (x = 0.08 and 0.12) Using a Phenomenological Model. J Electron Mater [Internet]. 2021 Mar 28;50(3):978–86. Available from: http://link.springer.com/10.1007/s11664-020-08617-6

28. Liu Z, Lin WG, Zhou KW, Yan JL. Effect of Cu doping on the structural, magnetic and magnetocaloric properties of La0.7Sr0.25Na0.05Mn1−xCuxO3 manganites. Ceram Int [Internet]. 2018 Feb;44(3):2797–802. Available from: https://linkinghub.elsevier.com/retrieve/pii/S027288421732463X

29. Chebaane M, Bellouz R, Oumezzine M, Hlil EK, Fouzri A. Copper-doped lanthanum manganite La 0.65 Ce 0.05 Sr 0.3 Mn 1−x Cu x O 3 influence on structural, magnetic and magnetocaloric effects. RSC Adv [Internet]. 2018;8(13):7186–95. Available from: http://xlink.rsc.org/?DOI=C7RA13244A

30. Schl&#65533;gl F. A characteristic class of quantities in nonequilibrium thermodynamics and a statistical justification of the local equilibrium approximation. Zeitschrift f&#65533;r Phys B Condens Matter Quanta [Internet]. 1975 Jun;20(2):177–84. Available from: http://link.springer.com/10.1007/BF01315688

31. Altintas SP. Structural and magneto-transport features of cobalt-substituted mixed-valence manganites. J Mater Sci Mater Electron [Internet]. 2021 Mar 15;32(6):7176–86. Available from: http://link.springer.com/10.1007/s10854-021-05426-3

32. Selmi A, M'nassri R, Cheikhrouhou-Koubaa W, Chniba Boudjada N, Cheikhrouhou A. Influence of transition metal doping (Fe, Co, Ni and Cr) on magnetic and magnetocaloric properties of Pr0.7Ca0.3MnO3 manganites. Ceram Int [Internet]. 2015 Sep;41(8):10177–84. Available from: https://linkinghub.elsevier.com/retrieve/pii/S0272884215008792

33. Gdaiem MA, Ghodhbane S, Dhahri A, Dhahri J, Hlil EK. Effect of cobalt on structural, magnetic and magnetocaloric properties of La0.8Ba0.1Ca0.1Mn1-xCoxO3 (x = 0.00, 0.05 and 0.10) manganites. J Alloys Compd [Internet]. 2016 Oct;681:547–54. Available from: https://linkinghub.elsevier.com/retrieve/pii/S0925838816311227

34. Syed Ali KS, Saravanan R, Pashchenko A V, Pashchenko VP. Local distortion in Co-doped LSMO from entropy-maximized charge density distribution. J Alloys Compd [Internet]. 2010;501(2):307–12. Available from: https://www.sciencedirect.com/science/article/pii/S0925838810009096

35. Debnath JC, Wang J. Magnetic and electrical response of Co-doped La0.7Ca0.3MnO3 manganites/insulator system. Phys B Condens Matter [Internet]. 2017 Jan;504:58–62. Available from: https://linkinghub.elsevier.com/retrieve/pii/S0921452616304781

36. Chen W, Chen Y, Wu W, Li T, Zhang C, Zhou Y, et al. Lattice Strain and Magnetic Property Evolution of La0.5Sr0.5Mn1−x Co x O3 Synthesized by Solid-State Reaction at Low Temperatures. J Supercond Nov Magn [Internet]. 2016 Jan 19;29(1):115–22. Available from: http://link.springer.com/10.1007/s10948-015-3218-z

37. Ogale SB, Shreekala R, Bathe R, Date SK, Patil SI, Hannoyer B, et al. Transport properties, magnetic ordering, and hyperfine interactions in Fe-doped La0.75Ca0.25MnO3. Phys Rev B [Internet]. 1998 Apr 1;57(13):7841–5. Available from: https://link.aps.org/doi/10.1103/PhysRevB.57.7841

38. Laiho R, Lisunov KG, Lähderanta E, Salminen J, Shakhov MA, Stamov VS, et al. Non-universal low-field magnetic scaling and variable-range hopping conductivity as a consequence of disorder in La1−xCaxMn1−yFeyO3. J Phys Chem Solids [Internet]. 2003;64(9):1573–7. Available from: https://www.sciencedirect.com/science/article/pii/S0022369703001914

39. Ahn KH, Wu XW, Liu K, Chien CL. Magnetic properties and colossal magnetoresistance of La(Ca)Mn${\mathrm{O}}_{3}$ materials doped with Fe. Phys Rev B [Internet]. 1996 Dec 1;54(21):15299–302. Available from: https://link.aps.org/doi/10.1103/PhysRevB.54.15299

40. Mostafa AG, Abdel-Khalek EK, Daoush WM, Moustfa SF. Study of some co-precipitated manganite perovskite samples-doped iron. J Magn Magn Mater [Internet]. 2008

Dec;320(24):3356–60. Available from: https://linkinghub.elsevier.com/retrieve/pii/S0304885308007828

41. Leung LK, Morrish AH, Evans BJ. Magnetic properties of iron-doped manganites. Phys Rev B [Internet]. 1976 May 1;13(9):4069–78. Available from: https://link.aps.org/doi/10.1103/PhysRevB.13.4069

42. Hu B, Krishnan S, Liang C, Heo SJ, Aphale AN, Ramprasad R, et al. Experimental and thermodynamic evaluation of La1−xSrxMnO3±δ and La1−xSrxCo1−yFeyO3−δ cathodes in Cr-containing humidified air. Int J Hydrogen Energy [Internet]. 2017 Apr;42(15):10208–16. Available from: https://linkinghub.elsevier.com/retrieve/pii/S0360319917300605

43. Huo G, Yang Q, Dong F, Song D. Structural, magnetic and electrical transport properties for a series of La1−xSrxFe1−xMnxO3 (0.3≤x≤0.7) compounds. J Alloys Compd [Internet]. 2008 Sep;464(1–2):42–6. Available from: https://linkinghub.elsevier.com/retrieve/pii/S0925838807019846

44. Ahn KH, Wu XW, Liu K, Chien CL. Magnetic properties and colossal magnetoresistance of La(Ca)MnO3 materials doped with Fe. Phys Rev B [Internet]. 1996 Dec 1;54(21):15299–302. Available from: https://link.aps.org/doi/10.1103/PhysRevB.54.15299

45. Chang YL, Huang Q, Ong CK. Effect of Fe doping on the magnetotransport properties in Nd0.67Sr0.33MnO3 manganese oxides. J Appl Phys [Internet]. 2002 Jan 15;91(2):789–93. Available from: http://aip.scitation.org/doi/10.1063/1.1421044

46. Neeraj Kumar, H. Kishan, A. Rao VPSA. Fe ion doping effect on electrical and magnetic properties of La 0.7Ca0.3Mn1-xFexO3 (0 ≤ x ≤ 1). J Alloys Compd. 2010;502:283–8.

47. Arayedh B, Kallel S, Kallel N, Peña O. Influence of non-magnetic and magnetic ions on the MagnetoCaloric properties of La0.7Sr0.3Mn0.9M0.1O3 doped in the Mn sites by M=Cr, Sn, Ti. J Magn Magn Mater [Internet]. 2014;361:68–73. Available from: https://www.sciencedirect.com/science/article/pii/S0304885314001966

48. Bhalodia J, Jadav G, Shah H, Mankadia S, Kanjariya P. Enhanced room temperature magnetoresistance property of co and Ti doped La0.7Sr0.3MnO3. Int J ChemTech Res. 2014 Jan 1;6:2193–6.

49. Rahmouni H, Nouiri M, Jemai R, Kallel N, Rzigua F, Selmi A, et al. Electrical conductivity and complex impedance analysis of 20% Ti-doped La0.7Sr0.3MnO3 perovskite. J Magn Magn Mater [Internet]. 2007;316(1):23–8. Available from: https://www.sciencedirect.com/science/article/pii/S0304885307005409

50. Tong W, Tang Y, Liu X, Zhang Y. Charge-order melting and phase separation in <math display="inline"> <mrow> <msub> <mrow> <mi mathvariant="normal">La</mi> </mrow> <mrow> <mn>0.5</mn> </mrow> </msub> </mrow> <mrow> <msub> <mrow> <mi mathvariant="normal">Ca</mi> </mrow> <mrow> <mn>0.5</mn. Phys Rev B [Internet]. 2003 Oct 21;68(13):134435. Available from: https://link.aps.org/doi/10.1103/PhysRevB.68.134435

51. Aslibeiki B, Kameli P, Salamati H. Reentrant spin glass behavior in La0.8Sr0.2Mn1−xTixO3 manganites. Solid State Commun [Internet]. 2009 Aug;149(31–32):1274–7. Available from: https://linkinghub.elsevier.com/retrieve/pii/S0038109809002750

52. Shang C, Xia ZC, Jin Z, Shi LR, Huang JW, Chen BR, et al. Effect of Ti ion doping on martensitic transition of La0.5Sr0.5Mn1−xTixO3. J Alloys Compd [Internet]. 2014 Mar;588:53–8. Available from: https://linkinghub.elsevier.com/retrieve/pii/S0925838813027606

53. Ben Jemaa F, Mahmood SH, Ellouze M, Hlil EK, Halouani F. Structural, magnetic, magnetocaloric, and critical behavior of selected Ti-doped manganites. Ceram Int [Internet]. 2015 Jul;41(6):8191–202. Available from: https://linkinghub.elsevier.com/retrieve/pii/S0272884215004447

54. Kossi SE, Ghodhbane S, Mnefgui S, Dhahri J, Hlil EK. The impact of disorder on magnetocaloric properties in Ti-doped manganites of La0.7Sr0.25Na0.05Mn(1−x)TixO3

(0≤x≤0.2). J Magn Magn Mater [Internet]. 2015 Dec;395:134–42. Available from: https://linkinghub.elsevier.com/retrieve/pii/S0304885315303577

55. Yang J, Ma YQ, Zhang RL, Zhao BC, Ang R, Song WH, et al. Structural, transport, and magnetic properties in the Ti-doped manganites LaMn1−xTixO3 (0≤x≤0.2). Solid State Commun [Internet]. 2005 Nov;136(5):268–72. Available from: https://linkinghub.elsevier.com/retrieve/pii/S0038109805006927

56. Hébert S, Maignan A, Martin C, Raveau B. Important role of impurity eg levels on the ground state of Mn-site doped manganites. Solid State Commun [Internet]. 2002 Feb;121(5):229–34. Available from: https://linkinghub.elsevier.com/retrieve/pii/S0038109801005130

57. Bourguiba M, Raddaoui Z, Chafra M, Dhahri J. The investigation of structural and vibrational properties and optical behavior of Ti-doped La 0.67 Ba 0.25 Ca 0.08 Mn (1−x) Ti x O 3 (x = 0.00, 0.05 and 0.10) manganites. RSC Adv [Internet]. 2019;9(72):42252–61. Available from: http://xlink.rsc.org/?DOI=C9RA07407D

58. Minh NQ. Solid oxide fuel cell technology—features and applications. Solid State Ionics [Internet]. 2004;174(1):271–7. Available from: https://www.sciencedirect.com/science/article/pii/S0167273804004813

59. Mahato N, Banerjee A, Gupta A, Omar S, Balani K. Progress in material selection for solid oxide fuel cell technology: A review. Prog Mater Sci [Internet]. 2015;72:141–337. Available from: https://www.sciencedirect.com/science/article/pii/S0079642515000195

60. Zhang Y, Gao J, Peng D, Guangyao M, Liu X. Dip-coating thin yttria-stabilized zirconia films for solid oxide fuel cell applications. Ceram Int [Internet]. 2004;30(6):1049–53. Available from: https://www.sciencedirect.com/science/article/pii/S0272884203002384

61. de Arespacochaga N, Valderrama C, Mesa C, Bouchy L, Cortina JL. Biogas deep clean-up based on adsorption technologies for Solid Oxide Fuel Cell applications. Chem Eng J [Internet]. 2014;255:593–603. Available from: https://www.sciencedirect.com/science/article/pii/S1385894714008031

62. Singhal SC. Solid oxide fuel cells for stationary, mobile, and military applications. Solid State Ionics [Internet]. 2002;152–153:405–10. Available from: https://www.sciencedirect.com/science/article/pii/S0167273802003491

63. Singhal SC. Advances in solid oxide fuel cell technology. Solid State Ionics [Internet]. 2000;135(1):305–13. Available from: https://www.sciencedirect.com/science/article/pii/S0167273800004525

64. Sharma RK, Burriel M, Dessemond L, Martin V, Bassat J-M, Djurado E. An innovative architectural design to enhance the electrochemical performance of La2NiO4+δ cathodes for solid oxide fuel cell applications. J Power Sources [Internet]. 2016;316:17–28. Available from: https://www.sciencedirect.com/science/article/pii/S0378775316302816

65. Jacobson AJ. Materials for Solid Oxide Fuel Cells. Chem Mater [Internet]. 2010 Feb 9;22(3):660–74. Available from: https://doi.org/10.1021/cm902640j

66. K Huang JBG. Solid Oxide Fuel Cell Technology: Principles, Performance and Operations. Boca Raton Boston Newyork Washington, DC: Woodhead Publishing Limited, Abigton Hall, Granta Park, Great Abington, Cambridge CB21 6AH, UK; 2009.

67. Kuhn M, Napporn TW. Single-Chamber Solid Oxide Fuel Cell Technology—From Its Origins to Today's State of the Art. Vol. 3, Energies . 2010.

68. Ormerod RM. Solid oxide fuel cells. Chem Soc Rev [Internet]. 2003 Dec 18;32(1):17–28. Available from: http://xlink.rsc.org/?DOI=b105764m

69. Siemons W, Koster G, Blank DHA, Hammond RH, Geballe TH, Beasley MR. Tetragonal CuO: End member of the 3d transition metal monoxides. Phys Rev B [Internet]. 2009 May 22;79(19):195122. Available from: https://link.aps.org/doi/10.1103/PhysRevB.79.195122

70. Salonitis K, Pandremenos J, Paralikas J, Chryssolouris G. Multifunctional materials: engineering applications and processing challenges. Int J Adv Manuf Technol [Internet]. 2010 Jul 17;49(5–8):803–26. Available from: http://link.springer.com/10.1007/s00170-

009-2428-6

71. E D. Nanoscale Phase Separation and Colossal Magnetoresistence The physics of Manganites and Related Compounds. Berlin Heidelberg New York; 2003.

72. Kresin VZ. Manganites. In: Bassani F, Liedl GL, Wyder PBT-E of CMP, editors. Oxford: Elsevier; 2005. p. 261–5. Available from: https://www.sciencedirect.com/science/article/pii/B0123694019011591

73. Bingham NS, Lampen P, Phan MH, Hoang TD, Chinh HD, Zhang CL, et al. Impact of nanostructuring on the magnetic and magnetocaloric properties of microscale phase-separated (La,Pr,Ca)MnO3 manganites. Phys Rev B [Internet]. 2012 Aug 16;86(6):064420. Available from: https://link.aps.org/doi/10.1103/PhysRevB.86.064420

74. Lau HK, Leung CW. Nonvolatile multilevel memory effect by resistive switching in manganite thin films. J Appl Phys [Internet]. 2008 Dec 15;104(12):123705. Available from: http://aip.scitation.org/doi/10.1063/1.3043801

75. Levy P, Parisi F, Granja L, Indelicato E, Polla G. Novel Dynamical Effects and Persistent Memory in Phase Separated Manganites. Phys Rev Lett [Internet]. 2002 Sep 4;89(13):137001. Available from: https://link.aps.org/doi/10.1103/PhysRevLett.89.137001

76. Zener C. Interaction Between the d-Shells in the Transition Metals. Phys Rev [Internet]. 1951 Feb 1;81(3):440–4. Available from: https://link.aps.org/doi/10.1103/PhysRev.81.440

77. Jonker GH, Van Santen JH. Ferromagnetic compounds of manganese with perovskite structure. Physica [Internet]. 1950 Mar;16(3):337–49. Available from: https://linkinghub.elsevier.com/retrieve/pii/0031891450900334

78. Van Santen JH, Jonker GH. Electrical conductivity of ferromagnetic compounds of manganese with perovskite structure. Physica [Internet]. 1950 Jul;16(7–8):599–600. Available from: https://linkinghub.elsevier.com/retrieve/pii/0031891450901042

79. Volger J. Further experimental investigations on some ferromagnetic oxidic compounds of manganese with perovskite structure. Physica [Internet]. 1954;20(1):49–66. Available from: https://www.sciencedirect.com/science/article/pii/S0031891454800152

80. Wollan EO, Koehler WC. Neutron Diffraction Study of the Magnetic Properties of the Series of Perovskite-Type Compounds $[(1\ensuremath{-}x)\mathrm{La}, x\mathrm{Ca}]\mathrm{Mn}{\mathrm{O}}_{3}$. Phys Rev [Internet]. 1955 Oct 15;100(2):545–63. Available from: https://link.aps.org/doi/10.1103/PhysRev.100.545

81. Searle CW, Wang ST. Studies of the ionic ferromagnet (LaPb)MnO 3 III. Ferromagnetic resonance studies. Can J Phys [Internet]. 1969 Dec 1;47(23):2703–8. Available from: http://www.nrcresearchpress.com/doi/10.1139/p69-329

82. Searle CW, Wang ST. Studies of the ionic ferromagnet (LaPb)MnO 3 . V. Electric transport and ferromagnetic properties. Can J Phys [Internet]. 1970 Sep 1;48(17):2023–31. Available from: http://www.nrcresearchpress.com/doi/10.1139/p70-257

83. Morrish AH, Evans BJ, Eaton JA, Leung LK. Studies of the ionic ferromagnet (LaPb)MnO 3 I. Growth and characteristics of single crystals. Can J Phys [Internet]. 1969 Dec 1;47(23):2691–6. Available from: http://www.nrcresearchpress.com/doi/10.1139/p69-327

84. Leung LK, Morrish AH, Searle CW. Studies of the ionic ferromagnet (LaPb)MnO 3 II. Static magnetization properties from 0 to 800 °K. Can J Phys [Internet]. 1969 Dec 1;47(23):2697–702. Available from: http://www.nrcresearchpress.com/doi/10.1139/p69-328

85. Goodenough JB. and Longo JM. Crystallographic and Magnetic Properties of Perovskites and Perovskite-Related Compounds. Vol. III/4a. in Landolt-Bornstein Tabellen, Berlin: Springer; 1970.

86. von Helmolt R, Wecker J, Holzapfel B, Schultz L, Samwer K. Giant negative magnetoresistance in perovskitelike La2/3Ba1/3MnOx ferromagnetic films. Phys Rev Lett [Internet]. 1993 Oct 4;71(14):2331–3. Available from: https://link.aps.org/doi/10.1103/PhysRevLett.71.2331

87. Chahara K, Ohno T, Kasai M, Kozono Y. Magnetoresistance in magnetic manganese oxide with intrinsic antiferromagnetic spin structure. Appl Phys Lett [Internet]. 1993 Oct 4;63(14):1990–2. Available from: http://aip.scitation.org/doi/10.1063/1.110624

88. McCormack M, Jin S, Tiefel TH, Fleming RM, Phillips JM, Ramesh R. Very large magnetoresistance in perovskite-like La-Ca-Mn-O thin films. Appl Phys Lett [Internet]. 1994 May 30;64(22):3045–7. Available from: http://aip.scitation.org/doi/10.1063/1.111372

89. Jin S, Tiefel TH, McCormack M, Fastnacht RA, Ramesh R, Chen LH. Thousandfold Change in Resistivity in Magnetoresistive La-Ca-Mn-O Films. Science (80-) [Internet]. 1994 Apr 15;264(5157):413–5. Available from: https://www.sciencemag.org/lookup/doi/10.1126/science.264.5157.413

90. Imada M, Fujimori A, Tokura Y. Metal-insulator transitions. Rev Mod Phys [Internet]. 1998;70(4):1039–263. Available from: https://link.aps.org/doi/10.1103/RevModPhys.70.1039

91. Coey JMD, Viret M, Ranno L, Ounadjela K. Electron Localization in Mixed-Valence Manganites. Phys Rev Lett [Internet]. 1995 Nov 20;75(21):3910–3. Available from: https://link.aps.org/doi/10.1103/PhysRevLett.75.3910

92. Salamon MB, Chun SH. Griffiths singularities and magnetoresistive manganites. Phys Rev B [Internet]. 2003 Jul 9;68(1):14411. Available from: https://link.aps.org/doi/10.1103/PhysRevB.68.014411

93. Salamon MB, Jaime M. The physics of manganites: Structure and transport. Rev Mod Phys [Internet]. 2001 Aug 29;73(3):583–628. Available from: https://link.aps.org/doi/10.1103/RevModPhys.73.583

94. Dagotto E. Nanoscale Phase Separation and Colossal Magnetoresistance The Physics of Manganites and Related Compounds. Verlag Berlin Heidelberg New York: Springer; 2003.

95. Y Tokura. Colossal magnetoresistive oxides. Advances i. Amsterdam, The Netherlands : Gordon and Breach Science Publishers; 2000.

96. Tokura Y. Critical features of colossal magnetoresistive manganites. Reports Prog Phys [Internet]. 2006;69(3):797–851. Available from: http://dx.doi.org/10.1088/0034-4885/69/3/R06

97. Siwach PK, Singh HK, Srivastava ON. Low field magnetotransport in manganites. J Phys Condens Matter [Internet]. 2008 Jul 9;20(27):273201. Available from: https://iopscience.iop.org/article/10.1088/0953-8984/20/27/273201

98. Peter E. Blöchl. Quantum Mechanics of the Chemical Bond. TU Clausthal; 2014. 242 p.

99. A. Mozhegorov, A. V. Larin AEN. The Phys. Met. Metallorg. 2008.

100. Goldschmidt VM. Die Gesetze der Krystallochemie. Naturwissenschaften [Internet]. 1926 May;14(21):477–85. Available from: http://link.springer.com/10.1007/BF01507527

101. Li C, Soh KCK, Wu P. Formability of ABO3 perovskites. J Alloys Compd [Internet]. 2004 Jun;372(1–2):40–8. Available from: https://linkinghub.elsevier.com/retrieve/pii/S0925838803011460

102. Coey JMD, Viret M, von Molnár S. Mixed-valence manganites. Adv Phys [Internet]. 1999 Mar;48(2):167–293. Available from: http://www.tandfonline.com/doi/abs/10.1080/000187399243455

103. Shannon RD. Revised effective ionic radii and systematic studies of interatomic distances in halides and chalcogenides. Acta Crystallogr Sect A [Internet]. 1976 Sep 1;32(5):751–67. Available from: http://scripts.iucr.org/cgi-bin/paper?S0567739476001551

104. Moshnyaga V, Damaschke B, Shapoval O, Belenchuk A, Faupel J, Lebedev OI, et al. Structural phase transition at the percolation threshold in epitaxial (La0.7Ca0.3MnO3)1–x:(MgO)x nanocomposite films. Nat Mater [Internet]. 2003;2(4):247–52. Available from: https://doi.org/10.1038/nmat859

105. Ramanathan S. Thin Film Metal-Oxides Fundamentals and Applications in Electronics and Energy. New York Dordrecht: Harvard University: Springer; 2010.

106. Hemberger J, Krimmel A, Kurz T, Krug von Nidda H-A, Ivanov VY, Mukhin AA, et al. Structural, magnetic, and electrical properties of single-crystalline La1−xSrxMnO3(0.4<x<0.85). Phys Rev B [Internet]. 2002 Sep 11;66(9):094410. Available from: https://link.aps.org/doi/10.1103/PhysRevB.66.094410

107. Liao Z, Zhang J. Metal-to-Insulator Transition in Ultrathin Manganite Heterostructures. Vol. 9, Applied Sciences . 2019.

108. Xu P, Huffman T J, Branagan N C, Qazilbash M M SP, Goehringer T, Yong G SV and KR. Novel aspects of charge and lattice dynamics in the hole-doped manganite La0.67Sr0.33MnO3. Philos Mag 95 2078. 2015;

109. Zener C. Interaction between the d-Shells in the Transition Metals. III. Calculation of the Weiss Factors in Fe, Co, and Ni. Phys Rev [Internet]. 1951 Jul 15;83(2):299–301. Available from: https://link.aps.org/doi/10.1103/PhysRev.83.299

110. Siwach PK, Singh HK, Srivastava ON. Low field magnetotransport in manganites. J Phys Condens Matter [Internet]. 2008;20(27):273201. Available from: http://dx.doi.org/10.1088/0953-8984/20/27/273201

111. de Gennes P-G. Effects of Double Exchange in Magnetic Crystals. Phys Rev [Internet]. 1960 Apr 1;118(1):141–54. Available from: https://link.aps.org/doi/10.1103/PhysRev.118.141

112. Millis AJ. Lattice effects in magnetoresistive manganese perovskites. Nature [Internet]. 1998 Mar;392(6672):147–50. Available from: http://www.nature.com/articles/32348

113. Dagotto E, Hotta T, Moreo A. Colossal magnetoresistant materials: the key role of phase separation. Phys Rep [Internet]. 2001;344(1):1–153. Available from: https://www.sciencedirect.com/science/article/pii/S0370157300001216

114. N. Tsuda, K. Nasu AF and KS. Electronic conduction in oxides,. 2nd editio. Verlag Berlin Heidelberg New York: Springer; 2000.

115. Tokura, Y. NN. Orbital Physics in Transition-Metal Oxides. Science (80-) [Internet]. 2000 Apr 21;288(5465):462–8. Available from: https://www.sciencemag.org/lookup/doi/10.1126/science.288.5465.462

116. Orbach R and Stapleton HJE. Spin-Lattice Relaxation Electron Paramagnetic Resonance. (Ed.) SG, editor. Plenum, New York; 1972.

117. Kanamori J. Crystal Distortion in Magnetic Compounds. J Appl Phys [Internet]. 1960 May;31(5):S14–23. Available from: http://aip.scitation.org/doi/10.1063/1.1984590

118. Kramers HA. L'interaction Entre les Atomes Magnétogènes dans un Cristal Paramagnétique. Physica [Internet]. 1934;1(1):182–92. Available from: https://www.sciencedirect.com/science/article/pii/S0031891434900239

119. Goodenough JB. Metallic oxides. Prog Solid State Chem [Internet]. 1971;5:145–399. Available from: https://www.sciencedirect.com/science/article/pii/0079678671900185

120. Millis AJ. Cooperative Jahn-Teller effect and electron-phonon coupling in La1-xAxMnO3. Phys Rev B [Internet]. 1996 Apr 1;53(13):8434–41. Available from: https://link.aps.org/doi/10.1103/PhysRevB.53.8434

121. A. J. Millis BIS and RM. Dynamic jahn–teller effect and colossal magnetoresistance in La1−xSrxMnO3. Phys Rev Lett. 1996;77:175.

122. Rifai D, Abdalla AN, Ali K, Razali R. Giant Magnetoresistance Sensors: A Review on Structures and Non-Destructive Eddy Current Testing Applications. Vol. 16, Sensors . 2016.

123. Baibich MN, Broto JM, Fert A, Van Dau FN, Petroff F, Etienne P, et al. Giant Magnetoresistance of (001)Fe/(001)Cr Magnetic Superlattices. Phys Rev Lett [Internet]. 1988 Nov 21;61(21):2472–5. Available from: https://link.aps.org/doi/10.1103/PhysRevLett.61.2472

124. Ganguly R, Gopalakrishnan IK, Yakhmi J V. Magnetic and electrical properties of La0.67Ca0.33MnO3 as influenced by substitution of Cr. Phys B Condens Matter [Internet]. 2000;275(4):308–15. Available from: https://www.sciencedirect.com/science/article/pii/S0921452699008558

125. Anoop C. Sreekantan BG. Magnetic sensors and industrial sensing applications. 2018.

126. Julliere M. Tunneling between ferromagnetic films. Phys Lett A [Internet]. 1975;54(3):225–6. Available from: https://www.sciencedirect.com/science/article/pii/0375960175901747

127. Asamitsu A, Tomioka Y, Kuwahara H, Tokura Y. Current switching of resistive states in magnetoresistive manganites. Nature [Internet]. 1997;388(6637):50–2. Available from: https://doi.org/10.1038/40363

128. De Teresa JM, Barthélémy A, Fert A, Contour JP, Lyonnet R, Montaigne F, et al. Inverse Tunnel Magnetoresistance in Co/SrTiO3/La0.7Sr0.3MnO3 New Ideas on Spin-Polarized Tunneling. Phys Rev Lett [Internet]. 1999 May 24;82(21):4288–91. Available from: https://link.aps.org/doi/10.1103/PhysRevLett.82.4288

129. De Teresa JM, Barthélémy A, Fert A, Contour JP, Montaigne F, Seneor P. Role of Metal-Oxide Interface in Determining the Spin Polarization of Magnetic Tunnel Junctions. Science (80-) [Internet]. 1999 Oct 15;286(5439):507–9. Available from: https://www.sciencemag.org/lookup/doi/10.1126/science.286.5439.507

130. Kokado S, Tsunoda M. Intuitive explanation of Anisotropic Magnetoresistance (AMR) effect and necessary condition for half-metallic ferromagnet 'negative AMR' (Conference Presentation). In: Jaffrès H, Drouhin H-J, Wegrowe J-E, Razeghi M, editors. Spintronics XI [Internet]. SPIE; 2018. p. 115. Available from: https://spiedigitallibrary.org/conference-proceedings-of-spie/10732/2320021/Intuitive-explanation-of-Anisotropic-Magnetoresistance-AMR-effect-and-necessary-condition/10.1117/12.2320021.full

131. Ziese M. Extrinsic magnetotransport phenomena in ferromagnetic oxides. Reports Prog Phys [Internet]. 2002;65(2):143–249. Available from: http://dx.doi.org/10.1088/0034-4885/65/2/202

132. Campbell IA, Fert A, Jaoul O. The spontaneous resistivity anisotropy in Ni-based alloys. J Phys C Solid State Phys [Internet]. 1970;3(1S):S95–101. Available from: http://dx.doi.org/10.1088/0022-3719/3/1S/310

133. McGuire T, Aboaf J, Klokholm E. Negative anisotropic magnetoresistance in 3d metals and alloys containing iridium. IEEE Trans Magn [Internet]. 1984 Sep;20(5):972–4. Available from: http://ieeexplore.ieee.org/document/1063188/

134. Du Y, Xu GZ, Liu EK, Li GJ, Zhang HG, Yu SY, et al. Half-metallicity and anisotropy magnetoresistance properties of Heusler alloys Fe2Co1−xCrxSi. J Magn Magn Mater [Internet]. 2013 Jun;335:101–4. Available from: https://linkinghub.elsevier.com/retrieve/pii/S030488531300070X

135. Kokado S, Tsunoda M. Theoretical Study on Anisotropic Magnetoresistance Effects of I // [100], I // [110], and I // [001] for Ferromagnets with a Crystal Field of Tetragonal Symmetry. J Phys Soc Japan [Internet]. 2019 Mar 15;88(3):034706. Available from: https://journals.jps.jp/doi/10.7566/JPSJ.88.034706

136. Kokado S, Tsunoda M, Harigaya K, Sakuma A. Anisotropic Magnetoresistance Effects in Fe, Co, Ni, Fe 4 N, and Half-Metallic Ferromagnet: A Systematic Analysis. J Phys Soc Japan [Internet]. 2012 Feb 15;81(2):024705. Available from: https://journals.jps.jp/doi/10.1143/JPSJ.81.024705

137. Kokado S, Tsunoda M. Anisotropic Magnetoresistance Effect: General Expression of AMR Ratio and Intuitive Explanation for Sign of AMR Ratio. Adv Mater Res [Internet]. 2013;750–752:978–82. Available from: https://www.scientific.net/AMR.750-752.978

138. Solin SA. Enhanced Room-Temperature Geometric Magnetoresistance in Inhomogeneous Narrow-Gap Semiconductors. Science (80-) [Internet]. 2000 Sep 1;289(5484):1530–2. Available from: https://www.sciencemag.org/lookup/doi/10.1126/science.289.5484.1530

139. Hewett TH, Kusmartsev F V. Geometrically enhanced extraordinary magnetoresistance in

semiconductor-metal hybrids. Phys Rev B [Internet]. 2010 Dec 13;82(21):212404. Available from: https://link.aps.org/doi/10.1103/PhysRevB.82.212404

140. Sun J, Kosel J. Extraordinary Magnetoresistance in Semiconductor/Metal Hybrids: A Review. Materials (Basel) [Internet]. 2013 Feb 13;6(2):500–16. Available from: http://www.mdpi.com/1996-1944/6/2/500

141. Kusters RM, Singleton J, Keen DA, McGreevy R, Hayes W. Magnetoresistance measurements on the magnetic semiconductor Nd0.5Pb0.5MnO3. Phys B Condens Matter [Internet]. 1989 Mar;155(1–3):362–5. Available from: https://linkinghub.elsevier.com/retrieve/pii/0921452689905309

142. Snyder GJ, Hiskes R, DiCarolis S, Beasley MR, Geballe TH. Intrinsic electrical transport and magnetic properties of La0.67Ca0.33MnO3 and La0.67Sr0.33MnO3 MOCVD thin films and bulk material. Phys Rev B [Internet]. 1996 Jun 1;53(21):14434–44. Available from: https://link.aps.org/doi/10.1103/PhysRevB.53.14434

143. Viret M, Ranno L, Coey JMD. Magnetic localization in mixed-valence manganites. Phys Rev B [Internet]. 1997 Apr 1;55(13):8067–70. Available from: https://link.aps.org/doi/10.1103/PhysRevB.55.8067

144. Emin D, Holstein T. Adiabatic Theory of an Electron in a Deformable Continuum. Phys Rev Lett [Internet]. 1976 Feb 9;36(6):323–6. Available from: https://link.aps.org/doi/10.1103/PhysRevLett.36.323

145. N F Mott. Conduction in non-crystalline materials. second edi. Oxford : Clarendon Press; 1993.

146. Mott NF. Conduction in glasses containing transition metal ions. J Non Cryst Solids [Internet]. 1968;1(1):1–17. Available from: https://www.sciencedirect.com/science/article/pii/0022309368900021

147. Sun Y, Xu X, Zhang Y. Variable-range hopping of small polarons in mixed-valence manganites. J Phys Condens Matter [Internet]. 2000;12(50):10475–80. Available from: http://dx.doi.org/10.1088/0953-8984/12/50/309

148. Ahmed H, Khan S, Khan W, Nongjai R, Khan I. Adiabatic to non adiabatic change in conduction mechanism of Zn doped La0.67Sr0.33MnO3 perovskite. J Alloys Compd [Internet]. 2013;563:12–7. Available from: https://www.sciencedirect.com/science/article/pii/S0925838813002648

149. Denbri F, Mahamdioua N, Meriche F, Koc NS, Terzioglu C, Varilci A, et al. A-site Pb doping effect on structural, microstructural and magnetotransport properties of La0.5Sm0.2Ca0.3-xPbxMnO3 (x=0, 0.05, 0.10) manganite. Mater Chem Phys [Internet]. 2021;267:124550. Available from: https://www.sciencedirect.com/science/article/pii/S0254058421003333

150. Ravi S, Kar M. Study of magneto-resistivity in La1−xAgxMnO3 compounds. Phys B Condens Matter [Internet]. 2004;348(1):169–76. Available from: https://www.sciencedirect.com/science/article/pii/S0921452603011475

151. AS Alexandrov NM. Polarons and bipolarons. 1996.

152. Kalyana Lakshmi Y, Manjunathrao S, Venugopal Reddy P. Influence of rare-earth ion doping on magnetotransport behavior of potassium doped manganites. Mater Chem Phys [Internet]. 2014 Feb;143(3):983–90. Available from: https://linkinghub.elsevier.com/retrieve/pii/S0254058413007803

153. Snyder GJ, Hiskes R, DiCarolis S, Beasley MR, Geballe TH. Intrinsic electrical transport and magnetic properties of La0.67Ca0.33MnO3 and La0.67Sr0.33MnO3 MOCVD thin films and bulk material. Phys Rev B [Internet]. 1996 Jun 1;53(21):14434–44. Available from: https://link.aps.org/doi/10.1103/PhysRevB.53.14434

154. De Teresa JM, Ibarra MR, Blasco J, García J, Marquina C, Algarabel PA, et al. Spontaneous behavior and magnetic field and pressure effects on La2/3Ca1/3MnO3 perovskite. Phys Rev B [Internet]. 1996 Jul 1;54(2):1187–93. Available from: https://link.aps.org/doi/10.1103/PhysRevB.54.1187

155. G. V, Paduru VR. Electrical behavior of sol-gel prepared Nd0.67Sr0.33MnO3 manganite system. J Magn Magn Mater. 2005 Jan 31;285:343–52.

156. Zhang J, Xu Y, Cao S, Cao G, Zhang Y, Jing C. Kondo-like transport and its correlation with the spin-glass phase in perovskite manganites. Phys Rev B [Internet]. 2005 Aug 4;72(5):54410. Available from: https://link.aps.org/doi/10.1103/PhysRevB.72.054410

157. Urushibara A, Moritomo Y, Arima T, Asamitsu A, Kido G, Tokura Y. Insulator-metal transition and giant magnetoresistance in La1-xSrxMnO3. Phys Rev B Condens Matter. 1995 May;51(20):14103–9.

158. Furukawa N. Unconventional One-Magnon Scattering Resistivity in Half-Metals. J Phys Soc Japan [Internet]. 2000 Jul 15;69(7):1954–7. Available from: http://journals.jps.jp/doi/10.1143/JPSJ.69.1954

159. Li J, Ong CK, Zhan Q, Li DX. Microstructure and inter-grain magnetoresistance in Ag-doped polycrystalline La0.67Sr0.33MnO3 thin films. J Phys Condens Matter [Internet]. 2002;14(25):6341–51. Available from: http://dx.doi.org/10.1088/0953-8984/14/25/304

160. Huang Q, Li ZW, Li J, Ong CK. The magnetic, electrical transport and magnetoresistance properties of epitaxial La0.7Sr0.3Mn1-xFexO3(x= 0-0.20) thin films prepared by pulsed laser deposition. J Phys Condens Matter [Internet]. 2001;13(18):4033–47. Available from: http://dx.doi.org/10.1088/0953-8984/13/18/312

161. Kubo K, Ohata N. A Quantum Theory of Double Exchange. I. J Phys Soc Japan [Internet]. 1972 Jul;33(1):21–32. Available from: https://journals.jps.jp/doi/10.1143/JPSJ.33.21

162. Cullity BD. Elements of X-Ray Diffraction. 2nd Editio. Phillippines: Addison-Wesley Publishing Company Inc.; 1978.

163. Warren B. X-Ray Diffraction. Addison-Wesley, Reading, MA; 1969.

164. Keithley Instruments Inc., Handbook on Low Level Measurements, 6th Edn. 2004;

165. Dogruer M, Yildirim G, Ozturk O, Terzioglu C. Analysis of Indentation Size Effect on Mechanical Properties of Cu-Diffused Bulk MgB2 Superconductor Using Experimental and Different Theoretical Models. J Supercond Nov Magn [Internet]. 2013 Jan 20;26(1):101–9. Available from: http://link.springer.com/10.1007/s10948-012-1719-6

166. Gaur A, Varma GD. Sintering temperature effect on electrical transport and magnetoresistance of nanophasic La0.7Sr0.3MnO3. J Phys Condens Matter [Internet]. 2006;18(39):8837–46. Available from: http://dx.doi.org/10.1088/0953-8984/18/39/014

167. Klie RF, Zheng JC, Zhu Y, Varela M, Wu J, Leighton C. Direct Measurement of the Low-Temperature Spin-State Transition in LaCoO3. Phys Rev Lett [Internet]. 2007 Jul 25;99(4):047203. Available from: https://link.aps.org/doi/10.1103/PhysRevLett.99.047203

168. J. A. Bhalodia*, G. D. Jadav, H. D. Shah, S. R. Mankadia PVK. Enhanced Room Temperature Magnetoresistance Property of Co and Ti Doped La0.7Sr0.3MnO3. Int J ChemTech Res. 2014;6(0974–4290):2193–6.

169. Cullity, B.D., Stock SR. Elements of X-ray diffraction. vol 3. Prentice hall New Jersey; 2001. chapter 5, 174.

170. Schneider CA, Rasband WS, Eliceiri KW. NIH Image to ImageJ: 25 years of image analysis. Nat Methods [Internet]. 2012 Jul 28;9(7):671–5. Available from: http://www.nature.com/articles/nmeth.2089

171. Punith Kumar V, Dayal V, Hadimani RL, Bhowmik RN, Jiles DC. Magnetic and electrical properties of Ti-substituted lanthanum bismuth manganites. J Mater Sci [Internet]. 2015 May 3;50(10):3562–75. Available from: http://link.springer.com/10.1007/s10853-015-8916-1

172. Souza AD, Rayaprol S, Murari MS, Daivajna M. Effect of milling on structure and magnetism of nanocrystalline La0.7-xBixSr0.3MnO3 (x = 0.35, 0.40) manganites. Phys B Condens Matter [Internet]. 2021;606:412792. Available from: https://www.sciencedirect.com/science/article/pii/S0921452620307651

173. Schiffer P, Ramirez AP, Bao W, Cheong S-W. Low Temperature Magnetoresistance and

the Magnetic Phase Diagram of La1−xCaxMnO3. Phys Rev Lett [Internet]. 1995 Oct 30;75(18):3336–9. Available from: https://link.aps.org/doi/10.1103/PhysRevLett.75.3336

174. Hwang HY, Cheong S-W, Ong NP, Batlogg B. Spin-Polarized Intergrain Tunneling in La2/3Sr1/3MnO3. Phys Rev Lett [Internet]. 1996 Sep 2;77(10):2041–4. Available from: https://link.aps.org/doi/10.1103/PhysRevLett.77.2041

175. Kallel N, Fröhlich K, Pignard S, Oumezzine M, Vincent H. Structure, magnetic and magnetoresistive properties of La0.7Sr0.3Mn1−xSnxO3 samples (0≤x≤0.20). J Alloys Compd [Internet]. 2005 Aug;399(1–2):20–6. Available from: https://linkinghub.elsevier.com/retrieve/pii/S0925838805002471

176. Moualhi Y, M'nassri R, Rahmouni H, Gassoumi M, Khirouni K. Possibility of controlling the conduction mechanism by choosing a specific doping element in a praseodymium manganite system. RSC Adv [Internet]. 2020;10(56):33868–78. Available from: http://xlink.rsc.org/?DOI=D0RA03982A

177. M'nassri R, Khelifi M, Rahmouni H, Selmi A, Khirouni K, Chniba-Boudjada N, et al. Study of physical properties of cobalt substituted Pr0.7Ca0.3MnO3 ceramics. Ceram Int [Internet]. 2016 Apr;42(5):6145–53. Available from: https://linkinghub.elsevier.com/retrieve/pii/S0272884216000249

178. Sun T, Ji F, Liu Y, Dong G, Zhang S, Chen Q, et al. La1-Sr MnO3:Ag0.2 ($0.1 \leq x \leq 0.2$) ceramics with large room-temperature TCR for uncooled infrared bolometers. J Eur Ceram Soc [Internet]. 2019 Feb;39(2–3):352–7. Available from: https://linkinghub.elsevier.com/retrieve/pii/S0955221918306198

179. Perna P, Maccariello D, Ajejas F, Guerrero R, Méchin L, Flament S, et al. Engineering Large Anisotropic Magnetoresistance in La 0.7 Sr 0.3 MnO 3 Films at Room Temperature. Adv Funct Mater [Internet]. 2017 Jul;27(26):1700664. Available from: https://onlinelibrary.wiley.com/doi/10.1002/adfm.201700664

180. Lukose R, Zurauskiene N, Stankevic V, Vagner M, Plausinaitiene V, Niaura G, et al. Room temperature Co-doped manganite/graphene sensor operating at high pulsed magnetic fields. Sci Rep [Internet]. 2019 Dec 1;9(1):9497. Available from: http://www.nature.com/articles/s41598-019-46012-2

181. Mahamdioua N, Amira A, Boudjadja Y, Saoudel A, Altintas SP, Varilci A, et al. Magneto-conductive mechanisms in the La-site doped double-layered La1.4Ca1.6Mn2O7 manganites. Phys B Condens Matter [Internet]. 2016 Nov;500:77–84. Available from: https://linkinghub.elsevier.com/retrieve/pii/S0921452616302897

182. Urushibara A, Moritomo Y, Arima T, Asamitsu A, Kido G, Tokura Y. Insulator-metal transition and giant magnetoresistance in La1−xSrxMnO3. Phys Rev B [Internet]. 1995 May 15;51(20):14103–9. Available from: https://link.aps.org/doi/10.1103/PhysRevB.51.14103

183. Kalyana Lakshmi Y, Venugopal Reddy P. Electrical behavior of some silver-doped lanthanum-based CMR materials. J Magn Magn Mater [Internet]. 2009;321(9):1240–5. Available from: https://www.sciencedirect.com/science/article/pii/S0304885308011554

184. Graziosi P, Gambardella A, Prezioso M, Riminucci A, Bergenti I, Homonnay N, et al. Polaron framework to account for transport properties in metallic epitaxial manganite films. Phys Rev B [Internet]. 2014 Jun 12;89(21):214411. Available from: https://link.aps.org/doi/10.1103/PhysRevB.89.214411

185. Venkataiah G, Krishna DC, Vithal M, Rao SS, Bhat S V, Prasad V, et al. Effect of sintering temperature on electrical transport properties of La0.67Ca0.33MnO3. Phys B Condens Matter [Internet]. 2005;357(3):370–9. Available from: https://www.sciencedirect.com/science/article/pii/S0921452604012414

186. Ogale SB, Shreekala R, Bathe R, Date SK, Patil SI, Hannoyer B, et al. Transport properties, magnetic ordering, and hyperfine interactions in Fe-doped La0.75Ca0.25MnO3: Localization-delocalization transition. Phys Rev B [Internet]. 1998 Apr 1;57(13):7841–5. Available from: https://link.aps.org/doi/10.1103/PhysRevB.57.7841

187. Mahjoub S, Baazaoui M, M'nassri R, Rahmouni H, Boudjada NC, Oumezzine M. Effect

of iron substitution on the structural, magnetic and magnetocaloric properties of Pr0.6Ca0.1Sr0.3Mn1−xFexO3 (0⩽x⩽0.075) manganites. J Alloys Compd [Internet]. 2014 Sep;608:191–6. Available from: https://linkinghub.elsevier.com/retrieve/pii/S0925838814009384

188. Wang GF, Zhao ZR, Li HL, Zhang XF. Magnetocaloric effect and critical behavior in Fe-doped La0.67Sr0.33Mn1−Fe O3 manganites. Ceram Int [Internet]. 2016 Dec;42(16):18196–203. Available from: https://linkinghub.elsevier.com/retrieve/pii/S0272884216314481

189. Suryanarayana C, Norton MG. X-Ray Diffraction [Internet]. Boston, MA: Springer US; 1998. Available from: http://link.springer.com/10.1007/978-1-4899-0148-4

190. Qamhieh N, Najar A, Qamhieh ZN, Abdel Aziz B, Mansour A, Alghoul I. Synthesis and characterization of a perovskite film for solar cells applications. Optik (Stuttg) [Internet]. 2018 Oct;171:648–51. Available from: https://linkinghub.elsevier.com/retrieve/pii/S0030402618307150

191. Dhilip M, Devi NA, Punitha JS, Anbarasu V, Kumar KS. Conventional synthesis and characterization of cubically ordered La2FeMnO6 double perovskite compound. Vacuum [Internet]. 2019 Sep;167:16–20. Available from: https://linkinghub.elsevier.com/retrieve/pii/S0042207X1930627X

192. Xavier MM, Cabral FAO, de Araújo JH, Chesman C, Dumelow T. Magnetic and transport properties of polycrystalline La0.7Sr0.3Mn1−xFexO3. Phys Rev B [Internet]. 2000 Dec 12;63(1):12408. Available from: https://link.aps.org/doi/10.1103/PhysRevB.63.012408

193. RAO CNR, RAYCHAUDHURI AK. COLOSSAL MAGNETORESISTANCE, CHARGE ORDERING AND OTHER NOVEL PROPERTIES OF MANGANATES AND RELATED MATERIALS. In: Colossal Magnetoresistance, Charge Ordering and Related Properties of Manganese Oxides [Internet]. WORLD SCIENTIFIC; 1998. p. 1–42. Available from: http://www.worldscientific.com/doi/abs/10.1142/9789812816795_0001

194. Booth CH, Bridges F, Kwei GH, Lawrence JM, Cornelius AL, Neumeier JJ. Direct Relationship between Magnetism and La1−xCaxMnO3. Phys Rev Lett [Internet]. 1998 Jan 26;80(4):853–6. Available from: https://link.aps.org/doi/10.1103/PhysRevLett.80.853

195. De Teresa JM, Dörr K, Müller KH, Schultz L, Chakalova RI. Strong influence of the Mn3+ content on the binding energy of the lattice polarons in manganese perovskites. Phys Rev B [Internet]. 1998 Sep 1;58(10):R5928–31. Available from: https://link.aps.org/doi/10.1103/PhysRevB.58.R5928

196. Li R, Wang Z, Chen X, Sun J, Shen B, Yan C. Magnetic properties and colossal magnetoresistance of the perovskites La2/3Ca1/3Mn1−xTixO3. J Appl Phys [Internet]. 2000 May;87(9):5597–9. Available from: http://aip.scitation.org/doi/10.1063/1.372462

197. Tozri A, Dhahri E. Structural and magnetotransport properties of (La, Pr)-Ba manganites. J Alloys Compd [Internet]. 2019;783:718–28. Available from: https://www.sciencedirect.com/science/article/pii/S0925838818348515

198. Kuberkar DG, Doshi RR, Solanki PS, Khachar U, Vagadia M, Ravalia A, et al. Grain morphology and size disorder effect on the transport and magnetotransport in Sol–Gel grown nanostructured manganites. Appl Surf Sci [Internet]. 2012 Sep;258(22):9041–6. Available from: https://linkinghub.elsevier.com/retrieve/pii/S0169433212010082

199. De Teresa JM, Ibarra MR, Blasco J, García J, Marquina C, Algarabel PA, et al. Spontaneous behavior and magnetic field and pressure effects on La/2/3Ca1/3MnO3 perovskite. Phys Rev B [Internet]. 1996 Jul 1;54(2):1187–93. Available from: https://link.aps.org/doi/10.1103/PhysRevB.54.1187

200. Zhang J, Xu Y, Cao S, Cao G, Zhang Y, Jing C. Kondo-like transport and its correlation with the spin-glass phase in perovskite manganites. Phys Rev B [Internet]. 2005 Aug 4;72(5):054410. Available from: https://link.aps.org/doi/10.1103/PhysRevB.72.054410

201. Viret M, Ranno L, Coey JMD. Magnetic localization in mixed-valence manganites. Phys Rev B [Internet]. 1997 Apr 1;55(13):8067–70. Available from: https://link.aps.org/doi/10.1103/PhysRevB.55.8067

202. Lalitha G, Reddy PV. Low temperature resistivity anomalies in bismuth doped manganites. J Alloys Compd [Internet]. 2010 Apr;494(1–2):476–82. Available from: https://linkinghub.elsevier.com/retrieve/pii/S0925838810001222

203. Banerjee A, Pal S, Bhattacharya S, Chaudhuri BK, Yang HD. Particle size and magnetic field dependent resistivity and thermoelectric power of La0.5Pb0.5MnO3 above and below metal–insulator transition. J Appl Phys [Internet]. 2002 Apr 15;91(8):5125–34. Available from: http://aip.scitation.org/doi/10.1063/1.1459618

204. Millis AJ, Littlewood PB, Shraiman BI. Double Exchange Alone Does Not Explain the Resistivity of La1−xSrxMnO3. Phys Rev Lett [Internet]. 1995 Jun 19;74(25):5144–7. Available from: https://link.aps.org/doi/10.1103/PhysRevLett.74.5144

205. Goodenough JB, Zhou J-S. New forms of phase segregation. Nature [Internet]. 1997 Mar;386(6622):229–30. Available from: http://www.nature.com/articles/386229a0

206. Mott NF. Metal-insulator transitions. Contemp Phys [Internet]. 1973 Sep;14(5):401–13. Available from: http://www.tandfonline.com/doi/abs/10.1080/00107517308210764

207. Barik SK, Mahendiran R. Effect of Bi doping on magnetic and magnetocaloric properties of La0.7−xBixSr0.3MnO3 ($0 \leq x \leq 0.4$). J Appl Phys [Internet]. 2010 May;107(9):093906. Available from: http://aip.scitation.org/doi/10.1063/1.3407523

208. Auslender MI, Rozenberg E, Kar'kin AE, Chaudhuri BK, Gorodetsky G. The nature of the low-temperature minimum of resistivity in ceramic manganites. J Alloys Compd [Internet]. 2001 Aug;326(1–2):81–4. Available from: https://linkinghub.elsevier.com/retrieve/pii/S0925838801012282